ABSTRACT

OH, CHULWOO Finite-Difference Time-Domain Analysis of Periodic Anisotropic Media. (Under the direction of Dr. Michael J. Escuti).

The Finite-Difference Time-Domain (FDTD) method has been one of the most popular numerical techniques for solving electromagnetic propagation and scattering problems. Recent development in computer technologies allows us to have more power of computation and memory capacity, which overcomes the FDTD method's computationally intensive nature–a major hindrance to its widespread use.

For the applications of structures such as gratings and photonic crystals, the FDTD method can be made more efficient and accurate by taking advantage of periodicity. The simulation space can be substantially reduced into only one unit structure by enforcing periodic boundary conditions. The split-field update technique is an efficient way of implementing these boundary conditions with the capability of wide-band simulation at oblique incidence. However, previous work was limited to either isotropic or those possessing diagonal tensors.

This thesis presents a enhanced FDTD algorithm for periodic structures in more general anisotropic media incorporating spatially-varying non-diagonal permittivity tensors. Validation of the new FDTD method is done by applying it to problems of varying structure and comparing the results to other analytical or numerical solutions.

We perform an accurate numerical analysis of Polarization Gratings (PGs) for the first time using our FDTD tool. Diffraction properties such as the efficiency, polarization selectivity, and angular selectivity of each diffraction order are analyzed for several PG types. We also discuss behavior beyond the paraxial limit. Finally, we propose and numerically validate three different structures to create achromatic PGs with enhanced broadband diffraction properties. Preliminary experimental data on the achromatic PGs is also included.

A package of the FDTD code written in the standard C/C^{++} language will be publicly available as an open source software.

Finite-Difference Time-Domain Analysis of Periodic Anisotropic Media

by

Chulwoo Oh

A thesis submitted to the Graduate Faculty of
North Carolina State University
in partial fullfilment of the
requirements for the Degree of
Master of Science

Electrical and Computer Engineering

Raleigh

2006

Approved By:

Dr. Gianluca Lazzi	Dr. Keith Weninger

Dr. Michael J. Escuti
Chair of Advisory Committee

Biography

The author was born to Dae-Kyun Oh and Gui-Nam Lee in 1976 in Seoul, Korea and has two brothers, Won-Seok and Jun-Seok. He married Suna Woo in 2005. In 2003, he graduated from Yonsei University in Seoul, Korea. His undergraduate major was Electrical and Electronics Engineering. Since 2004, he has pursued graduate research in nanoelectronics and phtonics at North Carolina State University in Raleigh, NC within the department of Electrical and Computer Engineering.

Contents

List of Figures **v**

List of Tables **ix**

1 Introduction **1**

2 Fundamentals of Electromagnetic Optics **5**
2.1 Light as Electromagnetic Radiation 5
2.2 Polarization of Light 8
2.3 Light Propagation in Anisotropic Media 15
2.3.1 Linear Birefringence 15
2.3.2 Optical Activity 16
2.3.3 Light in Lossy Media and Dichroism 17
2.4 Light Propagation in Periodic Media 18
2.4.1 Periodic Structures and Gratings 19
2.4.2 Subwavelength Gratings 22
2.4.3 Near-Field to Far-Field Transformation 23

3 Finite-Different Time-Domain Method for Periodic Anisotropic Media **25**
3.1 Yee Algorithm 25
3.2 FDTD Algorithm for Periodic Anisotropic Media 29
3.3 Absorbing Boundary Conditions: UPML Approach 34
3.4 Numerical Dispersion and Stability 34
3.4.1 Numerical Dispersion 34
3.4.2 Stability Limit (Courant Stability Factor) 36
3.5 Wide-band Source and Vectorial Far-field Transformation 37

4 Validation of the FDTD Method **40**
4.1 Thin Phase Gratings 40
4.2 Dielectric Stacks as a Photonic Band Filter 45
4.3 Twisted Nematic Liquid Crystal Cells 47
4.4 Optically Active Media 49

5 Numerical Analysis of Polarization Gratings **50**
5.1 FDTD Analysis of Optical Properties of PGs 52
5.1.1 Linear Polarization Gratings 53
5.1.2 Elliptical Polarization Gratings 62
5.2 Design of Broadband Polarization Gratings 66
5.2.1 Polarizing Holography as a means of PG Creation 66
5.2.2 Combination of Double-Layered PGs with Mirror Images 69
5.2.3 Achromatic Polarization Gratings 72
5.2.4 Twisted Polarization Gratings 75

6 Conclusion **80**

Appendix **83**

A Finite-Difference Expressions for P-Q Field Equations **83**

Bibliography **87**

List of Figures

2.1 Polarization ellipse; a and b are the longest and shortest diameter, respectively. The angle of the polarization ellipse ψ is the angle of the major axes from the $+x$-axis and the angle of the ellipticity $\chi = \tan^{-1}(\pm b/a)$. 9
2.2 Various polarization configurations; The light would be linear with $\chi = 0$ and circular with $\chi = \pm\pi/4$. The orientation of a particular ellipse is defined as ψ. The electric field vector rotates clockwise for $(0 < \chi \leq \pi/2)$ and counterclockwise for $(-\pi/2 \leq \chi < 0)$. 10
2.3 Various polarization configurations; The light would be linear with $\chi = 0$ and circular with $\chi = \pm\pi/4$. The orientation of the ellipse is defined as ψ. The electric field vector rotates clockwise for $(0 < \chi \leq \pi/2)$ and counterclockwise for $(-\pi/2 \leq \chi < 0)$. 13
2.4 Rotation of the plane of polarization by an optically active medium 17
2.5 Two simple phase gratings: (a) a sinusoidal grating; (b) a binary grating. The grating parameters are the grating pitch Λ, the average index $\bar{n}$, and the index modulation factor n_1. 19
2.6 Two types of gratings: (a) a Bragg grating, which allows only one diffraction order; (b) a Raman-Nath grating, which can make several diffraction orders. 21
2.7 A subwavelength periodic structure. f_1 and f_2 are the fractions of the pitch (Λ) for the parts of ϵ_1 and ϵ_2 respectively. Note that $\Lambda \lesssim \lambda$. 23
2.8 Two-dimensional scattering or radiation geometry showing the integration contours used in the derivation of the near-to-far-field transformation [18]. . 24

3.1 Position of the electric and magnetic field vector components in the Yee space lattice [17]. 26
3.2 Space-time chart of the Yee algorithm for a propagating one-dimensional wave 28
3.3 Schematic view of the bi-dimensional Yee grid space. Arrows depict the direction of field vectors. 29
3.4 Variation of the numerical phase velocity depending on the propagation direction for three sampling densities $(N = 10, 20, 30)$ in a uniform square-cell grid 35
3.5 Stability limit for the split-field technique in two dimensions 37

4.1 Schematic of FDTD simulation space. Λ is the grating pitch and d is the grating thickness. 41
4.2 Diffraction efficiencies of a binary rectangular grating at normal incidence as a function of $n_1 d/\lambda$. The grating parameters are $\Lambda = 10\lambda$, $\bar{n} = 1.5$, $n_1 = 0.5$, and $f_t = 0.5$. 43
4.3 Diffraction efficiencies of a binary thin grating at 30° of incidence as a function of $n_1 d/\lambda$. The grating parameters are $\Lambda = 10\lambda$, $\bar{n} = 1.5$, $n_1 = 0.5$, and $f_t = 0.5$. 43
4.4 Near-field images of the electric field at (a) $\theta_{inc} = 0$ and (b) $\theta_{inc} = 30°$ for a binary rectangular grating, whose parameters are $\Lambda = 10\lambda$, $\bar{n} = 1.5$, $n_1 = 0.5$, $d = 0.5\lambda$ and $f_t = 0.5$. 44
4.5 Schematic view of a simple stack of dielectric layers with two different refractive indices ($n_1 = 1$, $n_2 = 5$) as a one dimensional photonic bandgap structure. The length of each period $\Lambda = 1um$ and the fill factor $f_t = 0.5$. 45
4.6 Transmittance of a simple stack of dielectric layers with two different refractive indices ($n_1 = 1$, $n_2 = 5$) at normal incidence. The length of period $\Lambda = 1\mu m$ and the fill factor $f_t = 0.5$. 46
4.7 Transmittance of a simple dielectric stack with two different refractive indices ($n_1 = 1$, $n_2 = 5$) at 30° incidence. The length of period $\Lambda = 1\mu m$ and the fill factor $f_t = 0.5$. 46
4.8 Schematic view of a 90°-twisted nematic liquid crystal cell between cross-polarizers; arrows depict nematic directors of liquid crystals. d is the thickness of the LC cell. 47
4.9 Transmittance through the 90°-twisted-nematic cell with ideal cross-polarizers as a function of the normalized retardation $\Delta n_l d/\lambda$. The parameters for LC materials are$\Delta n_0 = 1.6$ and $\Delta n_l = 0.2$. 48
4.10 The normalized Stokes parameters for transmitted light polarization of the 90°-twisted-nematic cell. The Stokes parameters are measured before the analyzing polarizer. The parameters for LC materials are$\Delta n_0 = 1.6$ and $\Delta n_l = 0.2$. 48
4.11 The normalized Stokes parameters for transmitted light polarization from a slab of optically active media with circular birefringence $\Delta n_c = 0.05$. 49

5.1 Two types of PGs: (a) linear PG; (b) elliptical PG. Λ is the optical pitch of anisotropy, which is a half of the periodicity (P/2), and the red arrows depict local anisotropy. 51
5.2 Diffraction efficiencies of the linear PG as a function of (a) the normalized retardation $\Delta n_l d/\lambda$ and (b) the ellipticity angle χ of the input polarization. The grating parameters are $\Lambda = 20\lambda_0$, $n_0 = 1.6$, and $\Delta n_l = 0.2$, where λ_0 is the center wavelength. 54
5.3 Near-field images of the electric field for (a) circularly polarized input and (b) linearly polarized input. The grating parameters are $\Lambda = 20\lambda$, $n_0 = 1.6$, $\Delta n_l = 0.2$, and $\Delta n_l d/\lambda = \frac{1}{2}$. 55
5.4 (a) Diffraction efficiencies and (b) the normalized Stokes parameter S_3' of the linear PG at various angle of incidence. 57

5.5 The effect of grating parameters ρ and Q on the diffraction properties of the linear PG. Diffraction efficiency (a sum of $\eta_{\pm 1}$) is calculated for different values of ρ (0.05, 1, 2, 5) as a function of the normalized retardation $\Delta n_l d/\lambda$; only d is a variable for a given ρ. 58
5.6 Linear PG within a single small pixel: (a) near-field map of the electric field and (b) far-field diffraction efficiency (a sum of $\eta_{\pm 1}$) for various pixel size L/Λ. The red line points 99.5% of efficiency. Each pixel is isolated by absorbing media (PML) and L is the size of a pixel. The grating parameters are $\Lambda = 10\lambda_0$, $n_0 = 1.6$, and $\Delta n_l = 0.2$, where λ_0 is the center wavelength. . 60
5.7 The effect of lateral pixelation in the anisotropy pattern of linear PGs. Diffraction efficiency (a sum of $\eta_{\pm 1}$) is calculated for the $\lambda/2$ retardation condition as a function of the number of sub-pixels P in one grating period. 61
5.8 Diffraction efficiencies of the elliptical PG as a function of the normalized retardation $\Delta n_l d/\lambda$. The grating parameters are $\Lambda = 20\lambda_0$, $n_0 = 1.6$, and $\Delta n_l = 0.2$, where λ_0 is the center wavelength. 62
5.9 Diffraction efficiencies of elliptical PGs as a function of (a) the normalized retardation $\Delta nd/\lambda$ and (b) the azimuth angle ψ of the input polarization. The grating parameters are $\Lambda = 20\lambda_0$, $n_0 = 1.6$, and $\Delta n_l = \Delta n_c = 0.2$, where λ_0 is the center wavelength. 64
5.10 Schematic view of the function of PGs on Poincré sphere; red color corresponds to linear PGs and blue color to elliptical PGs with both linear and circular birefringence. Arrows depict the conversion of polarization to the characteristic states: left- and right-hand circular polarizations for linear PGs; horizontal and vertical linear polarizations for elliptical PGs. 65
5.11 Optical system for recording polarizing holograms using two orthogonal polarizations, left- (LCP) and right-hand (RCP) circular or vertical (LVP) and horizontal (LHP) linear polarization. φ is the phase difference between recording beams and arrows depict induced anisotropy by polarization interference of two recording beams. 67
5.12 Fabrication procedures of holographic polarization gratings based on a combination of liquid crystal materials and the photo-alignment technique. . . . 68
5.13 Schematic view of the double-layered PG structure for broadband operation. Bars depict uniaxial birefringence in plane. 69
5.14 Diffraction efficiencies of double-layered PGs as a function of the normalized retardation $\Delta n_l d/\lambda$. Diffraction efficiency of linear PGs is marked for comparison. The grating parameters are $\Lambda = 20\lambda_0$, $n_0 = 1.6$, and $\Delta n_l = 0.2$, where λ_0 is the center wavelength. 71
5.15 Transmittance measured by spectro-photometer of the 0^{th} order for a single PG (PG1) and the double-layered PG (PG1-PG2). 71

5.16 Schematic view of the achromatic PG structure using three polarization gratings. θ_{shift} is the phase difference of the middle PG (PG2) with respect to the other PGs. Chiral liquid crystal layers (C1 and C2) with the opposite sense of twist (right- and left-hand) can be used to integrate three grating layers instead using three independent gratings. The structure using chiral LC layers is described inside of the box. Bars depict uniaxial birefringence in the plane. 73
5.17 Diffraction efficiency (a sum of $\eta_{\pm 1}$) of the achromatic PG using three grating layers as a function of the normalized retardation $\Delta n_l d/\lambda$ for different angular shifts θ_{shift} of the middle layer. The maximum bandwidth $\Delta\lambda_{max} = 60.22(\% - \lambda_0)$ for the first order diffraction can be achieved when $\theta_{twist} = 57^\circ$. The grating parameters are $\Lambda = 20\lambda_0$, $n_0 = 1.6$, and $\Delta n_l = 0.2$, where λ_0 is the center wavelength. 74
5.18 Schematic view of the double-layered twisted PG structure for broadband operation. θ_{twist} is the total twist angle of each layer of twisted PGs, which have opposite sense of twist. Bars depict uniaxial birefringence in the plane. 75
5.19 Diffraction efficiency (a sum of $\eta_{\pm 1}$) of the double-twisted PG as a function of the normalized retardation $\Delta n_l d/\lambda$ for different twist angles θ_{twist} from 0 to 90°. The maximum bandwidth $\Delta\lambda_{max} = 46.65(\% - \lambda_0)$ for the first order diffraction can be achieved when $\theta_{twist} = 70^\circ$. The grating parameters are $\Lambda = 20\lambda_0$, $n_0 = 1.6$, and $\Delta n_l = 0.2$, where λ_0 is the center wavelength. . . 76
5.20 Diffraction properties of the twisted PG: (a) diffraction efficiency (a sum of $\eta_{\pm 1}$) of the twisted PG as a function of the normalized retardation $\Delta n_l d/\lambda$ and (b) the first maximum diffraction efficiency for different twist angles θ_{twist} from 0 to 90°. The grating parameters are $\Lambda = 20\lambda_0$, $n_0 = 1.6$, and $\Delta n_l = 0.2$, where λ_0 is the center wavelength. 78
5.21 Diffraction characteristics of the twist PG: (a) spectrums of the 0^{th} order transmission and (b) estimated twist angles of the twisted PG with a number of layers N. 79

List of Tables

2.1 Stokes and Jones Vectors for Some Polarization States 14

4.1 FDTD Simulation Parameters 41

5.1 Parameters for linear and elliptical PG. 52

Chapter 1

Introduction

We see objects or images via light, but ironically we cannot see light itself. People have developed a number of theories to "*see*" the nature of light. Initially, light has been assumed to be a scalar wave because of its wave properties such as refraction or interference. However, it was later found that light has a vectorial nature since it exhibits properties such as polarization. James C. Maxwell successfully described light as an electromagnetic radiation for the first time in his paper on electrodynamics theory [1].

Light experiences a wave phenomenon known as diffraction, while propagating in periodic media. Gratings are periodic structures causing optical diffraction. When a grating forms in anisotropic media, it can produce polarization-dependent diffraction, which may have completely different properties from that of conventional diffraction gratings such as thin phase gratings. One of the most interesting anisotropic gratings is the polarization grating (PG), first realized by polarizing holograms [2].

There are many different types of PGs defined according by their anisotropy patterns. In this thesis we focus on two profiles we label the "linear" PG and the elliptical "PG." The unique diffraction characteristics of PGs owe to an in-plane anisotropy that varies with position [3, 4]. The number of diffraction orders and polarization properties can be determined by the anisotropy of PGs and the input polarization. Moreover, it is possible that only one order of diffraction has 100% efficiency even with *thin* gratings. These unique properties of PGs lead to numerous applications in a variety of fields; polarimetry, highly efficient polarizers, polarization beam splitters, light modulators, optical filters, spec-

trometry, light multiplexer and de-multiplexer, polarization sensing and recovering, image sensing, optical data storage, quantum computing, and remote sensing [5–10].

One can apply either analytical and numerical methods to design the grating parameters for advanced functions as well as to understand the physics of grating diffractions. There are two successful analytical methods for solving traditional phase or amplitude grating problems: the coupled-wave theory [11] and the modal approach method [12]. Both methods can result in very simple analytical solutions, applicable to most grating problems such as sinusoidal and binary gratings.

However, these analytical descriptions have several applicability limitations. First, the paraxial limit of gratings is often unclear. Solutions for gratings beyond the paraxial limit differ from those for gratings within the limit. Second, analytical methods are dependent on grating structures. Complex geometry of gratings leads in considerably complicated mathematical derivations. Finally, ideal infinite gratings are assumed. Because of these limitations, we desire to find robust numerical methods with both reasonable computation cost and acceptable numerical errors as effective alternatives.

The diffraction properties of PGs can be analyzed using the Jones matrix method [13]. The Jones matrix is one of the descriptive forms of polarizing systems. Unlike conventional phase or amplitude gratings, light propagation in PGs must be described by vector fields. Extensive studies on PG diffraction using the Jones matrix analysis can be found in [3, 4, 14–16]. However, the Jones matrix analysis is also limited by the same problems as other analytical methods.

The focus of this thesis is to develop a robust and efficient numerical tool for analysis of periodic anisotropic media like the polarization grating. We will apply the Finite-Difference Time-Domain (FDTD) method. The FDTD method is a direct finite difference solution of Maxwell's curl equations in time-domain.

In 1966, Kane Yee proposed an efficient and stable algorithm for electromagnetic problems, often called *the Yee algorithm* [17]. Since Yee's first work, the FDTD method has been one of the most popular numerical techniques in computational electromagnetics [18]. Recent development of computer technologies resolves the main drawback of the FDTD method–intensive computation and large memory cost. Now, the same FDTD simulations that required grid computers in the past can be solved on personal computers in reasonable amount of time.

In the FDTD method, the material properties can be easily incorporated by gener-

ating a mesh structure, called Yee's grid scheme. Fundamentally, there is no limit of material properties in the FDTD method though the original FDTD method was for isotropic media. Subsequently, the FDTD formulations for anisotropic media that have nondiagonal permittivity, permeability, and conductivity tensors, have been developed [19].

The dimensionality of problems with periodic structures can be dramatically reduced into a unit structure of periodicity by applying periodic boundary conditions (PBC). The implementation of PBCs in the FDTD method is straightforward in the case of normal incidence. Difficulty, however, arises when the incident angle is not normal to the structures. Since the phase difference between grid cells causes time advancing or retarding, a direct update in the time domain is generally impossible. One of the successful FDTD techniques for periodic structures at oblique incidence is the split-field update method, proposed by Roden et al. [20]. The basic idea of this method involves transforming and splitting the electric and magnetic fields in the phase domain to make their direction always normal to the problem structures to remove time gradients across the grid. The most important advantage is its capability of wideband analysis. However this work was limited to materials that have only diagonal tensors.

Our aim was the development of the FDTD algorithm for periodic anisotropic media with more general material properties at a general angle of incidence. To this end, we modified the split-field FDTD algorithm to incorporate the nondialgonal permittivity tensor. This FDTD method will be a very useful tool for analysis of a number of different optical elements, including isotropic or anisotropic gratings, polarizers, waveplates, diffractive optical elements (DOE), liquid crystal devices, and photonic crystals.

In Chapter 2, we start with Maxwell's equations and then introduce the fundamentals of electromagnetic theory and optics. Brief descriptions of the polarization of light and light propagation in anisotropic media follow. We also discuss light propagation in periodic structures including phase gratings.

Chapter 3 presents the modified FDTD algorithm for periodic anisotropic media. Details of the new FDTD formulations are described. The Yee algorithm and numerical characteristics of the FDTD method are briefly presented. In addition, wide-band source excitation and the vectorial near-field to far-field transformation are discussed.

In Chapter 4, the new FDTD method is applied to four different problems; thin phase gratings, dielectric stacks, twist nematic liquid crystal cells, and a slab of optically active media. The results from FDTD simulations are compared with other analytical and

numerical solutions for validation of the FDTD method.

Chapter 5 presents the FDTD analysis of polarization gratigns. Historical background and fabrication technologies of PG are introduced. Then, an extensive analysis of two different types of PGs – the linear PG and the elliptical PG – is presented. The FDTD results for diffraction efficiencies and polarization sensitivity of diffracted orders are compared with analytical solutions from the Jones matrix analysis and experimental data, where applicable. Finally, the effect of the grating regimes and the minimum pixel size for high diffraction efficiency are studied.

In Chapter 6, we propose and analyze three novel structures of the broadband PG using our FDTD simulation tool. The performance of each structure is evaluated in terms of the bandwidth for maximum diffraction efficiency. Preliminary experimental studies are also presented.

The seventh and final Chapter summarizes the results of this thesis and suggests topics for further study.

The work in this thesis has resulted in two conference publications and there are two manuscripts in preparation:

- C. Oh, R. Komanduri, and M. J. Escuti, "FDTD and Elastic Continuum Analysis of the Liquid Crystal Polarization Grating," *SID Symposium Digest* **37**, 844-847 (2006).

- C. Oh and M. J. Escuti, "Finite-Difference Time-Domain Analysis of Polarization Gratings," *SPIE Optics & Photonics Conference*, #6332-38, accepted (2006).

- C. Oh M. J. Escuti, "The Finite-Difference Time-Domain Method for Wideband Analysis of Periodic Anisotropic Media at Oblique Incidence," *Optics Express*, in preparation for submission (2006).

- C. Oh M. J. Escuti, "Rigorous Analysis of Polarization Gratings Using the Finite-Difference Time-Domain Method," *Physical Review A*, in preparation for submission (2006).

Chapter 2

Fundamentals of Electromagnetic Optics

"...light itself (including radiant heat and other radiations) is an electromagnetic disturbance in the form of waves propagated through the electromagnetic field according to electromagnetic laws" –James Clerk Maxwell

The electromagnetic origin of light was understood for the first time by James C. Maxwell [1]. Since his beautiful description of the electromagnetic field, the 'concealed' motion of light is captured by simple mathematical expressions now termed "Maxwell's equations." This chapter begins with Maxwell's equations and then introduces more general expressions and theories in electromagnetic optics.

2.1 Light as Electromagnetic Radiation

The electromagnetic field can be defined by two vector quantities: the electric and magnetic fields. Maxwell's equations describe the behavior of these two vector fields in relation to each other and the position and motion of charged particles. In differential

form, Maxwell's equations are given by

$$\nabla \times \boldsymbol{E}(\mathbf{r},t) = -\frac{\partial \boldsymbol{B}(\mathbf{r},t)}{\partial t} \qquad (Faraday's\ law) \tag{2.1a}$$

$$\nabla \times \boldsymbol{H}(\mathbf{r},t) = \boldsymbol{J}(\mathbf{r},t) + \frac{\partial \boldsymbol{D}(\mathbf{r},t)}{\partial t} \qquad (Ampere's\ law) \tag{2.1b}$$

$$\nabla \cdot \boldsymbol{D}(\mathbf{r},t) = \rho(\mathbf{r},t) \qquad (Gauss's\ law) \tag{2.1c}$$

$$\nabla \cdot \boldsymbol{B}(\mathbf{r},t) = 0 \qquad (Gauss's\ law) \tag{2.1d}$$

where $\mathbf{r}$ is the position vector and t is time. The field variables are defined as:

$$\boldsymbol{E} : electric\ field\ (V/m)$$
$$\boldsymbol{H} : magnetic\ field\ (A/m)$$
$$\boldsymbol{D} : electric\ displacement\ (W/m^2)$$
$$\boldsymbol{B} : magnetic\ flux\ density\ (C/m^2)$$
$$\boldsymbol{J} : electric\ current\ density\ (A/m^2)$$
$$\rho : electric\ charge\ density\ (C/m^3)$$

These variables (except ρ, a scalar) are vectors and may have complex amplitudes. ρ is a scalar variable function of space and time.

In order to solve Eq.2.1, another set of relationships between $\boldsymbol{D}$, $\boldsymbol{E}$, $\boldsymbol{B}$, and $\boldsymbol{H}$ must be known. These are called constitutive relations. These conditions are established by the physical properties of media; the permittivity ϵ and permeability μ. In a vacuum, these relations are:

$$\boldsymbol{D}(\mathbf{r},t) = \epsilon_0 \boldsymbol{E}(\mathbf{r},t) \tag{2.2a}$$

$$\boldsymbol{B}(\mathbf{r},t) = \mu_0 \boldsymbol{H}(\mathbf{r},t) \tag{2.2b}$$

where the subscript '$_0$' refers to the value in a vacuum. $\boldsymbol{J}$ can generally be found from Ohm's law: $\boldsymbol{J}(\mathbf{r},t) = \sigma(\mathbf{r})\boldsymbol{E}(\mathbf{r},t)$, where σ is the conductivity. Since materials of interest to us are nonmagnetic, μ is assumed as μ_o without any special comment. In linear media, $\epsilon = \epsilon(\mathbf{r})$ is a function of position. For anisotropic media, permittivity must be expressed in the form of a tensor $\tilde{\epsilon}$, which may have different values for each direction of the electromagnetic field vectors. We will discuss more about material properties and light propagation of anisotropic media in Section 2.3.

Maxwell's equations in a source-free space, where $\sigma = \rho = 0$, can be rewritten as:

$$\nabla \times \boldsymbol{E}(\mathbf{r}, t) = -\mu \frac{\partial \boldsymbol{H}(\mathbf{r}, t)}{\partial t} \tag{2.3a}$$

$$\nabla \times \boldsymbol{H}(\mathbf{r}, t) = \epsilon \frac{\partial \boldsymbol{E}(\mathbf{r}, t)}{\partial t} \tag{2.3b}$$

$$\nabla \cdot \boldsymbol{E}(\mathbf{r}, t) = 0 \tag{2.3c}$$

$$\nabla \cdot \boldsymbol{H}(\mathbf{r}, t) = 0 \tag{2.3d}$$

The electromagnetic wave equation can be derived from Eq.2.3a and 2.3b. We can eliminate $\boldsymbol{H}$ by taking the curl of Eq.2.3a and substituting Eq.2.3b:

$$\nabla \times (\nabla \times \boldsymbol{E}) = -\mu\epsilon \frac{\partial^2 \boldsymbol{E}}{\partial^2 t} \tag{2.4}$$

Applying the vector identity, it is reduced to

$$\nabla^2 \times \boldsymbol{E} = -\frac{1}{u^2} \frac{\partial^2 \boldsymbol{E}}{\partial^2 t} \tag{2.5}$$

where $u = (1/\mu\epsilon)^{1/2}$ is the phase velocity of light propagating in the medium; u in vacuum is given the spacial symbol $c = (1/\mu_o\epsilon_o)^{1/2} = 2.998 \times 10^8 (m/s)$, generally called the speed of light. In a dielectric medium, the phase velocity is $u = c/n$ where $n = (\epsilon/\epsilon_o)^{1/2}$ is referred to as the index of refraction. Without specifying the precise spatial nature of the wave, the time-harmonic electric field can be rewritten as $\boldsymbol{E}(\mathbf{r}) = \mathbf{E} \exp(j\omega t - j\mathbf{k} \cdot \mathbf{r})$ where $\mathbf{k}$ is the propagation vector and ω is the angular frequency. In a source-free space, $\mathbf{k} \cdot \mathbf{r} = \omega/u$. This is known as the dispersion relation. Substituting it into (2.3), we have

$$\nabla^2 \boldsymbol{E}(\mathbf{r}) + k^2 \boldsymbol{E}(\mathbf{r}) = 0 \tag{2.6}$$

where the wavenumber $k^2 = \mathbf{k} \cdot \mathbf{k} = (\omega/u)^2$. This is known as the Helmholtz equation. Similar expressions for $\boldsymbol{H}$ can be obtained.

2.2 Polarization of Light

In Cartesian coordinates, Maxwell's equations in the absence of sources ρ and $\boldsymbol{J}$ are given by

$$\epsilon \begin{bmatrix} \frac{\partial E_x}{\partial t} \\ \frac{\partial E_y}{\partial t} \\ \frac{\partial E_x}{\partial t} \end{bmatrix} = \begin{bmatrix} \frac{\partial H_z}{\partial y} - \frac{\partial H_y}{\partial z} \\ \frac{\partial H_x}{\partial z} - \frac{\partial H_z}{\partial x} \\ \frac{\partial H_y}{\partial x} - \frac{\partial H_x}{\partial y} \end{bmatrix} \tag{2.7a}$$

$$\mu \begin{bmatrix} \frac{\partial H_x}{\partial t} \\ \frac{\partial H_y}{\partial t} \\ \frac{\partial H_x}{\partial t} \end{bmatrix} = \begin{bmatrix} \frac{\partial E_y}{\partial z} - \frac{\partial E_z}{\partial y} \\ \frac{\partial E_z}{\partial x} - \frac{\partial E_x}{\partial z} \\ \frac{\partial E_x}{\partial y} - \frac{\partial E_y}{\partial x} \end{bmatrix} \tag{2.7b}$$

where E_i and H_i $(i = x, y, z)$ are field components corresponding to the principle axes of geometry.

Consider a uniform structure with no change in the shape or material properties along $\hat{\mathbf{z}}$. Any arbitrary polarized plane wave may be resolved into two cases, namely TM_z and TE_z modes; 'TE' and 'TM' refer to transverse electric and magnetic respectively. In the former, the $\boldsymbol{E}$ field lines parallel only to the $\hat{\mathbf{z}}$ direction. In the latter, the $\boldsymbol{E}$ field lies in a plane perpendicular to the $\hat{\mathbf{z}}$ direction. Eq.2.7 is reduced to:
For TM_z mode:

$$\begin{bmatrix} \epsilon \frac{\partial E_z}{\partial t} \\ \mu \frac{\partial H_x}{\partial t} \\ \mu \frac{\partial H_y}{\partial t} \end{bmatrix} = \begin{bmatrix} \frac{\partial H_z}{\partial y} - \frac{\partial H_y}{\partial z} \\ -\frac{\partial E_z}{\partial y} \\ \frac{\partial E_z}{\partial x} \end{bmatrix} \tag{2.8}$$

For TE_z mode:

$$\begin{bmatrix} \mu \frac{\partial H_z}{\partial t} \\ \epsilon \frac{\partial E_x}{\partial t} \\ \epsilon \frac{\partial E_y}{\partial t} \end{bmatrix} = \begin{bmatrix} \frac{\partial E_x}{\partial y} - \frac{\partial E_y}{\partial x} \\ -\frac{\partial H_z}{\partial y} \\ \frac{\partial H_z}{\partial x} \end{bmatrix} \tag{2.9}$$

Note that these two modes are orthogonal to each other.

A uniform plane wave is a particular solution of Maxwell's equations with $\boldsymbol{E}$ or $\boldsymbol{H}$ assuming the same direction, same magnitude, and same phase in infinite planes perpendicular to the direction of propagation. Although the orientation of the electric field is constant, its magnitude and sign can vary in time. The electric field resides in what is known as the plane of vibration. Polarization is the property of an electromagnetic wave or light, which shows the pattern of the electric field vibration. In other words, the polariza-

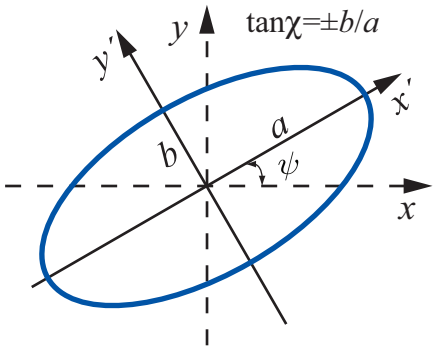


Figure 2.1: Polarization ellipse; a and b are the longest and shortest diameter, respectively. The angle of the polarization ellipse ψ is the angle of the major axes from the $+x$-axis and the angle of the ellipticity $\chi = \tan^{-1}(\pm b/a)$.

tion of a uniform plane wave describes the locus of the $\boldsymbol{E}$'s tip at a given point in space as a function of time [21].

An electric field may have only two other components perpendicular to the propagation direction, $\hat{\mathbf{k}}$, in order to satisfy $\nabla \cdot \boldsymbol{E} = 0$. For instance, if $\hat{\mathbf{k}}$ is $\hat{\mathbf{z}}$, the general form of the electric field phasor is given by

$$\boldsymbol{E}(z) = (\hat{\mathbf{x}}E_x + \hat{\mathbf{y}}E_y)e^{-jkz} \tag{2.10}$$

where E_x and E_y are complex amplitudes of the electric field vector corresponding to $\hat{\mathbf{x}}$ and $\hat{\mathbf{y}}$, respectively. The relative difference between x and y components determines the polarization of an electromagnetic wave. So it is convenient to rewrite the electric field as

$$\boldsymbol{E}(z) = \mathrm{E_o}e^{-jkz}(\hat{\mathbf{x}} + \mathrm{A}e^{-j\varphi}\hat{\mathbf{y}}) \tag{2.11}$$

The amplitude A and phase φ allow us to identify three types of polarization states.

Again, consider a plane wave propagating along the $\hat{\mathbf{z}}$ direction. A projection of the locus of the electric field's tip onto the xy-plane may make an ellipsoid whose circumference is referred to as the polarization ellipse. The polarization property can be described by two characteristic angles, referred to as the orientation angle of the polarization ellipse, ψ, and the angle of ellipticity, χ. ψ is the angle of the major axis of the ellipse from the $+x$-axis and χ is determined by the ratio between the longest diameter (a) and the shortest diameter (b) of the polarization ellipse ($\tan\chi = \pm b/a$) as shown in Fig.2.1. Both ψ and χ can be

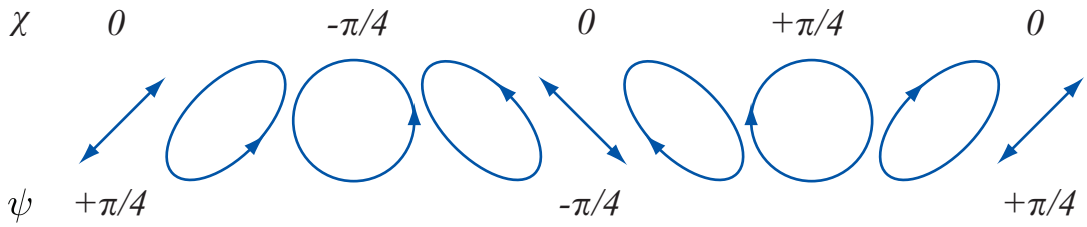


Figure 2.2: Various polarization configurations; The light would be linear with $\chi = 0$ and circular with $\chi = \pm\pi/4$. The orientation of a particular ellipse is defined as ψ. The electric field vector rotates clockwise for $(0 < \chi \leq \pi/2)$ and counterclockwise for $(-\pi/2 \leq \chi < 0)$.

written in terms of A and φ by introducing an auxiliary angle $\alpha(0 \leq \alpha \leq \pi/2)$:

$$\tan 2\psi = \frac{2\tan\alpha}{1-\tan^2\alpha}\cos\varphi \tag{2.12a}$$

$$\sin 2\chi = (\sin 2\alpha)\sin\varphi \tag{2.12b}$$

where $\tan\alpha = \mathrm{A}$. More details of the polarization ellipse may be found in [21].

In general, one can classify three types of polarization characteristics of electromagnetic waves: linear, circular, and elliptical polarization as shown in Fig.2.2.

Linear Polarization

If χ is 0, the locus of $\boldsymbol{E}$ looks linear at ψ from the $+x$-axis. In that case, a wave is linearly polarized. Particularly, one can say that light has horizontally linear polarization (HLP) when ψ=0 and vertical linear polarization (VLP) when $\psi = \pm\pi/2$.

Circular Polarization

If χ is $\pm\pi/4$, both $\alpha = \pm\pi/4$ and $\varphi = \pm\pi/2$ must be satisfied. In that case, ψ is 0. Since $\mathrm{A} = \tan\alpha = \pm 1$, the polarization ellipse becomes a circle; the wave is circularly polarized. If $\chi = +\pi/4$, the electric field vector rotates clockwise when looking down the z-axis; we call this case right circular polarization (RCP). If $\chi = -\pi/4$, the electric field vector rotates counterclockwise resulting in left circular polarization (LCP).

Elliptical Polarization

Elliptical polarization is the most general type of polarization; linear and circular polarization are special cases of elliptical polarization. If χ and ψ don't satisfy the above conditions for either or the other polarizations, the locus of the electric field makes an ellipse; the wave is elliptically polarized.

Stokes Parameters

An important and more general mathematical representation including aspects incoherency for polarized light was developed by G. G. Stokes in 1852. He showed that the polarization state of light can be specified by four quantities referred to as the *Stokes parameters* [21]. Consider a plane wave traveling along to $\hat{\mathbf{z}}$ to be represented by the equations:

$$E_x(t) = E_{ox}(t)\cos(\omega t - kz) \tag{2.13a}$$

$$E_y(t) = E_{oy}(t)\cos(\omega t - kz + \varphi(t)) \tag{2.13b}$$

where $E_{ox}(t)$ and $E_{oy}(t)$ are the complex amplitudes, ω is the angular frequency, and $\varphi(t)$ is the phase factor. Note that these quantities are instantaneous. The Stokes parameters for fully-polarized (coherent) light are obtained from the formulas:

$$S_0 = E_x E_x^* + E_y E_y^* \tag{2.14a}$$

$$S_1 = E_x E_x^* - E_y E_y^* \tag{2.14b}$$

$$S_2 = E_x E_y^* + E_y E_x^* \tag{2.14c}$$

$$S_2 = j\left(E_x E_y^* - E_y E_x^*\right) \tag{2.14d}$$

For the plane wave given in Eq.2.13, we can recast the Stokes parameters as

$$S_0 = E_{ox}^2 + E_{yo}^2 \tag{2.15a}$$

$$S_1 = E_{ox}^2 - E_{yo}^2 \tag{2.15b}$$

$$S_2 = 2E_{ox}E_{oy}\cos\varphi \tag{2.15c}$$

$$S_3 = 2E_{ox}E_{oy}\sin\varphi \tag{2.15d}$$

S_0 is the total intensity of the light. S_1 and S_2 describe the amount of vertical or horizontal polarization and linear $\pm 45^\circ$ polarization respectively. The last parameter S_3 depicts the

amount of left or right circular polarization. Also, notice that the Stokes parameters satisfy the relation:

$$S_0^2 = S_1^2 + S_2^2 + S_3^2 \tag{2.16}$$

For partially polarized light, the formulas for the Stokes parameters become the time-averaged values of Eq.2.14, but the relation in Eq.2.16 is restated:

$$S_0^2 \geq S_1^2 + S_2^2 + S_3^2 \tag{2.17}$$

The equal sign holds only for completely polarized light. One can determine the degree of polarization by use of the Stokes parameters. By definition,

$$P = \frac{I_{pol}}{I_{tot}} = \frac{\left(S_1^2 + S_2^2 + S_3^2\right)^{1/2}}{S_0^2} \tag{2.18}$$

where I_{pol} is the sum of the intensity of the polarization components and I_{tot} is the total intensity. It is often convenient to normalize parameters by the value of S_0; $S_0^{'} = 1$ and $|S_l^{'} = S_l/S_0| \leq 1$ where $l = 1, 2, 3$.

The set of Stokes parameters can be arranged in a matrix form known as the *Stokes vector*:

$$\mathbf{S} = \begin{bmatrix} S_0^{'} \\ S_1^{'} \\ S_2^{'} \\ S_3^{'} \end{bmatrix} = \begin{bmatrix} 1 \\ \cos 2\chi \cos 2\psi \\ \cos 2\chi \sin 2\psi \\ \sin 2\chi \end{bmatrix} \tag{2.19}$$

Eq.2.19 also shows how the Stokes parameters relate to two characteristic angles; the orientation angle (ψ) and the ellipticity angle (χ).

In 1892, Henri Poincaré developed a graphical method of depicting the polarization state. He introduced a sphere, now termed the *Poincaré sphere*, where the polar angle and the azimuth angle represent the polarization state as shown in Fig.2.3. The Stokes parameters can be captured in the Poincaré sphere even though he did not appear to know that. In particular, the Poincaré sphere is useful to describe the change in polarized light when it interacts with polarizing elements.

The *Jones vector* is another way to describe polarized light. R. Clark Jones invented this vector representation:

$$\boldsymbol{E} = \begin{bmatrix} E_{ox} e^{j\varphi_x} \\ E_{oy} e^{j\varphi_y} \end{bmatrix} \tag{2.20}$$

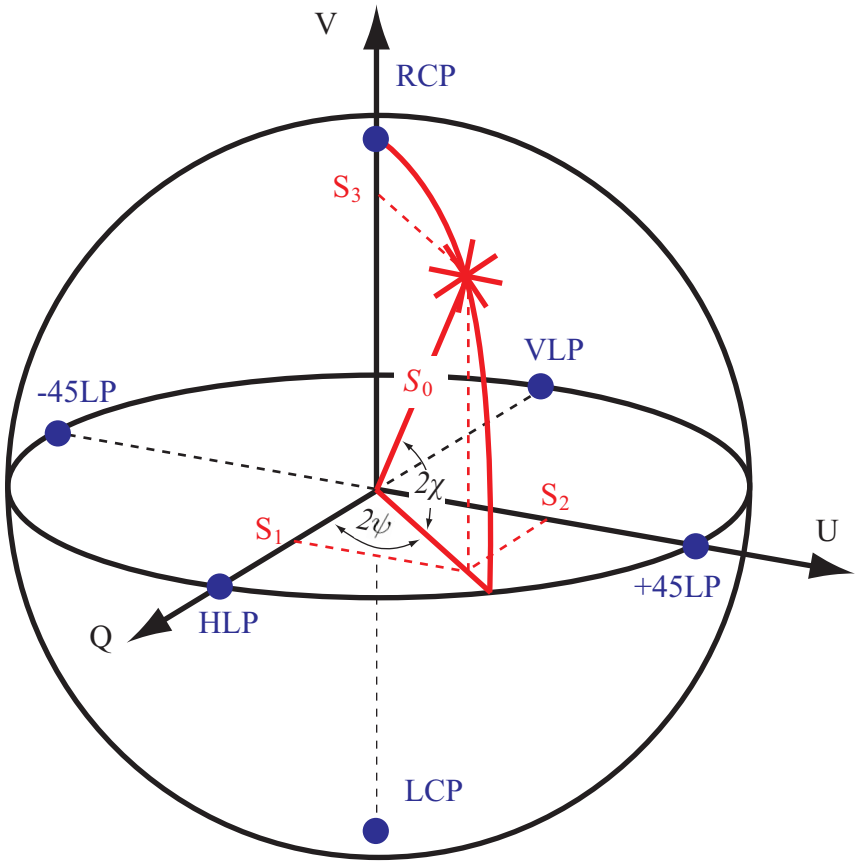


Figure 2.3: Various polarization configurations; The light would be linear with $\chi = 0$ and circular with $\chi = \pm\pi/4$. The orientation of the ellipse is defined as ψ. The electric field vector rotates clockwise for $(0 < \chi \leq \pi/2)$ and counterclockwise for $(-\pi/2 \leq \chi < 0)$.

where E_{ol} and φ_l are the instantaneous scalar amplitudes and the instantaneous phase factors for the l component of $\boldsymbol{E}$, respectively. The Jones vector can be normalized by the total irradiance ($I_{tot} = E_{xo}^2 + E_{yo}^2$) as follows:

$$\acute{\boldsymbol{E}} = \begin{bmatrix} e^{j\varphi_x} \cos\chi \\ e^{j\varphi_y} \sin\chi \end{bmatrix} \tag{2.21}$$

where $\tan\chi = E_{oy}/E_{ox}$.

Both the Stokes vector and the Jones vector can describe the polarization state of completely polarized light. However, only the Stokes vector can capture partial polarization and intensity. Still, the Jones vector is useful in many other cases because of its simplicity while the Stokes vector is a more complete form. Table 2.1 shows the Stokes vectors and the Jones vectors for particular polarization states.

Table 2.1: Stokes and Jones Vectors for Some Polarization States

State of Polarization	HLP	VLP	+45LP	-45LP	LCP	RCP
Stokes Vectors	$\begin{bmatrix} 1 \\ 1 \\ 0 \\ 0 \end{bmatrix}$	$\begin{bmatrix} 1 \\ -1 \\ 0 \\ 0 \end{bmatrix}$	$\begin{bmatrix} 1 \\ 0 \\ 1 \\ 0 \end{bmatrix}$	$\begin{bmatrix} 1 \\ 0 \\ -1 \\ 0 \end{bmatrix}$	$\begin{bmatrix} 1 \\ 0 \\ 0 \\ -1 \end{bmatrix}$	$\begin{bmatrix} 1 \\ 0 \\ 0 \\ 1 \end{bmatrix}$
Jones Vectors	$\begin{bmatrix} 1 \\ 0 \end{bmatrix}$	$\begin{bmatrix} 0 \\ 1 \end{bmatrix}$	$\frac{1}{\sqrt{2}}\begin{bmatrix} 1 \\ 1 \end{bmatrix}$	$\frac{1}{\sqrt{2}}\begin{bmatrix} 1 \\ -1 \end{bmatrix}$	$\frac{1}{\sqrt{2}}\begin{bmatrix} 1 \\ -i \end{bmatrix}$	$\frac{1}{\sqrt{2}}\begin{bmatrix} 1 \\ i \end{bmatrix}$

2.3 Light Propagation in Anisotropic Media

The vectorial nature of light can lead to different optical properties according to its polarization state when propagation occurs in media possessing anisotropy in refractive index or absorption. In this section, we briefly discuss optical anisotropy and light propagation in different anisotropic media.

2.3.1 Linear Birefringence

Recall the constitutive relation between $\boldsymbol{E}$ and $\boldsymbol{D}$. For anisotropic media with directional dependency, a tensor equation is necessary:

$$\boldsymbol{D}(\mathbf{r}, t) = \epsilon_0 \tilde{\epsilon} \boldsymbol{E}(\mathbf{r}, t) \tag{2.22}$$

where ϵ_0 is the dielectric constant in a vacuum and a tilde signifies a tensor. The permittivity tensor is a function of nine numbers. However, only three constants are necessary to specify $\tilde{\epsilon}$ with a proper choice of basis vectors since the permittivity tensor is symmetric ($\tilde{\epsilon} = \tilde{\epsilon}^T$):

$$\tilde{\epsilon} = \begin{bmatrix} \epsilon_x & 0 & 0 \\ 0 & \epsilon_y & 0 \\ 0 & 0 & \epsilon_z \end{bmatrix} \tag{2.23}$$

where $\epsilon_{x,y,z}$, are elements corresponding the *principal axes* of the coordinate system, called the *principal system*, where the permittivity tensor is diagonal. Note that materials in this thesis are non-magnetic so $\boldsymbol{B}(\mathbf{r}, t) = \mu_0 \boldsymbol{H}(\mathbf{r}, t)$.

In anisotropic media, $\boldsymbol{D}$ and $\boldsymbol{B}$ are perpendicular to the propagation vector $\hat{\mathbf{k}}$ while $\boldsymbol{E}$ and $\boldsymbol{H}$ may not be. Therefore, it is convenient to deal with electromagnetic wave problems in the new coordinate system called *kDB* system, which is formed by $\hat{\mathbf{k}}$ and the *DB* plane constructed by $\boldsymbol{D}$ and $\boldsymbol{B}$. In the *kDB* system, the constitutive relations between $\boldsymbol{E}$ and $\boldsymbol{D}$ fields and $\boldsymbol{H}$ and $\boldsymbol{B}$ fields are rewritten as a matrix representation:

$$\epsilon_0 \boldsymbol{E}(\mathbf{r}, t) = \tilde{\kappa} \boldsymbol{D}(\mathbf{r}, t) \tag{2.24a}$$

$$\mu_0 \boldsymbol{H}(\mathbf{r}, t) = \boldsymbol{B}(\mathbf{r}, t) \tag{2.24b}$$

where $\tilde{\kappa}$ is the *impermittivity* tensor in the media; $\kappa_l = 1/\epsilon_{x,y,z}$. The constitutive matrix $\tilde{\epsilon}$ or $\tilde{\kappa}$ determines the optical characteristics of the medium.

Consider the simplest anisotropic medium having one directional optical characteristics, namely *uniaxial*; $\epsilon_x = \epsilon_\perp$ and $\epsilon_y = \epsilon_z = \epsilon_\parallel$ where the subscripts '$_\parallel$' and '$_\perp$' refer to ordinary and extraordinary, respectively. $\hat{\mathbf{x}}$ is called the extraordinary or optic axis in contrast with $\hat{\mathbf{y}}$ and $\hat{\mathbf{z}}$, which are called the ordinary axes. The corresponding values for the refractive indices are $n_\parallel = (\epsilon_\parallel/\epsilon_0)^{1/2}$ and $n_\perp = (\epsilon_\perp/\epsilon_0)^{1/2}$. Clearly, the polarization property of light can vary when traveling in birefringent media. An ordinary wave propagates at phase velocity $u_\parallel = c/n_\parallel$, and an extraordinary wave travels at phase velocity $u_\perp = c/n_\perp$. When the propagation vector $\hat{\mathbf{z}}$ makes an angle θ with the optic axis, the phase velocity of light is given by $(\kappa_\parallel cos^2\theta + \kappa_\perp sin^2\theta)^{1/2}c$. This optical phenomenon, where two characteristic linearly polarized lights propagate at different velocities, is called '*linear birefringence*' [22]. The magnitude of linear birefringence is measured by $\Delta n_l = n_\perp - n_\parallel$.

An anisotropic medium with linear birefringence at an arbitrary optic axis can be captured in a permittivity tensor using the transformation matrix $\mathbf{T}$:

$$\tilde{\epsilon} = \mathbf{T}^{-1}(\phi,\theta) \begin{bmatrix} \epsilon_\perp & 0 & 0 \\ 0 & \epsilon_\parallel & 0 \\ 0 & 0 & \epsilon_\parallel \end{bmatrix} \mathbf{T}(\phi,\theta) \tag{2.25}$$

$\mathbf{T}$ is specified by two special angles (ϕ,θ):

$$\mathbf{T}(\phi,\theta) = \begin{bmatrix} \sin\phi & -\cos\phi & 0 \\ \cos\theta\cos\phi & \cos\theta\sin\phi & -\sin\theta \\ \sin\theta\cos\phi & \sin\theta\sin\phi & \cos\theta \end{bmatrix} \tag{2.26}$$

where ϕ and θ are the angles from the $\hat{\mathbf{x}}$ and $\hat{\mathbf{z}}$ axes, respectively. It can be seen that $\mathbf{T}^{-1} = \mathbf{T}^t$.

2.3.2 Optical Activity

Certain substances are found to possess the ability to rotate the plane of polarization of light passing through them as illustrated in Fig.2.4. This phenomenon is known as *optical activity* [23]. One can easily expect two cases upon the sense of rotation of the plane of polarization: namely, left-handed and right-handed. Like linear birefringence, optical activity can be explained by two characteristic waves: left and right circular waves. In an optically active medium, the phase velocity of each polarization differs from the other. *Circular birefringence* owes its name to this.

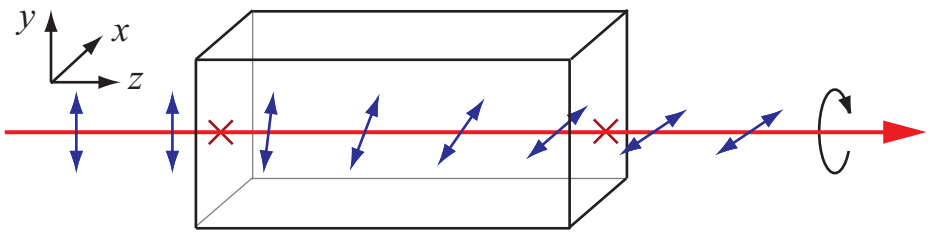


Figure 2.4: Rotation of the plane of polarization by an optically active medium

Consider a simple medium possessing the following permittivity matrix:

$$\tilde{\epsilon} = \begin{bmatrix} \epsilon_x & -j\epsilon_g & 0 \\ j\epsilon_g & \epsilon_x & 0 \\ 0 & 0 & \epsilon_z \end{bmatrix} \tag{2.27}$$

where ϵ_g is the gyration factor. The dispersion relation for a wave propagating along the $\hat{\mathbf{z}}$ direction is given by

$$k = \frac{\omega}{c}\sqrt{\epsilon_x \pm \epsilon_g} \tag{2.28}$$

where the upper sign corresponds to right circular polarization and the lower sign to left circular polarization. Accordingly, the refraction indices are

$$n_R = \sqrt{\epsilon_x + \epsilon_g} \tag{2.29a}$$

$$n_L = \sqrt{\epsilon_x - \epsilon_g} \tag{2.29b}$$

where the subscripts '$_R$' and '$_L$' represent right and left circular polarization, respectively. The difference of the refractive indices ($\Delta n_c = n_R - n_L$) is often called circular birefringence to distinguish it from linear birefringence Δn_l. It is convenient to discuss the amount of rotation per unit length of travel rather than the absolute value of circular birefringence. The *rotatory power* (δ_r) specifies the rotation of the polarization plane of light in the medium:

$$\delta_r = \Delta n_c \frac{\pi}{\lambda} \tag{2.30}$$

2.3.3 Light in Lossy Media and Dichroism

Until now, we limited our discussion to non-conductive materials. If the conductivity of a medium is non-zero, the amplitude of the electric field will decay in time. Resume

Ampere's law in the phasor representation:

$$\nabla \times \boldsymbol{H} = \boldsymbol{J} + j\omega\epsilon\boldsymbol{E} \qquad (Ampere's\ law) \tag{2.31}$$

Applying Ohm's law, Eq.2.31 can be rewritten:

$$\nabla \times \boldsymbol{H} = \sigma\boldsymbol{E} + j\omega\epsilon\boldsymbol{E} = j\omega\epsilon_{eff}\boldsymbol{E} \tag{2.32}$$

where the effective permittivity $\epsilon_{eff} = \epsilon(1 - j\sigma/\omega\epsilon)$. The dispersion relation in a lossy medium is

$$k^2 = (\omega/u)^2(1 - j\sigma/\omega\epsilon) \tag{2.33}$$

Now, the wavenumber k is a complex number. We express k as $k' - jk''$ where both k' and k'' are real numbers. The electric field propagating in the $+\hat{\mathbf{z}}$ direction is given by

$$\boldsymbol{E}(z) = E\, e^{-(jk'+k'')z} \tag{2.34}$$

For a highly conducting media, $k' \ll k''$ so the wave attenuates exponentially along the distance. On the other hand, the wave becomes purely sinusoidal in a insulator with $k' \gg k''$.

The conductivity may have directional dependency similar to dielectric anisotropy. The anisotropy in optical absorptive properties is called *dichroism*. The electromagnetic waves in different polarization states experience varying absorption in a dichroic medium. Eq.2.32 can be restated by introducing tensor expressions for the dielectric and absorpsive properties:

$$\nabla \times \boldsymbol{H} = \tilde{\sigma}\boldsymbol{E} + j\omega\epsilon_0\tilde{\epsilon}\boldsymbol{E} = j\omega\epsilon_0\tilde{\epsilon}_{eff}\boldsymbol{E} \tag{2.35}$$

where the effective permittivity tensor $\tilde{\epsilon}_{eff} = \tilde{\epsilon} - j\tilde{\sigma}/\epsilon_0\omega$.

2.4 Light Propagation in Periodic Media

An electromagnetic wave propagating through (reflecting from) gratings or holograms formed in photorefractive materials experiences refractive effects like diffraction or interference. Refractive effects can be achieved by spatial variation of two different types of material properties: refraction index or absorption coefficient. Gratings with index modulation are called phase gratings because the index locally affects the phase of a propagating wave. Gratings with variable absorption coefficients are called as amplitude gratings. In this paper, our interest is limited to transmission phase gratings even though absorptive gratings also have numerous applications.

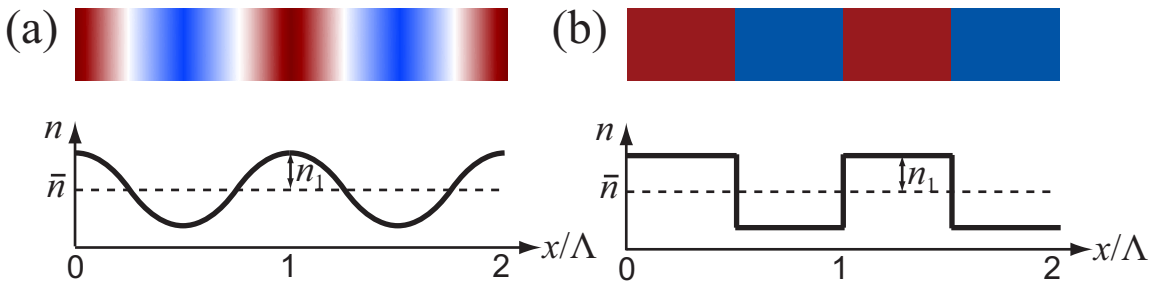


Figure 2.5: Two simple phase gratings: (a) a sinusoidal grating; (b) a binary grating. The grating parameters are the grating pitch Λ, the average index $\bar{n}$, and the index modulation factor n_1.

2.4.1 Periodic Structures and Gratings

The refractive index of periodic media is often written

$$n(x) = \bar{n} + n_1 \cdot p(x) \tag{2.36}$$

where $\bar{n}$ is the average index of refraction and n_1 is the index modulation factor. Also a grating vector $\hat{\mathbf{g}}$ which represents the direction of periodicity can be defined. If $\hat{\mathbf{g}}$ is $\hat{\mathbf{x}}$, $p(x)$ is a periodic function of x:

$$p(x) = p(x + \Lambda) \tag{2.37}$$

The index can be written by the sum of Fourier components of (2.36):

$$n(x) = \bar{n} + \frac{n_1}{2} \sum_l a_l \cos\left(j \frac{2\pi}{\Lambda} x\right) \tag{2.38}$$

where Λ is the grating pitch and a_l is the l^{th} component of the periodic index variation [24].

Two types of simple phase gratings, rectangular and sinusoidal, are illustrated in Fig. 2.5. These gratings are defined by the grating pitch Λ, average index $\bar{n}$ and index modulation factor n_1:

$$n(x) = \begin{cases} \bar{n} + n_1 \cos(Gx) & \text{for a sinusoidal grating} \\ \bar{n} + n_1 \left[1 - 2 \prod \left(\tan\left(\frac{1}{2} Gx\right)\right)\right] & \text{for a binary grating} \end{cases} \tag{2.39}$$

where G is the grating wave number $(2\pi/\Lambda)$ and $\prod(x)$ is a function that is 0 outside the interval $x = [-1, 1]$ and unity inside it. Note that the fill factor (f_t) for the rectangular gratings is assumed to be $\frac{1}{2}$.

The diffraction by a grating can be specified by integer numbers known as *Floquet* modes ($m = 0, \pm1, \pm2, \ldots$). The relation between the incident angle θ_{inc} and the transmitted angle θ_m to the m^{th} order is given by

$$\sin\theta_m = \frac{m\lambda}{\Lambda} + \sin\theta_{inc} \tag{2.40}$$

where λ is the wavelength of light. This relation is often referred to as the *grating equation*.

One can classify gratings in two regimes by the grating pitch and thickness relative to wavelength: the Bragg and Raman-Nath regimes. Diffraction characteristics differ for gratings in each regime as shown in Fig. 2.6. It is customary to distinguish among the two regimes of diffraction by defining a dimensionless parameter Q known as the *Klein parameter* [25]:

$$Q = \frac{2\pi\lambda d}{\bar{n}\Lambda^2} \tag{2.41}$$

where d is the grating thickness. For an oblique incidence, the Klein parameter can be written as $\acute{Q} = Q/\cos\theta_{inc}$. For $\acute{Q} \gg 1$, the grating characteristics depends on the Bragg diffraction. These gratings are known as Bragg gratings. In contrast, one defines the Raman-Nath gratings for $\acute{Q} \ll 1$ and $\Lambda > \lambda$.

The above descriptions of the grating regimes using Q or $\acute{Q}$ may be invalid for some extreme cases such as gratings with too large or too small index contrast. Moharam et al. introduced a new dimensionless parameter ρ [26]:

$$\rho = \frac{\lambda^2}{\bar{n}n_1\Lambda^2} \tag{2.42}$$

The Bragg regime resides in the condition of $\rho \gg 1$ and the Raman-Nath regime in the condition of $\rho \leq 1$. Note that the grating thickness does not enter ρ. The terms of thick or thin are irrelevant to the regime where the grating operates even though we usually refer to Bragg gratings as *thick* gratings and the Raman-Nath gratings as *thin* gratings.

Bragg Transmission Grating

When the grating pitch is not too large ($Q \gg 1$ or $\rho \gg 1$), a transmission grating may operate in the Bragg regime. The maximum diffraction occurs where the incident angle satisfies the following condition:

$$2\Lambda\sin\theta_i = \lambda \tag{2.43}$$

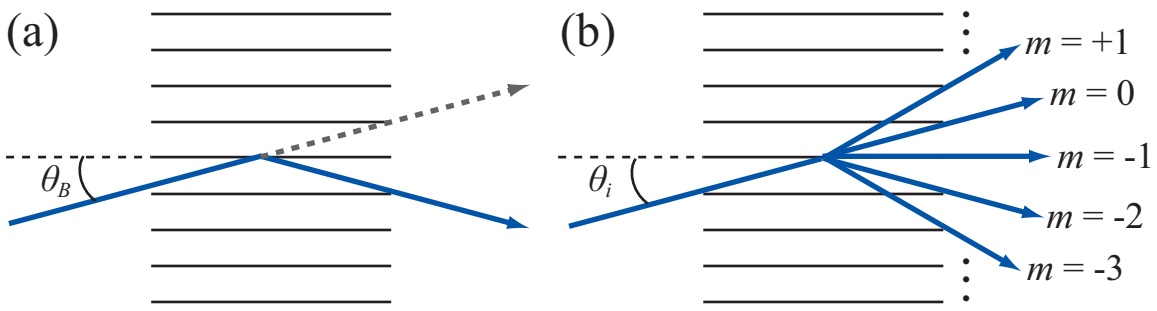


Figure 2.6: Two types of gratings: (a) a Bragg grating, which allows only one diffraction order; (b) a Raman-Nath grating, which can make several diffraction orders.

This angle is known as the Bragg angle θ_B. The diffraction angle of the transmitted wave is given by

$$\theta_t = \theta_B + \Delta\theta \tag{2.44}$$

where $\Delta\theta$ represents a phase mismatch between the incident and transmitted waves. Kogelink's coupled wave method is applicable to calculate the diffraction efficiency of Bragg transmission gratings [11]. The maximum diffraction efficiency of a Bragg grating can be written as:

$$\eta_{max} = \frac{1}{1 + \left(\frac{G\Delta\theta}{2\xi}\right)^2} \tag{2.45}$$

where G is the grating number $(2\pi/\Lambda)$ and ξ^2 is given by $\frac{(\pi n_1/\lambda)^2}{\cos\theta_i \cos\theta_t}$. Note that if $\Delta\theta$ is 0, the maximum diffraction efficiency can be 100%.

Raman-Nath Transmission Grating

Gratings for $Q \ll 1$ (or $\rho \leq 1$) can make a number of diffraction orders relevant to the incident angle. From the grating equation given in Eq.2.40, the transmission angle of the m^{th} order is $\sin(\theta_m) = \left(\frac{m\lambda}{\Lambda}\right) + \sin(\theta_{inc})$. It is clear that the number of possible modes is determined by wavelength λ and grating pitch Λ.

Two different effective methods can be applied to predict the diffraction efficiency of thin phase gratings based on the index profiles of sinusoidal and rectangular profiles. For a thin grating having a sinusoidal modulation in its refractive index, the coupled-wave theory can be applied and results in a simple analytical expression for the m^{th} order diffraction

efficiency as a form of Bessel's functions [24]:

$$\eta_m = J_m^2 \left(\frac{2\pi \bar{n} d}{\lambda \cos \theta_{inc}} \right) \tag{2.46}$$

where J_m is the m^{th} order Bessel's function.

For a binary thin grating, the transmittance method can be applied to calculate the diffraction efficiencies [27]. Consider a grating which has rectangular grooves. The diffraction efficiency of the m^{th} order is obtained by:

$$\eta_m = \begin{cases} \cos^2 \varphi & \text{for the } 0^{th} \text{ order} \\ \frac{4 \sin^2 \varphi}{(m\pi)^2} & \text{for the } m^{th} \text{ order} \end{cases} \tag{2.47}$$

where the phase angle φ is $\frac{\pi n_1 d}{\lambda \cos \theta_g}$; θ_g is the refractive angle of the grating, which satisfies $\bar{n} \sin \theta_g = n_0 \sin \theta_{inc}$.

The previous analytical solutions for the diffraction efficiencies fail where the paraxial approximation fails, i.e. highly oblique incidence, though they are simple and powerful in the most cases. Moharam and his coworkers developed a more complete algorithm for grating diffraction problems, namely the "Rigorous Coupled Wave (RCW)" analysis [28–30].

2.4.2 Subwavelength Gratings

Birefringence may arise from an ordered structure of optically isotropic material whose size is small compared with the wavelength of light. We then speak of *form birefringence* [22]. A wave propagating in subwavelength features experiences anisotropy in the effective refractive indicies, which leads to two characteristic waves: an ordinary wave and extraordinary wave.

Consider a periodic structure composed of subwavelength features having permittivity distribution shown in Fig.2.7:

$$\epsilon = \begin{cases} \epsilon_1 & \text{for } (p \leq x/\Lambda \leq p + f_1) \\ \epsilon_2 & \text{for } (p - f_2 \leq x/\Lambda \leq p) \end{cases} \tag{2.48}$$

where $\Lambda \lesssim \lambda$, p is an integer and $f_1 + f_2 = 1$ $(f_1, f_2 > 0)$. The effective dielectric constant

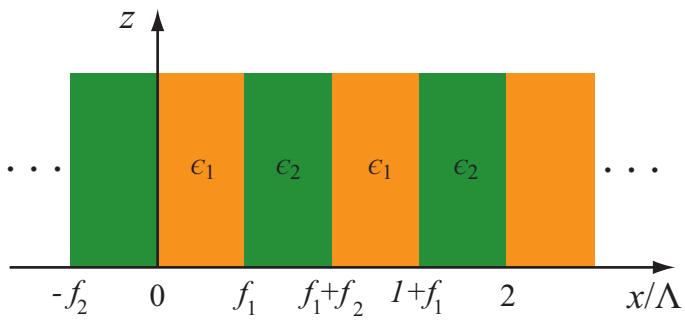


Figure 2.7: A subwavelength periodic structure. f_1 and f_2 are the fractions of the pitch (Λ) for the parts of ϵ_1 and ϵ_2 respectively. Note that $\Lambda \lesssim \lambda$.

$\epsilon_\perp$ for the ordinary wave and $\epsilon_\parallel$ for the extraordinary wave are given by

$$\epsilon_\perp = \frac{\epsilon_1 \epsilon_2}{f_1 \epsilon_2 + f_2 \epsilon_1} \tag{2.49a}$$

$$\epsilon_\parallel = f_1 \epsilon_1 + f_2 \epsilon_2 \tag{2.49b}$$

Now the form-refringence Δn can be defined as $(\epsilon_\parallel - \epsilon_\perp)^{1/2}$:

$$\Delta n^2 = -\frac{f_1 f_2 (\epsilon_1 - \epsilon_2)^2}{f_1 \epsilon_2 + f_2 \epsilon_1} \tag{2.50}$$

This assembly behaves like a negative uniaxial crystal. One can modulate the refractive index by varying the thickness of features or rotating the effective optic axis. Extensive studies of subwavelength gratings are found in [31–35]. Subwavelength gratings are essentially equivalent to anisotropic gratings in naturally birefringent media such as liquid crystals [36, 37].

2.4.3 Near-Field to Far-Field Transformation

Diffraction patterns are distinguished by the distance between diffractive elements and an observation point. As the plane of observation moves away from the point where diffraction occurs, the patterns of diffraction become more prominent and the image becomes more structured. This phenomenon is known as *Fresnel* or near-field diffraction. At a very great distance from that point, moving the plane of observation only changes the size of the pattern and not its shape. This is known as *Fraunhofer* or far-field diffraction.

Remember the Helmholtz equation: $\nabla^2 \boldsymbol{E} + k^2 \boldsymbol{E} = 0$. It can be solved with the aid of Green's theorem. The optical disturbance existing at a point P, expressed in terms of the

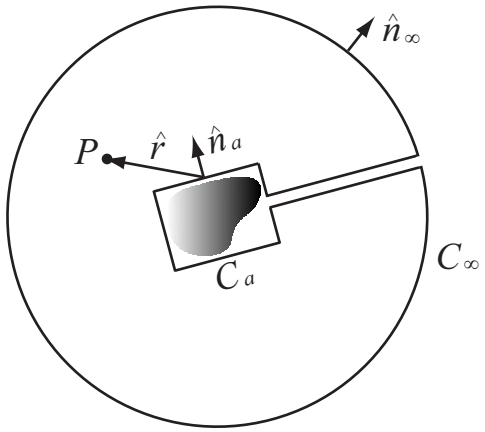


Figure 2.8: Two-dimensional scattering or radiation geometry showing the integration contours used in the derivation of the near-to-far-field transformation [18].

optical disturbance and its gradient evaluated on an arbitrary closed surface S, enclosing P, is

$$E_P = \frac{1}{4\pi}\left[\oint_s \frac{e^{jkr}}{r}\nabla E \cdot d\mathbf{S} - \oint_s E\nabla\left(\frac{e^{jkr}}{r}\right)\cdot d\mathbf{S}\right] \tag{2.51}$$

This is known as the Kirchhoff's integral theorem [38]. Far-field transformations in 2D make changes from the surface integral of (2.51) to a closed-loop integral as shown in Fig. 2.8.

For planar periodic structures, the near-field to far-field transformation becomes much simpler. Waves of each Floquet mode construct the diffraction pattern in the near-field region. Therefore, the far-field of the m^{th} order can be extracted from the near-field by the Fourier transformation:

$$E_{far,m}(\omega) = \frac{1}{\Lambda}\int_0^\Lambda E_{near}(\omega, x)\exp\left[j\left(\frac{2\pi m}{\Lambda} + k_0 \sin\theta_{inc}\right)x\right]dx \tag{2.52}$$

where ω is the frequency and k_0 is the wave-number of an incident wave.

Chapter 3

Finite-Different Time-Domain Method for Periodic Anisotropic Media

3.1 Yee Algorithm

The FDTD methods solve for both electric and magnetic fields in time and space using the coupled the Maxwell curl equations rather than solving for the electric field alone with a wave equation. The basic formulation is derived from the differential form of Maxwell's equations in time domain. The Yee algorithm is based on the approximation of the derivatives by central differences with the second-order accuracy and on the use of the Yee scheme to evaluate the field components. The discretized field values can be allocated on the Yee lattice as shown in Fig. 3.1. The Yee algorithm centers the $\boldsymbol{E}$ and $\boldsymbol{H}$ components in three-dimensional space so that every $\boldsymbol{E}$ component is surrounded by four circulating $\boldsymbol{H}$ components, and every $\boldsymbol{H}$ component surrounded by four circulating $\boldsymbol{E}$ components. This provides a beautifully simple picture of three-dimensional space being filled by an interlinked array of Faraday's Law and Ampere's Law contours. The Yee algorithm

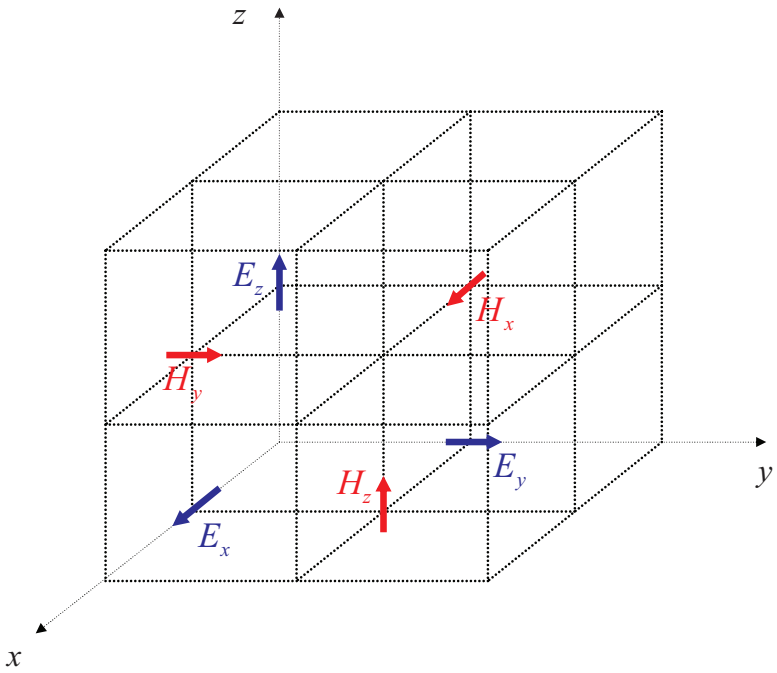


Figure 3.1: Position of the electric and magnetic field vector components in the Yee space lattice [17].

simultaneously simulates the pointwise differential form and the macroscopic integral from the Maxwell's equations. The latter is extremely useful in specifying boundary conditions and singularities.

The finite difference expressions for the time derivatives are central difference in nature and second-order accurate. The Yee algorithm also centers its $\boldsymbol{E}$ and $\boldsymbol{H}$ components in time in what is termed a leapfrog arrangement with the spatial increment Δu and the temporal increment Δt as shown in Fig. 3.2. All of the $\boldsymbol{E}$ computations in the modeled space are completed and stored in memory for a particular time-step using previously stored $\boldsymbol{H}$ data. Then all of the $\boldsymbol{H}$ computations in the space are completed and stored in memory using the $\boldsymbol{E}$ data just computed. This method is called the 'staggered field-update.' The cycle begins again with the re-computation of the $\boldsymbol{E}$ components based on the newly obtained $\boldsymbol{H}$. This process continues until time-stepping is concluded.

The FDTD is based solely on the time-domain Maxwell curl equations in differen-

tial form. Resume Eq. 2.1a and 2.1b in free space:

$$\nabla \times \boldsymbol{E} = -j\omega\mu_0 \boldsymbol{H} \tag{3.1a}$$

$$\nabla \times \boldsymbol{H} = j\omega\epsilon_0 \boldsymbol{E} \tag{3.1b}$$

In the Cartesian coordinate system, each of Eq. 3.1a and 3.1b become three separate equations of scalar components:

$$\epsilon_0 \frac{\partial E_x}{\partial t} = \frac{\partial H_z}{\partial y} - \frac{\partial H_y}{\partial z} \tag{3.2a}$$

$$\epsilon_0 \frac{\partial E_y}{\partial t} = \frac{\partial H_x}{\partial z} - \frac{\partial H_z}{\partial x} \tag{3.2b}$$

$$\epsilon_0 \frac{\partial E_z}{\partial t} = \frac{\partial H_y}{\partial x} - \frac{\partial H_x}{\partial y} \tag{3.2c}$$

$$\tag{3.2d}$$

$$-\mu_0 \frac{\partial H_x}{\partial t} = \frac{\partial H_z}{\partial y} - \frac{\partial H_y}{\partial z} \tag{3.3a}$$

$$-\mu_0 \frac{\partial H_y}{\partial t} = \frac{\partial H_x}{\partial z} - \frac{\partial H_z}{\partial x} \tag{3.3b}$$

$$-\mu_0 \frac{\partial H_z}{\partial t} = \frac{\partial H_y}{\partial x} - \frac{\partial H_x}{\partial y} \tag{3.3c}$$

$$\tag{3.3d}$$

The Yee algorithm expresses these time-dependent partial differential equations using center-differencing in orthogonal grid-space. When the three dimensional mesh is generated as a cubic lattice , where the distance between the nearest grid points is uniform ($\Delta u = \Delta x = \Delta y = \Delta z$), the FDTD formulations become

$$\begin{aligned} E^{n+1}_{x,(i+1/2,j,k)} - E^{n}_{x,(i+1/2,j,k)} = {} & \frac{\Delta t}{\epsilon_0 \Delta u}\left(H^{n+1/2}_{z,(i+1/2,j+1/2,k)} - H^{n+1/2}_{z,(i+1/2,j-1/2,k)}\right) \\ & - \frac{\Delta t}{\epsilon_0 \Delta u}\left(H^{n+1/2}_{y,(i+1/2,j,k+1/2)} - H^{n+1/2}_{y,(i+1/2,j,k-1/2)}\right) \end{aligned} \tag{3.4a}$$

$$\begin{aligned} E^{n+1}_{y,(i,j+1/2,k)} - E^{n}_{y,(i,j+1/2,k)} = {} & \frac{\Delta t}{\epsilon_0 \Delta u}\left(H^{n+1/2}_{x,(i,j+1/2,k+1/2)} - H^{n+1/2}_{x,(i,j+1/2,k-1/2)}\right) \\ & - \frac{\Delta t}{\epsilon_0 \Delta u}\left(H^{n+1/2}_{z,(i+1/2,j+1/2,k)} - H^{n+1/2}_{z,(i-1/2,j+1/2,k)}\right) \end{aligned} \tag{3.4b}$$

$$\begin{aligned} E^{n+1}_{z,(i,j,k+1/2)} - E^{n}_{z,(i,j,k+1/2)} = {} & \frac{\Delta t}{\epsilon_0 \Delta u}\left(H^{n+1/2}_{y,(i+1/2,j,k+1/2)} - H^{n+1/2}_{y,(i-1/2,j,k+1/2)}\right) \\ & - \frac{\Delta t}{\epsilon_0 \Delta u}\left(H^{n+1/2}_{x,(i,j+1/2,k+1/2)} - H^{n+1/2}_{x,(i,j-1/2,k+1/2)}\right) \end{aligned} \tag{3.4c}$$

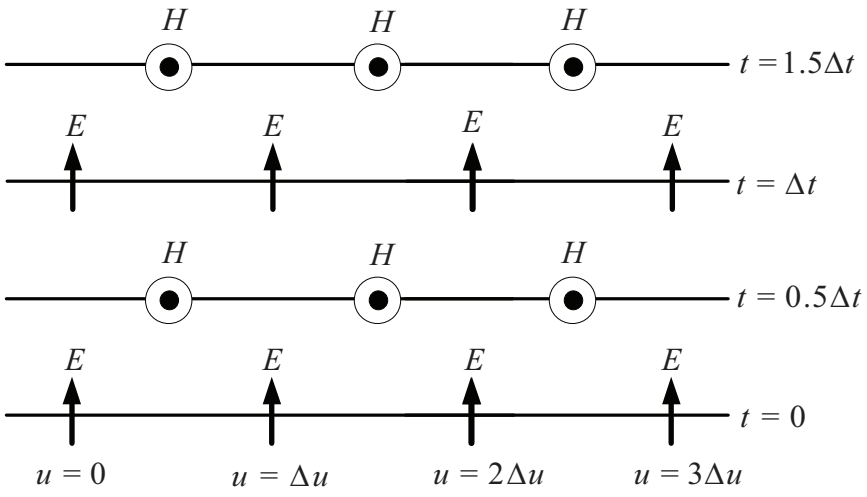


Figure 3.2: Space-time chart of the Yee algorithm for a propagating one-dimensional wave

$$H^{n+1/2}_{x,(i,j+1/2,k+1/2)} - H^{n-1/2}_{x,(i,j+1/2,k+1/2)} = \frac{\Delta t}{\mu_0 \Delta u}\left(E^n_{z,(i,j+1,k+1/2)} - E^n_{z,(i,j,k+1/2)}\right) - \frac{\Delta t}{\mu_0 \Delta u}\left(E^n_{y,(i,j+1/2,k+1)} - E^n_{y,(i,j+1/2,k)}\right) \tag{3.5a}$$

$$H^{n+1/2}_{y,(i+1/2,j,k+1/2)} - H^{n-1/2}_{y,(i+1/2,j,k+1/2)} = \frac{\Delta t}{\mu_0 \Delta u}\left(E^n_{x,(i+1/2,j,k+1)} - E^n_{x,(i+1/2,j,k)}\right) - \frac{\Delta t}{\mu_0 \Delta u}\left(E^n_{z,(i+1,j,k+1/2)} - E^n_{z,(i,j,k+1/2)}\right) \tag{3.5b}$$

$$H^{n+1/2}_{z,(i+1/2,j+1/2,k)} - H^{n-1/2}_{z,(i+1/2,j+1/2,k)} = \frac{\Delta t}{\mu_0 \Delta u}\left(E^n_{y,(i+1,j+1/2,k)} - E^n_{y,(i,j+1/2,k)}\right) - \frac{\Delta t}{\mu_0 \Delta u}\left(E^n_{x,(i+1/2,j+1,k)} - E^n_{x,(i+1/2,j,k)}\right) \tag{3.5c}$$

This lattice places electric fields on the edges of the unit cell and magnetic fields on the faces. A large number of these cells are then stacked together to form a computation domain. The domain needs to be terminated by appropriate boundary conditions.

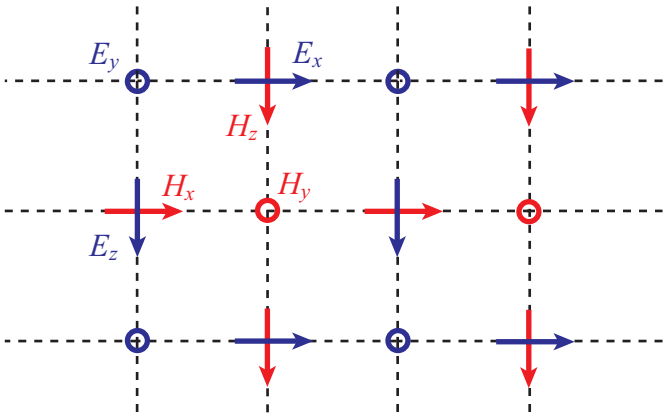


Figure 3.3: Schematic view of the bi-dimensional Yee grid space. Arrows depict the direction of field vectors.

3.2 FDTD Algorithm for Periodic Anisotropic Media

Maxwell's equations for a nonconductive anisotropic medium can be rewritten in phasor form as follows:

$$\nabla \times \boldsymbol{E} = -j\omega\mu_o \boldsymbol{H} \tag{3.6a}$$

$$\nabla \times \boldsymbol{H} = j\omega\epsilon_0 \tilde{\epsilon} \boldsymbol{E} \tag{3.6b}$$

where $\tilde{\epsilon}$ is given by

$$\tilde{\epsilon} = \begin{bmatrix} \epsilon_{xx} & \epsilon_{xy} & \epsilon_{xz} \\ \epsilon_{yx} & \epsilon_{yy} & \epsilon_{yz} \\ \epsilon_{zx} & \epsilon_{zy} & \epsilon_{zz} \end{bmatrix} \tag{3.7}$$

Let us consider the two-dimensional cases for simplicity. All six components of the electric and magnetic field are mapped on a bi-dimensional grid-space, which is the projection of the original Yee cell [17] onto the z-x plane as shown in Fig. 3.3 . **E** and **H** field can be updated in time by using the leapfrog approach. However the off-diagonal terms of the permittivity tensor in Eq. 3.6b result in three temporal derivatives of the electric field, which cannot be solved simultaneously. These time-domain correlations of the electric field components can be resolved by introducing the impermittivity tensor ($\tilde{\kappa} = \tilde{\epsilon}^{-1}$). Eq. 3.6b becomes

$$\tilde{\kappa} \nabla \times \boldsymbol{H} = j\omega\epsilon_o \boldsymbol{E} \tag{3.8}$$

Separating Eq. 3.6 into each field component yields

$$j\omega\epsilon_o E_x = -\kappa_{xx}\frac{\partial H_y}{\partial z} + \kappa_{xy}(\frac{\partial H_x}{\partial z} - \frac{\partial H_z}{\partial x}) + \kappa_{xz}\frac{\partial H_y}{\partial x} \tag{3.9a}$$

$$j\omega\epsilon_o E_y = -\kappa_{yx}\frac{\partial H_y}{\partial z} + \kappa_{yy}(\frac{\partial H_x}{\partial z} - \frac{\partial H_z}{\partial x}) + \kappa_{yz}\frac{\partial H_y}{\partial x} \tag{3.9b}$$

$$j\omega\epsilon_o E_z = -\kappa_{zx}\frac{\partial H_y}{\partial z} + \kappa_{zy}(\frac{\partial H_x}{\partial z} - \frac{\partial H_z}{\partial x}) + \kappa_{zz}\frac{\partial H_y}{\partial x} \tag{3.9c}$$

and

$$j\omega\mu_o H_x = \frac{\partial E_y}{\partial z} \tag{3.10a}$$

$$j\omega\mu_o H_y = \frac{\partial E_z}{\partial x} - \frac{\partial E_x}{\partial z} \tag{3.10b}$$

$$j\omega\mu_o H_z = -\frac{\partial E_y}{\partial x} \tag{3.10c}$$

where κ_{ab} corresponds to the (a, b) element of $\tilde{\kappa}$.

For a problem with periodic features, imposing periodic boundary conditions can improve computation time and memory limit dramatically. A solution for the normal incidence case is straightforward. However, the application of boundary conditions is difficult when the incident wave is oblique to the surface of the structure. Phase variation between different grid cells causes time-delay or -advance which makes the periodic boundary condition complex to solve in the time domain. In this thesis, we apply a field transformation technique, referred to as the split-field update method, to circumvent this difficulty for periodic anisotropic media.

An obliquely incident planewave at an angle θ_{inc} has phase difference along the $\hat{\mathbf{x}}$ direction. The periodicity of each cell is accounted for using Floquet theory. To remove the phase difference across grids, a Floquet transformation may be applied. In the Floquet mapping space, a new set of field variables is now introduced:

$$\mathbf{P} = \mathbf{E}\exp(jk_x x) \tag{3.11a}$$

$$\mathbf{Q} = c\mu_0\mathbf{H}\exp(jk_x x) \tag{3.11b}$$

where c is the speed of light in a vacuum and $k_x = (\omega/c)\sin\theta_{inc}$. Substituting $P_{x,y,z}$ and

$Q_{x,y,z}$ into Eq. 3.9 and 3.10 gives us a new form of the Maxwell curl equations:

$$\frac{j\omega}{c}P_x = -\kappa_{xx}\frac{\partial Q_y}{\partial z} + \kappa_{xy}(\frac{\partial Q_x}{\partial z} - \frac{\partial Q_z}{\partial x}) + \kappa_{xz}\frac{\partial Q_y}{\partial x} + jk_x(\kappa_{xy}Q_z - \kappa_{xz}Q_y) \tag{3.12a}$$

$$\frac{j\omega}{c}P_y = -\kappa_{yx}\frac{\partial Q_y}{\partial z} + \kappa_{yy}(\frac{\partial Q_x}{\partial z} - \frac{\partial Q_z}{\partial x}) + \kappa_{yz}\frac{\partial Q_y}{\partial x} + jk_x(\kappa_{yy}Q_z - \kappa_{yz}Q_y) \tag{3.12b}$$

$$\frac{j\omega}{c}P_z = -\kappa_{zx}\frac{\partial Q_y}{\partial z} + \kappa_{zy}(\frac{\partial Q_x}{\partial z} - \frac{\partial Q_z}{\partial x}) + \kappa_{zz}\frac{\partial Q_y}{\partial x} + jk_x(\kappa_{zy}Q_z - \kappa_{zz}Q_y) \tag{3.12c}$$

and

$$\frac{j\omega}{c}Q_x = \frac{\partial P_y}{\partial z} \tag{3.13a}$$

$$\frac{j\omega}{c}Q_y = \frac{\partial P_z}{\partial x} - \frac{\partial P_x}{\partial z} - jk_x P_z \tag{3.13b}$$

$$\frac{j\omega}{c}Q_z = -\frac{\partial Q_y}{\partial x} + jk_x P_y \tag{3.13c}$$

Note that $\boldsymbol{P}$ and $\boldsymbol{Q}$ have same cell-to-cell field relationships as E and H at normal incidence. However this field transformation results in additional time derivatives of the right-hand sides of Eq. (3.12) and Eq. (3.13), which cannot be solved by the normal FDTD update methods.

The additional time derivatives can be removed by defining $\boldsymbol{P} = \boldsymbol{P}_a + \boldsymbol{P}_b$ and $\boldsymbol{Q} = \boldsymbol{Q}_a + \boldsymbol{Q}_b$; the "a" portions satisfy the standard Maxwell's equations and the "b" portions satisfy the remaining parts (additional time derivatives). Eq. 3.12 is split into

$$\frac{j\omega}{c}P_{xa} = -\kappa_{xx}\frac{\partial Q_y}{\partial z} + \kappa_{xy}(\frac{\partial Q_x}{\partial z} - \frac{\partial Q_z}{\partial x}) + \kappa_{xz}\frac{\partial Q_y}{\partial x} \tag{3.14a}$$

$$\frac{j\omega}{c}P_{ya} = -\kappa_{yx}\frac{\partial Q_y}{\partial z} + \kappa_{yy}(\frac{\partial Q_x}{\partial z} - \frac{\partial Q_z}{\partial x}) + \kappa_{yz}\frac{\partial Q_y}{\partial x} \tag{3.14b}$$

$$\frac{j\omega}{c}P_{za} = -\kappa_{zx}\frac{\partial Q_y}{\partial z} + \kappa_{zy}(\frac{\partial Q_x}{\partial z} - \frac{\partial Q_z}{\partial x}) + \kappa_{zz}\frac{\partial Q_y}{\partial x} \tag{3.14c}$$

and

$$P_{xb} = \sin\theta_{inc}(\kappa_{xy}Q_z - \kappa_{xz}Q_y) \tag{3.15a}$$

$$P_{yb} = \sin\theta_{inc}(\kappa_{yy}Q_z - \kappa_{yz}Q_y) \tag{3.15b}$$

$$P_{zb} = \sin\theta_{inc}(\kappa_{zy}Q_z - \kappa_{zz}Q_y) \tag{3.15c}$$

Split equations for "$\boldsymbol{Q}$" field components can be written in a similar way.

$$\frac{j\omega}{c}Q_{xa} = \frac{\partial P_y}{\partial z} \tag{3.16a}$$

$$\frac{j\omega}{c}Q_{ya} = -\frac{\partial P_x}{\partial z} + \frac{\partial P_z}{\partial x} \tag{3.16b}$$

$$\frac{j\omega}{c}Q_{za} = -\frac{\partial P_y}{\partial x} \tag{3.16c}$$

and

$$Q_{xb} = 0 \tag{3.17a}$$

$$Q_{yb} = -\sin\theta_{inc} P_z \tag{3.17b}$$

$$Q_{zb} = \sin\theta_{inc} P_y \tag{3.17c}$$

As an indicative example, the discrete form of Eq. 3.14a can be expressed as follows:

$$\begin{aligned} P^{n+1}_{xa(i+1/2,k)} &= P^{n}_{xa(i+1/2,k)} \\ &- S\kappa_{xx}\left(Q^{n+1/2}_{y(i+1/2,k+1/2)} - Q^{n+1/2}_{y(i+1/2,k-1/2)}\right) \\ &+ \frac{1}{2}S\kappa_{xy}\left(Q^{n+1/2}_{x(i,k+1/2)} + Q^{n+1/2}_{x(i+1,k+1/2)} - Q^{n+1/2}_{x(i,k-1/2)} - Q^{n+1/2}_{x(i+1,k-1/2)}\right) \\ &- \frac{1}{2}S\kappa_{xy}\left(Q^{n+1/2}_{z(i+3/2,k)} - Q^{n+1/2}_{z(i-1/2,k)}\right) \\ &+ \frac{1}{4}S\kappa_{xz}\left(Q^{n+1/2}_{y(i+3/2,k-1/2)} + Q^{n+1/2}_{y(i+3/2,k+1/2)} - Q^{n+1/2}_{y(i-1/2,k-1/2)} - Q^{n+1/2}_{y(i-1/2,k+1/2)}\right) \end{aligned} \tag{3.18}$$

where the subscripts 'i' and 'k' represent the grid location in the x-axis and z-axis, and the superscript 'n' denotes a discretized time-step. A constant S, known as the Courant stability factor, is given by $c\Delta t/\Delta u$. Similarly, the discrete form of Eq. 3.15a can be written as:

$$P^{n+1}_{xb(i+1/2,k)} = \sin\theta_{inc}\left[\kappa_{xy} Q^{n+1}_{z(i+1/2,k)} - \frac{1}{2}\kappa_{xz}\left(Q^{n+1}_{y(i+1/2,k-1/2)} + Q^{n+1}_{y(i+1/2,k+1/2)}\right)\right] \tag{3.19}$$

The "a" fields can be updated from the initial values of the total fields. However, the "b" components must be removed in a proper way because of their temporal dependency to the total fields. One effective way is to express Q_z using "a" components by manipulating Eqs. 3.14 - 3.17. The first step is to find P_z by substituting P_{zb} using Eq. 3.15c and separating Q_y into the "a" and "b" portions.

$$\begin{aligned} P_z &= P_{za} + P_{zb} \\ &= P_{za} + \sin\theta_{inc}\left(\kappa_{zy} Q_z - \kappa_{zz} Q_y\right) \\ &= P_{za} + \sin\theta_{inc}\left[\kappa_{zy} Q_z - \kappa_{zz}\left(Q_{ya} - \sin\theta_{inc} P_z\right)\right] \end{aligned} \tag{3.20}$$

Then, we summarize it for P_z as follows:

$$P_z = \frac{1}{A}\left[P_{za} + \sin\theta_{inc}\left(\kappa_{zy} Q_z - \kappa_{zz} Q_{ya}\right)\right] \tag{3.21}$$

where $A = 1 - \kappa_{zz} \sin^2 \theta_{inc}$. Similarly, we solve for Q_z by substituting Q_{zb} with Eq 3.17c.

$$Q_z = Q_{za} + \sin\theta_{inc}\kappa_{zz} \left[P_{ya} + \sin_{\theta_{inc}} \left(\kappa_{yy} Q_z - \kappa_{yz} Q_y\right)\right] \tag{3.22}$$

Again, splitting Q_y into "a" and "b" portions, the field Q_z is expressed:

$$Q_z = Q_{za} + \sin\theta_{inc}\kappa_{zz} \left\{P_{ya} + \sin_{\theta_{inc}} \left[\kappa_{yy} Q_z - \kappa_{yz} \left(Q_{ya} - \sin\theta_{inc} P_z\right)\right]\right\} \tag{3.23}$$

Now, the total field Q_z is found to be expressed using the newly updated "a" fields:

$$Q_z = \frac{1}{D}\left(Q_{za} + \sin\theta_{inc} P_{ya} + \frac{B}{A} P_{za} + C Q_{ya}\right) \tag{3.24}$$

where $B = \kappa_{yz} \sin^3 \theta_{inc}$, $C = (1/A)\kappa_{yz} \sin^2 \theta_{inc}$, and $D = 1 - (B/A)\kappa_{zy} \sin\theta_{inc} - \kappa_{yy} \sin^2 \theta_{inc}$. P_z can be found using Q_z and other total fields can be updated using P_z and Q_z as follows:

$$P_z = \frac{1}{A}\left[P_{za} + \sin\theta_{inc}\left(\kappa_{zy} Q_z - \kappa_{zz} Q_{ya}\right)\right] \tag{3.25a}$$

$$Q_x = Q_{xa} \tag{3.25b}$$

$$Q_y = Q_{ya} - \sin\theta_{inc} P_z \tag{3.25c}$$

$$P_x = P_{xa} + \sin\theta_{inc}\left(\kappa_{xy} Q_x - \kappa_{xz} Q_z\right) \tag{3.25d}$$

$$P_y = P_{ya} + \sin\theta_{inc}\left(\kappa_{yy} Q_x - \kappa_{yz} Q_z\right) \tag{3.25e}$$

In the split-field update method, P and Q fields should be updated simultaneously. Field values at every integer and half time-step need to be stored in different variables. First, the "a" portions of the field variables are updated by previously stored field values, and then total fields can be determined by using the values of "a" portions at the same time-step. The discrete form of Eq. 3.24 can be written as:

$$\begin{aligned} Q^{n+1}_{z(i+1/2,k)} = {} & \frac{1}{D} Q^{n+1}_{za(i+1/2,k)} \\ & + \frac{1}{2D}\sin\theta_{inc}\left(P^{n+1}_{ya(i,k)} + P^{n+1}_{ya(i+1,k)}\right) \\ & + \frac{B}{4AD}\left(P^{n+1}_{za(i,k-1/2)} + P^{n+1}_{za(i,k+1/2)} + P^{n+1}_{za(i+1,k-1/2)} + P^{n+1}_{za(i+1,k+1/2)}\right) \\ & + \frac{C}{2D}\left(Q^{n+1}_{ya(i+1/2,k-1/2)} + Q^{n+1}_{ya(i+1/2,k+1/2)}\right) \end{aligned} \tag{3.26}$$

The complete FDTD formulations for all P and Q field components in the discrete form are presented in Appendix A. A package of computer code for the FDTD simulation has been written in the standard C/C^{++} language.

3.3 Absorbing Boundary Conditions: UPML Approach

Another important aspect for a robust FDTD method implementation is space truncation. Finite computation area inevitably causes electromagnetic wave interaction problems in unbounded regions. An absorbing boundary condition (ABC) artificially extends the lattice to infinity and removes such problems. ABC can be implemented by analytical methods [39]. Another effective method to implement absorbing boundary conditions is to use a 'Perfectly Matched Layer' (PML), introduced by J. P. Berenger [40, 41]. In brief, PML addresses highly absorbing but non reflective media at boundaries. The PML approach has been proven to perform the best as an absorbing boundary without generating reflections. A number of PML techniques have been proposed by others [42–44].

One successful alternative is the 'Uniaxial Perfectly Matched Layer' (UPML) using anisotropic media [45, 46]. The UPML gives a physical picture of PML ABC because it is based on a Maxwellian formulation rather than a mathematical model. The UPML can be easily implemented within the split-field FDTD method. Note that only two PML slabs need to be placed normal to the z-axis when the structure has a periodicity along the x-axis. In this case, The UPML has material properties

$$\frac{\epsilon}{\epsilon_0} = \frac{\mu}{\mu_0} = \begin{bmatrix} 1/s_x & 0 & 0 \\ 0 & s_x & 0 \\ 0 & 0 & s_x \end{bmatrix} \tag{3.27}$$

where $s_x = 1 + \chi c/j\omega$. To minimize reflection at the interface between the free space and the UPML regions, tapering of χ is needed [47].

3.4 Numerical Dispersion and Stability

The FDTD method is based on sampling and updating the electric and magnetic field in time and space. The discrete nature of the FDTD results in some restrictions, namely, numerical dispersion and stability.

3.4.1 Numerical Dispersion

The discrete grid-space and central difference approximations in the FDTD algorithm cause nonphysical dispersion of the simulated waves; a numerical wave propagates

at a different phase velocity depending on its propagation direction with respect to the major axes in the computational lattice. This phenomenon can be depicted by embedding the computational space in 'numerical aether' having properties very close to a vacuum. This effect results in a 'numerical dispersion' error. Also the finite grid spacing results in anisotropic properties of numerical dispersion. In other words, the phase velocity of the numerical wave can differ from its propagation direction. The numerical wave number k_{num} at a certain angle with respect to the major grid axes can be numerically calculated by repeating the following equation until convergence [18]:

$$k_{l+1} = k_l - \frac{\sin^2\left(\frac{k_l \Delta u \cos\theta_p}{2\lambda}\right) + \sin^2\left(\frac{k_l \Delta u \sin\theta_p}{2\lambda}\right) - \frac{1}{S^2}\sin^2\left(\frac{\pi S}{N}\right)}{\frac{\Delta u \cos\theta_p}{2\lambda}\sin\left(\frac{k_l \Delta u \cos\theta_p}{\lambda}\right) + \frac{\Delta u \sin\theta_p}{2\lambda}\sin\left(\frac{k_l \Delta u \sin\theta_p}{\lambda}\right)} \tag{3.28}$$

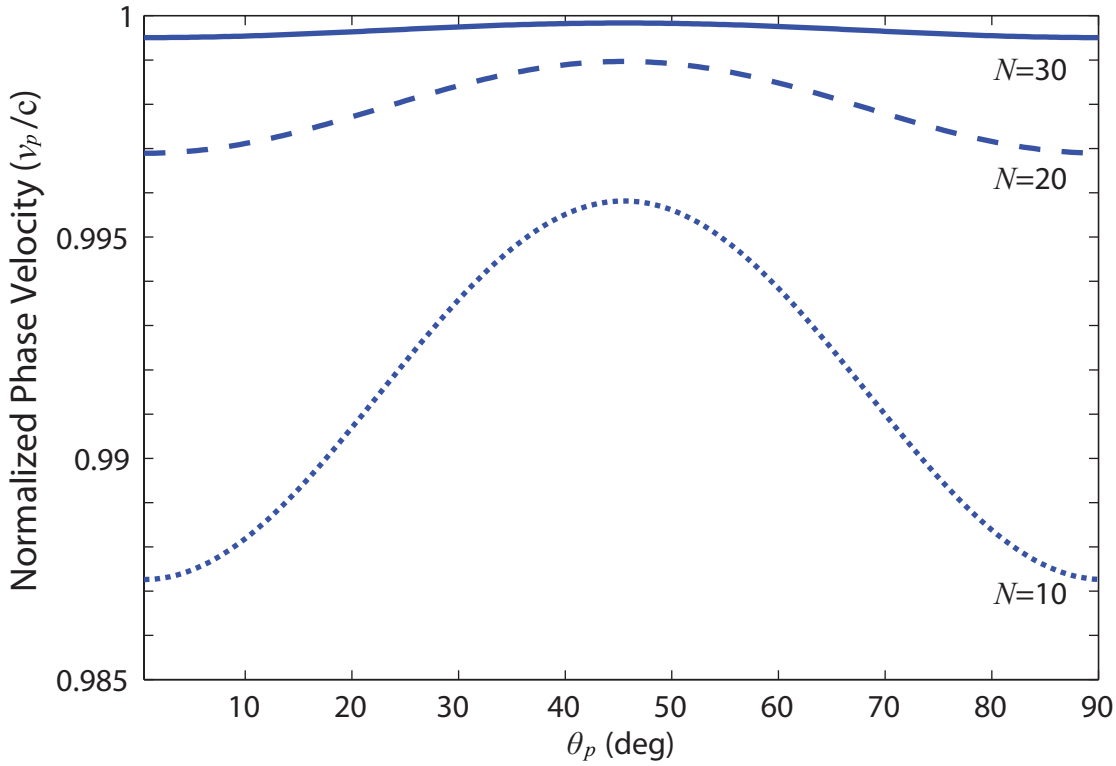


Figure 3.4: Variation of the numerical phase velocity depending on the propagation direction for three sampling densities ($N = 10, 20, 30$) in a uniform square-cell grid

where k_{l+1} is the improved value of k_l, θ_p is the propagation angle, and the grid density $N = \lambda/\Delta u$. The final value k_{num} can be obtained by increasing l. The numerical phase velocity is given by:

$$v_p = \frac{2\pi}{k_{num}} c \tag{3.29}$$

where c is the speed of light in a vacuum. A smaller grid spacing (a large value of N) can relieve the numerical dispersion error as shown in Fig. 3.4. However, finer grids require more computation and memory capacity. N is selected between 10 and 20 for the shortest wavelength or the smallest feature size. The FDTD algorithm for periodic anisotropic structures in Section 3.2 requires roughly double the number of N for the same numerical accuracy of the normal FDTD methods due to additional spatial averaging. Higher order approximations or a hexagonal grid-space can be employed to improve the numerical wave properties [18].

3.4.2 Stability Limit (Courant Stability Factor)

The time step Δt has a special bound relative to the grid spacing Δu to avoid numerical instability. The critical value for the stability limit is called the 'Courant stability factor' (S). The upper bound of the Courant factor for the original Yee algorithm in the M-dimension is given by:

$$S \leq 1/\sqrt{M} \tag{3.30}$$

where M is 1, 2, or 3. The time step should be selected below the stability limit.

$$\Delta t = \frac{\Delta u}{c} S \leq \frac{\Delta u}{c} S_{max} \tag{3.31}$$

The numerical characteristics of the split-field method differ from those of the original Yee algorithm in that the stability limit is highly dependent on the incident angle. A. Roden derived the upper bound of the stability limit of the split-field method to be:

$$S \leq \frac{\cos^2 \theta_{inc}}{\sqrt{1 + \cos^2 \theta_{inc}}} \tag{3.32}$$

Fig. 3.5 shows the stability limit for split-field method as a function of the angle of incidence.

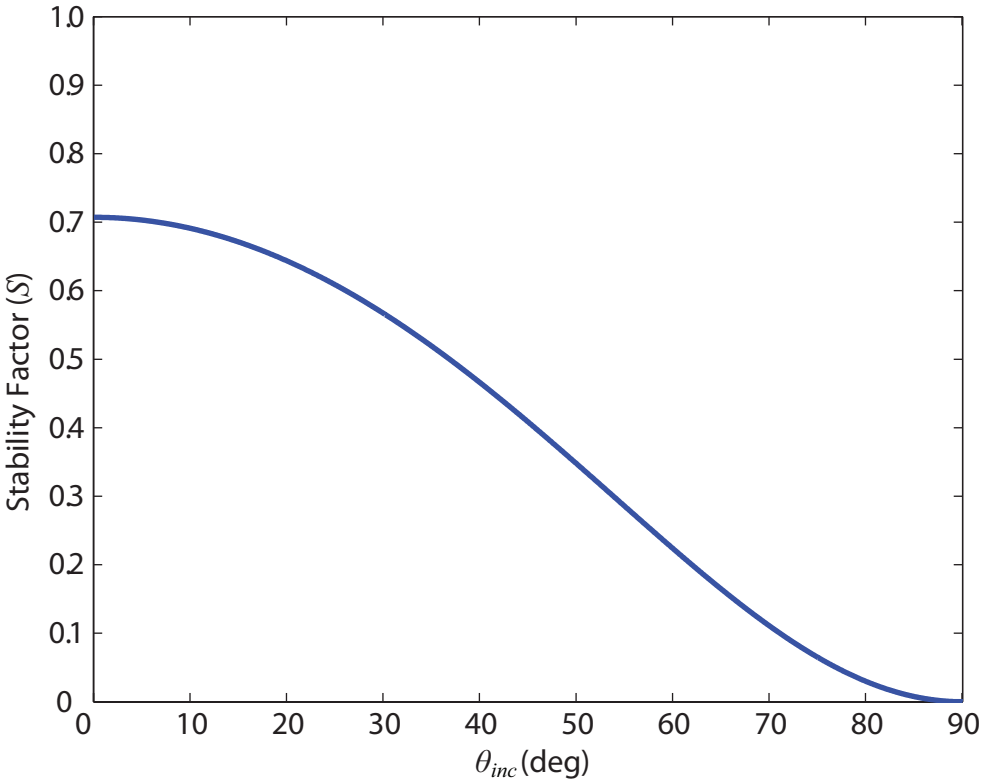


Figure 3.5: Stability limit for the split-field technique in two dimensions

3.5 Wide-band Source and Vectorial Far-field Transformation

There are two methods of input excitation: using a continuous wave (CW) or employing a time-limited pulse wave. The CW FDTD solution can be found in the steady state for sinusoidal illumination. A general form of the input sine wave is given by:

$$\boldsymbol{P}_{inc} = \boldsymbol{P}_0 \exp(j\omega_0 t) \tag{3.33}$$

where ω_0 is the center angular frequency and $\boldsymbol{P}_0 = \hat{\mathbf{x}} P_x \exp(j\varphi_x) + \hat{\mathbf{y}} P_y \exp(j\varphi_y)$. The complex amplitudes P_x and P_y and the phase difference $(\varphi_y - \varphi_x)$ determine the polarization of the input wave. Note that the angle of incidence is already included in $\boldsymbol{P}_0$ so its

propagation vector is always parallel to the z-axis. A pulsed plane wave excitation can be applied to obtain a spectral response from a single FDTD simulation while the CW method requires an individual FDTD simulation for each frequency of interest. A gaussian pulse is widely used for pulsed FDTD:

$$\boldsymbol{P}_{inc} = \boldsymbol{P}_0 \exp(j\omega_0 t) \exp\left[-\frac{(t-t_0)^2}{T^2}\right] \tag{3.34}$$

where t_0 is a time delay required to generate a smooth two-sided pulse and T determines the width of the pulse in time domain. The frequency information can be extracted by applying the discrete Fourier transformation (DFT) during time-marching in the FDTD simulation.

The phenomena in the far-field region are frequently of interest as well as in the near-field region. When a time-domain pulse is used for spectral analysis, the far-field information must be extracted from the near-field before sampling for the the DFT. The near-field to far-field transformation may then be applied (see Sec. 2.4.3). In the far-field region, a set of sinc functions appear as the Fourier components corresponding to the diffraction orders. When the structure has an infinite periodicity, a sum of the Fourier components yields discrete signals in the far-field region rather than a continuous pattern.

The far-field signals, often called Floquet modes, are governed by the diffraction equation:

$$\sin\theta_m = \frac{m\lambda}{\Lambda} + \sin\theta_{inc} \tag{3.35}$$

where λ is the wavelength of interest, Λ is the period, and m is an integer. The amplitude and phase of signals in each order m can be determined from the fields ($P_{l,near}$)on a single line in front of and behind the structure by applying the near-to-far transformation in the time-domain:

$$E^m_{l,far}(t) = \frac{1}{\Lambda}\int P_{l,near}(t,x)\exp\left(j\frac{2\pi m}{\Lambda}x\right)dx \tag{3.36}$$

where $l = x, y, z$.

One may find that enforcing Eq. 3.36 directly to each field component of the FDTD grid cells leads to considerable losses for orders whose diffraction angles are highly oblique since the expression is derived assuming small angles. The most accurate method is to set the near-fields always normal to the propagation vector of each order ($\hat{\mathbf{k}}_m$). A more

complete near-to-far transformation of the vector field is given by:

$$E_{m1,far}(t) = \frac{1}{\Lambda}\int \left[P_{x,near}(t,x)\cos\theta'_m - P_{z,near}(t,x)\sin\theta'_m\right]\exp\left(j\frac{2\pi m}{\Lambda}x\right)dx \tag{3.37a}$$

$$E_{m2,far}(t) = \frac{1}{\Lambda}\int P_{y,near}(t,x)\exp\left(j\frac{2\pi m}{\Lambda}x\right)dx \tag{3.37b}$$

where $E_{m1,far}$ and $E_{m2,far}$ are field components corresponding to the identical vectors normal to $\hat{\mathbf{k}}_m$, and $\sin\theta'_m = (m\lambda/\Lambda)$. Note that $\hat{\mathbf{y}}$ is always perpendicular to $\hat{\mathbf{k}}_m$ due to the two dimensional nature of problems. The FDTD formulation for Eq. 3.37 can be written as follows:

$$E^n_{m1,far} = \frac{1}{N}\sum_{i=0}^{N}\left[\frac{\cos\theta'_m}{2}\left(P^n_{x(i-1/2,k_1)} + P^n_{x(i+1/2,k_1)}\right) - \frac{\sin\theta'_m}{2}\left(P^n_{z(i,k_1-1/2)} + P^n_{z(i,k_1+1/2)}\right)\right] \tag{3.38a}$$

$$\times \exp\left(j\frac{2\pi mi}{N}\right)$$

$$E^n_{m2,far} = \frac{1}{N}\sum_{i=0}^{N} P^n_{y(i,k_1)}\exp\left(j\frac{2\pi mi}{N}\right) \tag{3.38b}$$

where $N = \Lambda/\Delta u$, often called the grid density, and $k = k_1$ is the sampling line of the near-field values.

Chapter 4

Validation of the FDTD Method

The FDTD algorithm, described in Section 3.2, can be applied to arbitrary periodic media in cases of both normal and oblique incidence. This chapter presents the comparison of FDTD results with results from well-known analytical or numerical methods such as the rigorous coupled-wave (RCW) theory and the Berreman method. To this end, four different structures will be discussed: thin phase gratings, dielectric stacks, twist-nematic liquid crystal cells, and optically active media.

4.1 Thin Phase Gratings

Applying the FDTD method to the traditional grating problems can be the simplest way to verify the FDTD algorithm, though the FDTD method is not limited to isotropic media. We test the diffraction properties of a binary grating with rectangular grooves. The FDTD results of diffraction efficiencies for the normal incidence case and a sampled incident angle (30°) are compared with the results from RCW analysis as well as analytical solutions.

Fig. 4.1 illustrates a two dimensional FDTD simulation space for grating analysis. Two boundaries along the x axis were treated by periodic boundary conditions. The other two boundaries along the z axis must be terminated in a proper way to avoid artificial reflections. To this end, uniaxial perfectly matched layers (PML) [45] were placed at both

Table 4.1: FDTD Simulation Parameters

Parameters	Normalized Value	Sampled Value
Spatial resolution ($\Delta x = \Delta z$)	$\lambda_o/40$	$20nm$
Temporal resolution (Δt)	$\Delta x/3c$	$0.022fs$
Gaussian pulse width (T)	$50\Delta t$	$0.11fs$
PML thickness	$40\Delta x$	$800nm$

boundaries. The FDTD simulation parameters are summarized in Table 4.1.

Recalling Eq.2.47, the analytic solutions for the m^{th} order diffraction efficiency of a thin binary grating are:

$$\eta_m = \begin{cases} \cos^2\varphi & \text{for the } 0^{th} \text{ order} \\ \frac{4\sin^2\varphi}{(m\pi)^2} & \text{for the } m^{th} \text{ order} \end{cases} \tag{4.1}$$

where the phase angle φ is $\frac{\pi n_1 d}{\lambda \cos\theta_g}$; θ_g is the refractive angle of the grating, which satisfies

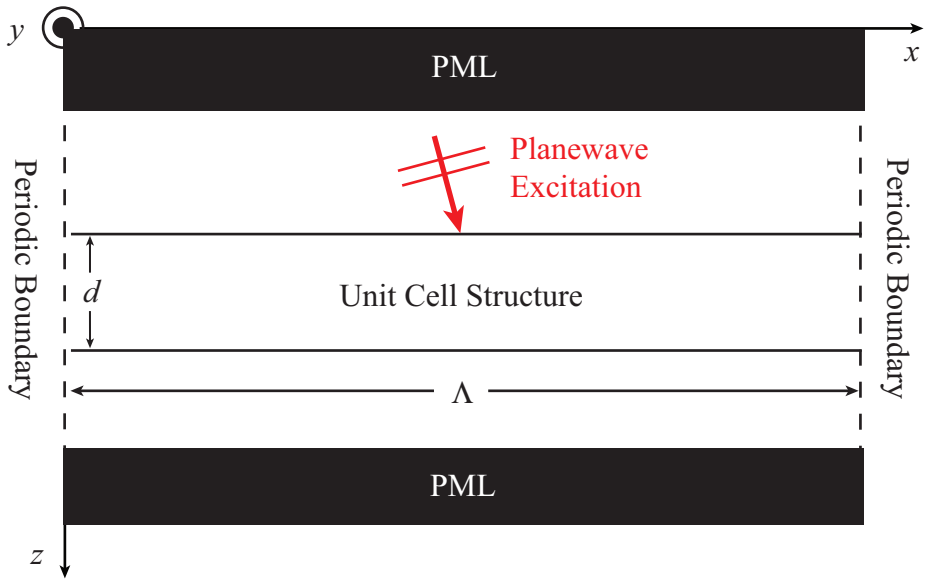


Figure 4.1: Schematic of FDTD simulation space. Λ is the grating pitch and d is the grating thickness.

$\bar{n}\sin\theta_g = n_0\sin\theta_{inc}$. Note that Eq. 4.1 is a even function; $\eta_{\pm 1}$ are identical. Fig. 4.2 shows the diffraction efficiencies of a sinusoidal phase grating at normal incidence with the following grating parameters: the grating pitch $\Lambda = 10\lambda$, the average index $n_0 = 1.5$, the modulation index $n_1 = 0.5$, and the fill factor $f_t = 0.5$. The incident polarization is linear and perpendicular to the plane of the propagation vector and the grating vector.

The FDTD results for diffraction efficiencies at normal incidence in Fig. 4.2 show a good agreement with the analytical expressions given in Eq. 4.1. Small losses in efficiencies are observed as a consequence of reflections at air-grating interfaces. Note that this thin grating may have many diffracted orders up to $\pm 19^{th}$, determined by the grating equation given in Eq. 2.40.

The analytical solutions given in Eq. 4.1 for diffraction efficiencies are simple and effective in most cases. Those expressions, however, are no longer valid at highly oblique incidence where the paraxial approximation fails. In addition, they cannot account for the coupling effects between higher orders. The rigorous coupled-wave (RCW) analysis [27, 28, 48, 49] can be applied to get accurate predictions for the diffraction efficiencies at oblique incidence. We calculated the diffraction efficiencies of the same binary grating but at 30° of incidence. The results from the FDTD and the RCW theory appear in Fig. 4.3. The FDTD results agree with the expectations of the RCWA method. The FDTD results show excellent agreement with the RCW analysis.

We note that the FDTD results appear to be slightly shifted to longer wavelengths for high frequencies, which shows the characteristic numerical dispersion of the FDTD method. A denser grid resolution may improve these numerical errors, but with cost of more computation and memory capacity.

Easy visualization of wave motions is one of the advantages of the FDTD method. Fig. 4.4 shows the snap shots of the electric field at both normal and 30° incidence.

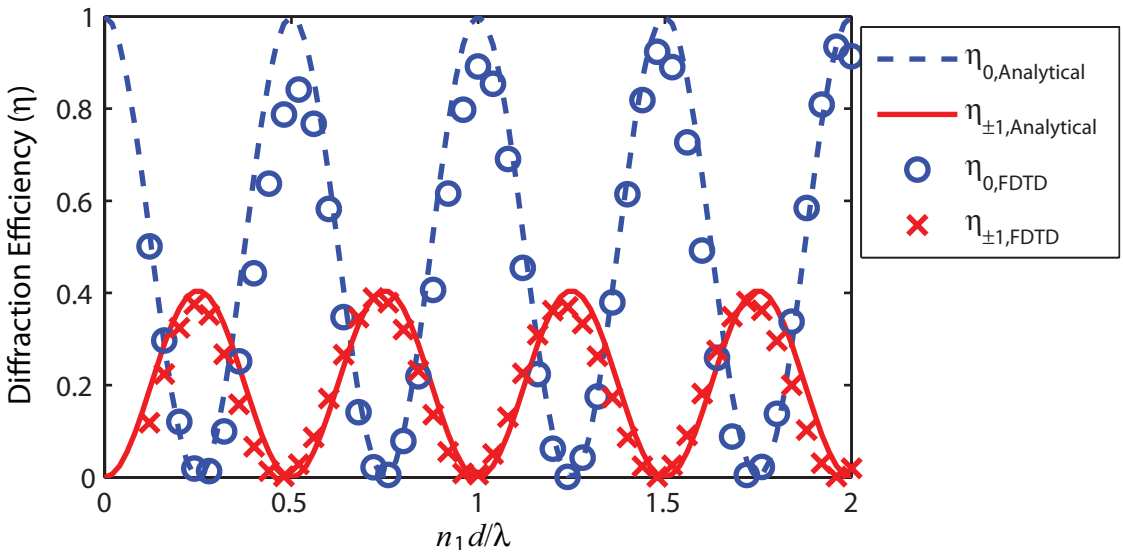


Figure 4.2: Diffraction efficiencies of a binary rectangular grating at normal incidence as a function of $n_1 d/\lambda$. The grating parameters are $\Lambda = 10\lambda$, $\bar{n} = 1.5$, $n_1 = 0.5$, and $f_t = 0.5$.

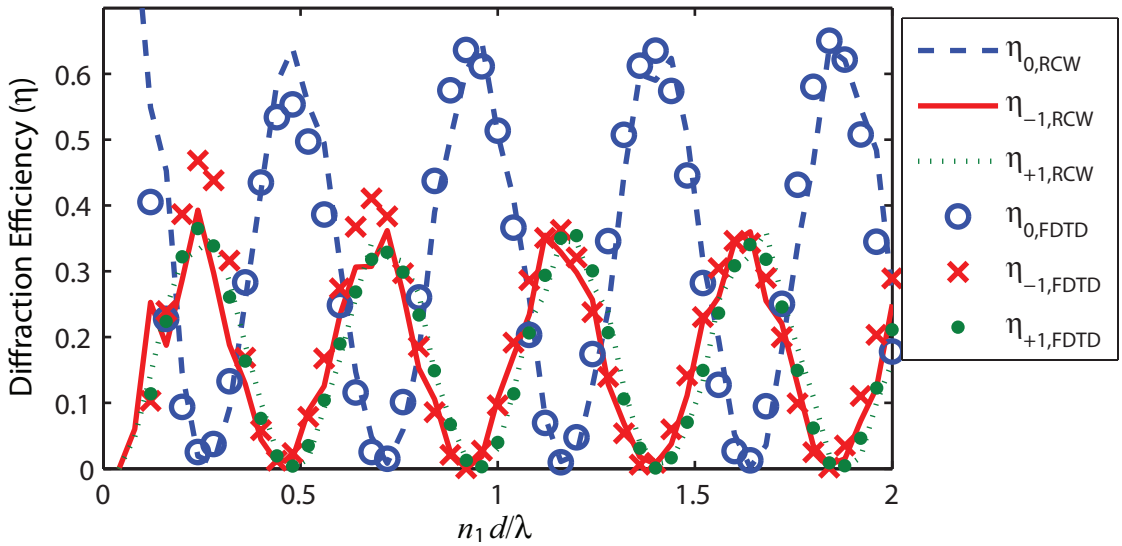
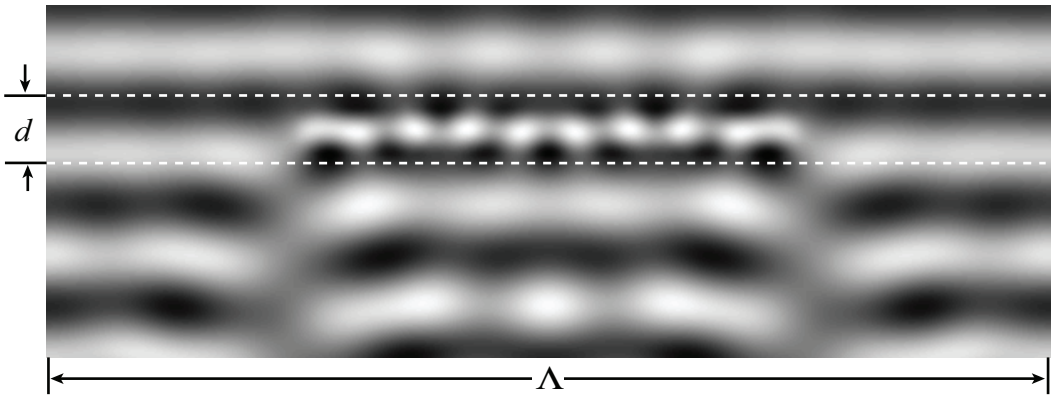
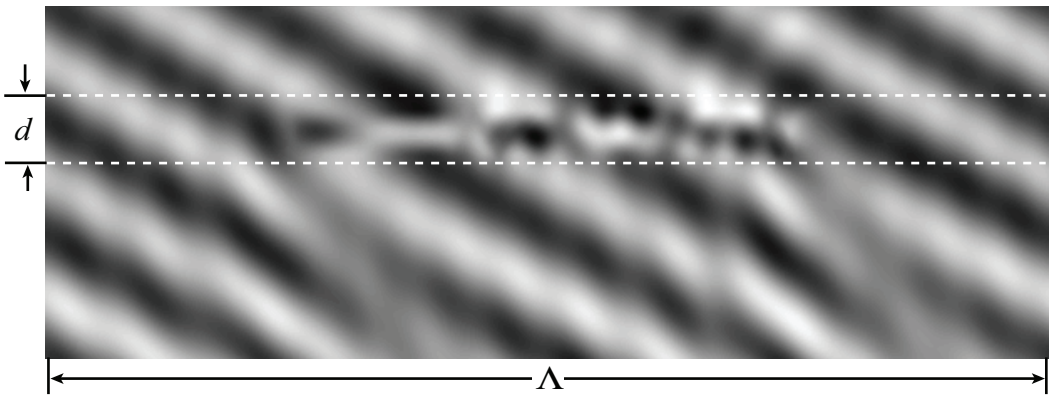


Figure 4.3: Diffraction efficiencies of a binary thin grating at 30° of incidence as a function of $n_1 d/\lambda$. The grating parameters are $\Lambda = 10\lambda$, $\bar{n} = 1.5$, $n_1 = 0.5$, and $f_t = 0.5$.



(a) Near-field image of the electric field at normal incidence



(b) Near-field image of the electric field at 30° incidence

Figure 4.4: Near-field images of the electric field at (a) $\theta_{inc} = 0$ and (b) $\theta_{inc} = 30°$ for a binary rectangular grating, whose parameters are $\Lambda = 10\lambda$, $\bar{n} = 1.5$, $n_1 = 0.5$, $d = 0.5\lambda$ and $f_t = 0.5$.

4.2 Dielectric Stacks as a Photonic Band Filter

Another interesting structure to analyze is one composed of multiple stacks of different dielectric layers. These stratified structures can perform optical filtering as a one dimensional photonic crystal [50, 51]. We consider a simple stack of dielectric layers with two different refractive indices as shown in Fig. 4.5. The total thickness is 5Λ, where $\Lambda = 1\mu$ and the fill factor $f_t = 0.5$. The refractive indices of each layer are designed for $n_1 = 1$ and $n_2 = 5$.

Transmittance is calculated by the FDTD simulations at both normal and 30° of incidence as a function of frequency. For comparison, we apply the Berreman 4×4 matrix method to the same structure. The results from FDTD simulations in Fig. 4.6 and 4.7 show an excellent agreement with the Berreman method.

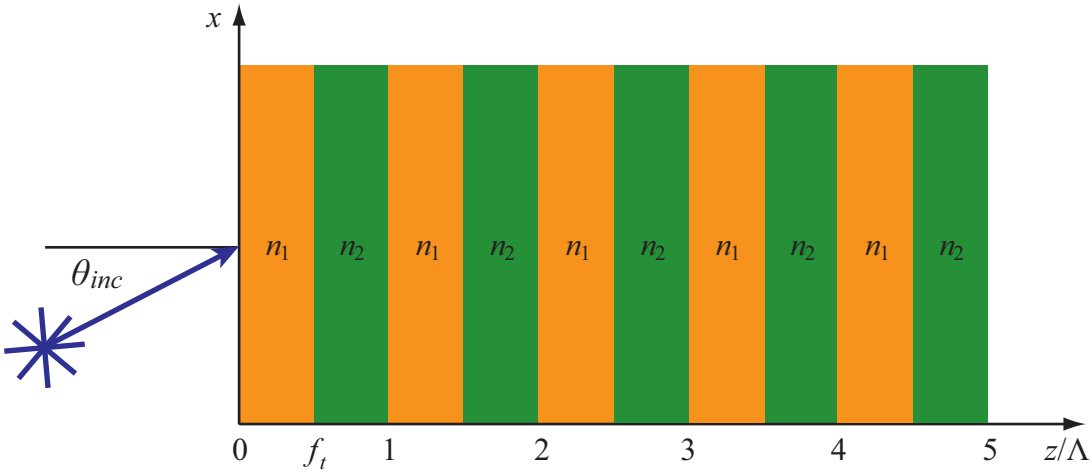


Figure 4.5: Schematic view of a simple stack of dielectric layers with two different refractive indices ($n_1 = 1$, $n_2 = 5$) as a one dimensional photonic bandgap structure. The length of each period $\Lambda = 1um$ and the fill factor $f_t = 0.5$

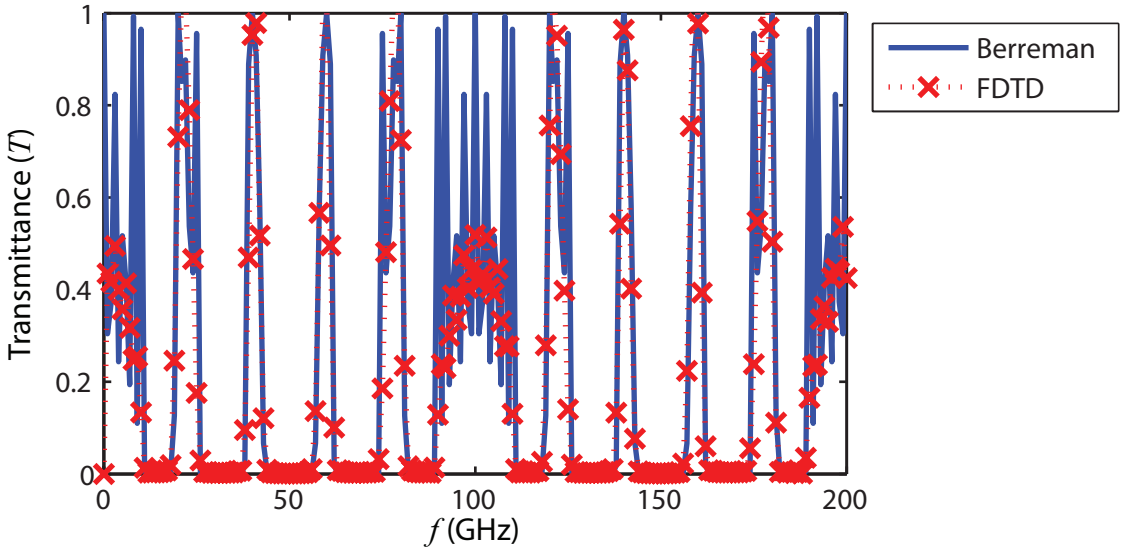


Figure 4.6: Transmittance of a simple stack of dielectric layers with two different refractive indices ($n_1 = 1$, $n_2 = 5$) at normal incidence. The length of period $\Lambda = 1\mu m$ and the fill factor $f_t = 0.5$.

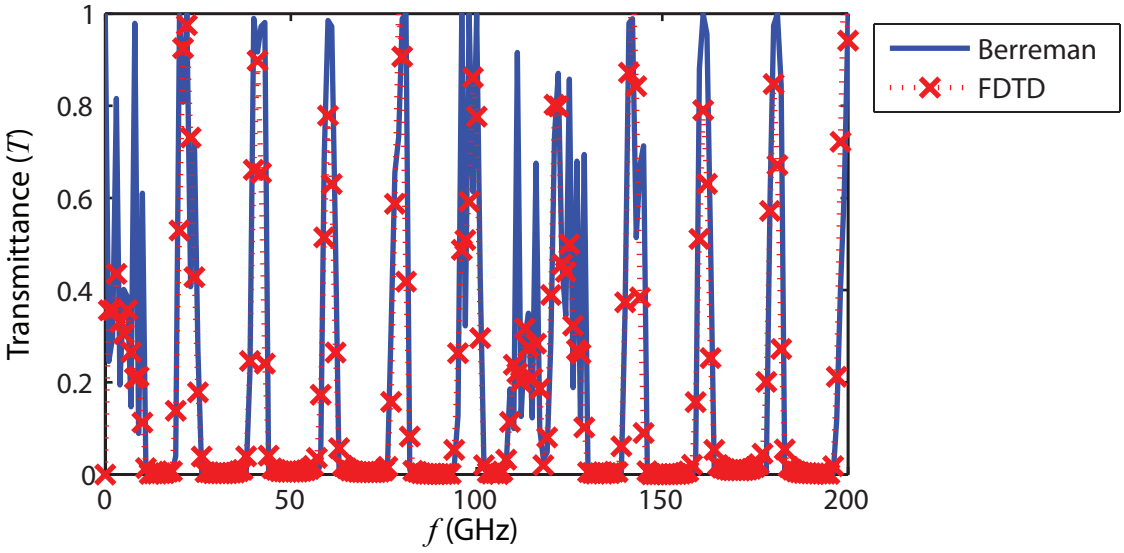


Figure 4.7: Transmittance of a simple dielectric stack with two different refractive indices ($n_1 = 1$, $n_2 = 5$) at 30° incidence. The length of period $\Lambda = 1\mu m$ and the fill factor $f_t = 0.5$.

4.3 Twisted Nematic Liquid Crystal Cells

Twisted nematic (TN) liquid crystal (LC) cells are widely used as a light valve for flat panel displays. Waveguiding occurs as light propagates in the LC cell when $\phi_{twist} \ll \pi\Delta n_l d/\lambda$ (Δn_l: birefringence of LC material, d: cell thickness, and ϕ_{twist}: twist angle), referred to as the *Mauguin limit* [52]. Consider a TN LC cell between ideal cross polarizers as shown in Fig. 4.8. The transmittance at the analyzer was derived by Gooch and Tarry [53].

$$T = 1 - \frac{\sin^2\left(\pi\sqrt{0.25+u^2}\right)}{2(1+4u^2)} \tag{4.2}$$

where $u = \Delta n_l d/\lambda$. A perfect 90° rotation of linear polarization can be achieved under the special conditions.

$$\Gamma(\lambda) = \sqrt{0.25+u^2} = 1, 2, 3, \ldots \tag{4.3}$$

90°-TN LC structures can be easily tacked in the FDTD grid-space by defining a permittivity tensor in Eq. 2.25 by $n_{\|} = 1.5$, $\Delta n_l = 0.2$, and $\phi(z) = (z/d)\phi_{twist}$ where $\phi_{twist} = 90°$. Gradient-index anti-reflection coatings with a parabolic profile [54] are employed to eliminate reflections at the air-LC interfaces.

Fig. 4.9 shows the FDTD predictions for the transmittance (T) after the analyzing polarizer. The polarization state of transmitted light before the analyzing polarizer is described in Fig. 4.10 in terms of the normalized Stokes parameters. An excellent agreement is found.

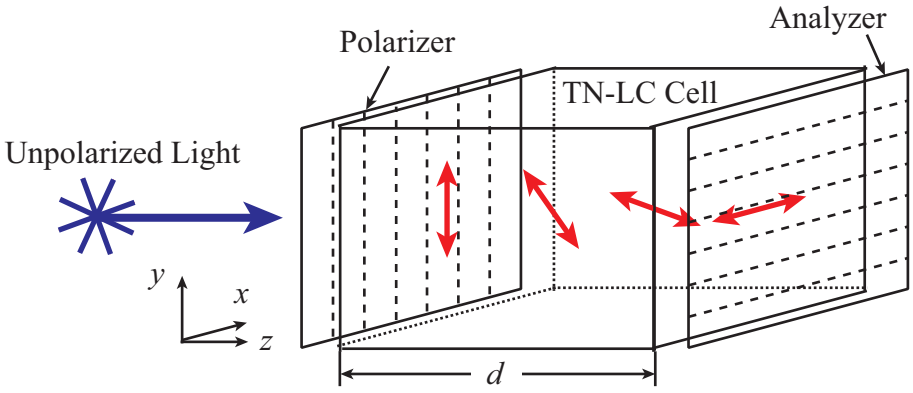


Figure 4.8: Schematic view of a 90°-twisted nematic liquid crystal cell between cross-polarizers; arrows depict nematic directors of liquid crystals. d is the thickness of the LC cell.

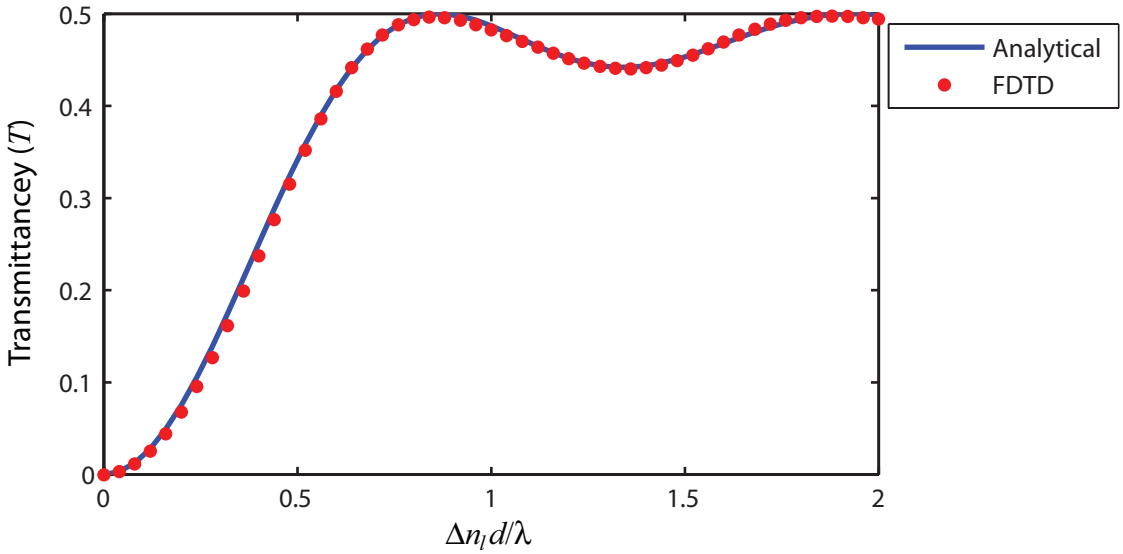


Figure 4.9: Transmittance through the 90°-twisted-nematic cell with ideal cross-polarizers as a function of the normalized retardation $\Delta n_l d/\lambda$. The parameters for LC materials are$\Delta n_0 = 1.6$ and $\Delta n_l = 0.2$.

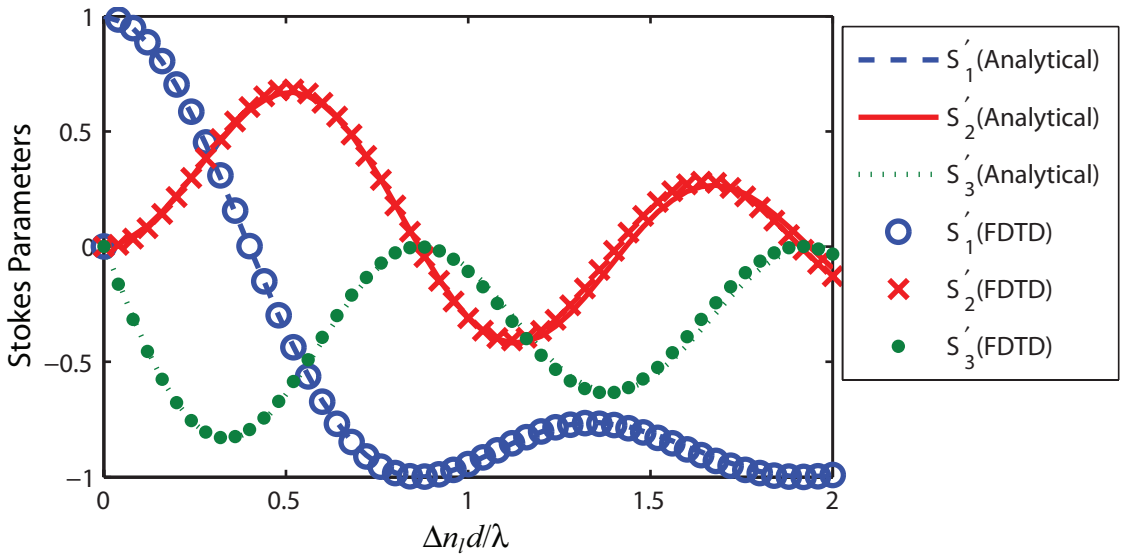


Figure 4.10: The normalized Stokes parameters for transmitted light polarization of the 90°-twisted-nematic cell. The Stokes parameters are measured before the analyzing polarizer. The parameters for LC materials are$\Delta n_0 = 1.6$ and $\Delta n_l = 0.2$.

4.4 Optically Active Media

The rotation of polarization can also be achieved by optical activity. An ideal rotation of the polarization plane is given by $\delta_r d$, where $\delta_r = \Delta n_c \pi/\lambda$ and d is the thickness of an optically active medium. The polarization of light will rotate linearly while propagating along the optic axis. Since we are most interested in the polarization properties, the Stokes parameters will be discussed.

We consider a slab of optically active media with circular birefringence $\Delta n_c = 0.05$. When the incoming light polarization is linear and vertical ($S_1' = 1$), the normalized Stokes parameters for the transmitted light are given by:

$$S_1' = \cos(2\pi u) \tag{4.4a}$$

$$S_2' = -\sin(2\pi u) \tag{4.4b}$$

$$S_3' = constant = 0 \tag{4.4c}$$

where $u = \Delta n_c d/\lambda$. The results obtained from the FDTD simulation show very good agreement with analytical solutions as shown in Fig. 4.11.

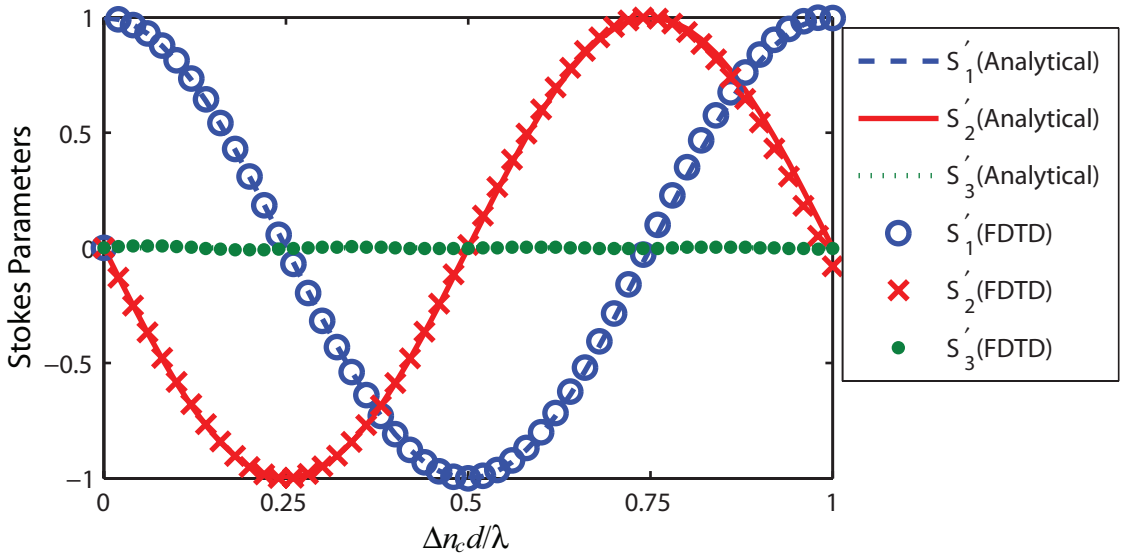


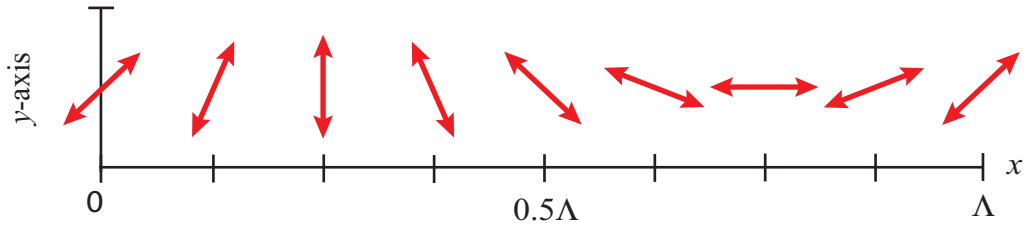
Figure 4.11: The normalized Stokes parameters for transmitted light polarization from a slab of optically active media with circular birefringence $\Delta n_c = 0.05$.

Chapter 5

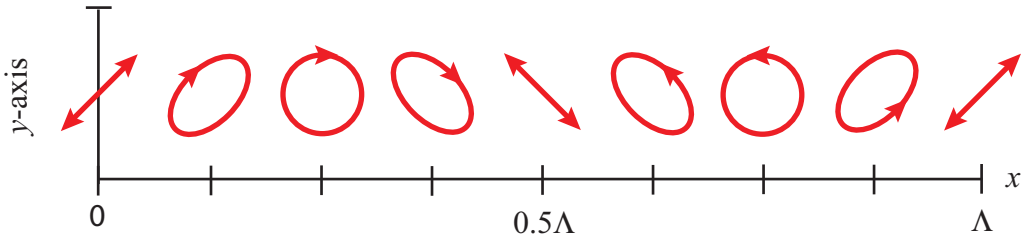
Numerical Analysis of Polarization Gratings

The Polarization Grating (PG) [3] is a polarization-selective optical element which can perform a periodic change of the polarization state of an incident beam. Since the first report of PGs appeared in Soviet journals [2], the diffraction properties of PG have been studied by many authors [3–5, 14–16, 55]. The periodically varying anisotropy leads to the unique optical properties of PGs; polarization dependent diffraction. The most distinct feature of a PG from conventional gratings is its Bragg property while it falls into the thin grating regime.

PGs can be realized using various technologies. The primary means for creating PGs is using polarizing holography with anisotropic organic recording materials (e.g. reactive mesogens and azobenzene containing polymers) [3, 4]. Recently effective fabrication techniques for creating high quality PGs using a combination of polarizing holograms and photo-alignment techniques were proposed [56–58]. A different PG realization is using subwavelength features to create gratings [59–61]. Structures smaller than wavelength can possess optical anisotropy, referred to as *form birefringence* [22], even in isotropic media. In a macroscopic view, there is no difference between holographic and subwavelength PGs, nonetheless they are quite different at the material level. We regard all of them as periodic



(a) Spatially varying anisotropy pattern of the linear PG



(b) Spatially varying anisotropy pattern of the elliptical PG

Figure 5.1: Two types of PGs: (a) linear PG; (b) elliptical PG. Λ is the optical pitch of anisotropy, which is a half of the periodicity (P/2), and the red arrows depict local anisotropy.

anisotropic media with a spatially varying anisotropy pattern.

The diffraction properties of PGs have been studied using the Jones matrix analysis [3, 14–16]. The Jones analysis yields simple analytic expressions for the diffraction characteristics of PGs in the ideal case (i.e. when the grating period is $\gg$ than the wavelength). However, this analysis is no longer valid where paraxial approximation fails. Moreover, it cannot tell the limit wherein crucial assumptions remain valid. For these limitations of analytical solutions, we apply the modified FDTD method as a tool of rigorous numerical analysis of PGs.

There are two primary types of PGs based on the periodic patterns of anisotropy. Fig. 5.1 illustrates different types of PGs. The first type of PG, labeled the "linear PG," has a spiral pattern of linear anisotropy; only linear birefringence is considered for this analysis. The second type of PG, labeled the "elliptical PG," has an anisotropy profile of both orientation and ellipticity varying with position. Two different cases of the elliptical PG can be identified by the presence of circular birefringence; the first case has only linear birefringence while the second case has both linear and circular birefringence.

Table 5.1: Parameters for linear and elliptical PG.

	Linear PG	Elliptical PG
ϕ	$\left(\frac{x}{\Lambda}+\frac{1}{4}\right)\pi$	$\frac{1}{4}\pi$
ϵ_x	$n_{\parallel}^2$	$\left[\frac{1}{2}\left(n_{\perp}+n_{\parallel}\right)+\frac{1}{2}\left(n_{\perp}+n_{\parallel}\right)\cos(\frac{2\pi}{\Lambda}x)\right]^2$
ϵ_y	$n_{\perp}^2$	$\left[\frac{1}{2}\left(n_{\perp}+n_{\parallel}\right)-\frac{1}{2}\left(n_{\perp}+n_{\parallel}\right)\cos(\frac{2\pi}{\Lambda}x)\right]^2$
ϵ_z	$n_{\perp}^2$	$n_{\perp}^2$
g	0	0 or $\frac{1}{2}\left(n_{\perp}+n_{\parallel}\right)n_c\sin(\frac{2\pi}{\Lambda}x)$

We consider a one dimensional anisotropic grating whose grating vector is parallel to the x direction. The permittivity tensor $\tilde{\epsilon}$ for PG is given by:

$$\tilde{\epsilon} = \mathbf{T}^{-1}(\phi)\begin{bmatrix} \epsilon_x & -i\epsilon_g & 0 \\ i\epsilon_g & \epsilon_y & 0 \\ 0 & 0 & \epsilon_z \end{bmatrix}\mathbf{T}(\phi) \tag{5.1}$$

where $\mathbf{T}$ is a rotational matrix in Eq. 2.27 and ϕ is the angle out of the z-x plane. The linear and elliptical profiles of the PG can be defined by the material parameters (ϕ, $\epsilon_{x,y,z}$, ϵ_g) as shown in Table 5.1.

5.1 FDTD Analysis of Optical Properties of PGs

We aim to better understand PGs using the FDTD method. First, we verify the FDTD results by comparing with the analytical expressions for the diffraction properties of PGs. Then we will answer the following questions. How does the diffraction of PG depend on grating geometry, material parameters, incident angle? To our knowledge, this is the first numerical study of the diffraction properties of PGs.

Note that all results of FDTD simulations are normalized by transmittance from a dielectric slab with the average index of PGs. In addition, graded-index anti-reflection (AR) coatings [54] are integrated with PGs to eliminate reflections at the interfaces between air and the face and back sides of grating structures.

5.1.1 Linear Polarization Gratings

In the ideal case, the Jones analysis produces very simple analytical expressions for diffraction efficiencies of linear PG [58].

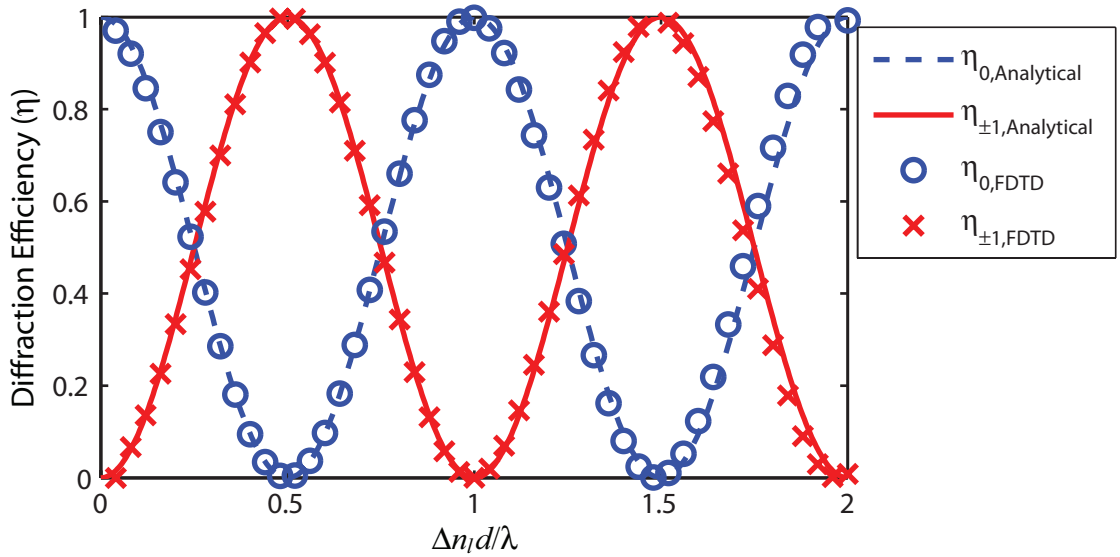
$$\eta_0 = \cos^2(\pi \Delta n_l d/\lambda) \tag{5.2a}$$

$$\eta_{\pm 1} = \frac{1 \mp S_3'}{2} \sin^2(\pi \Delta n_l d/\lambda) \tag{5.2b}$$

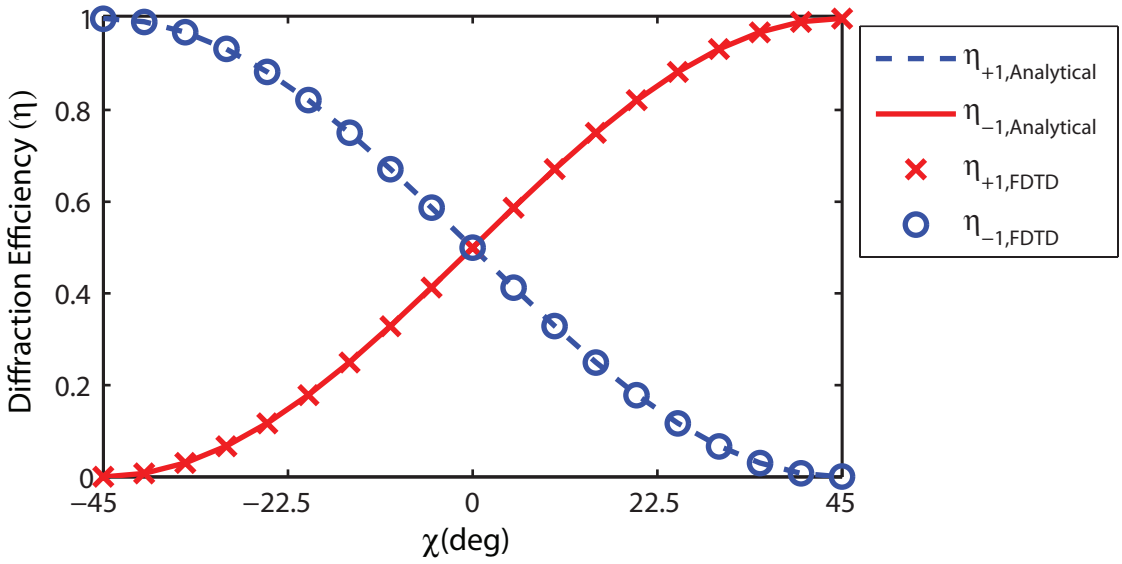
where the subscripts 0 and ± 1 correspond to the order of diffraction, $\Delta n_l = n_{\parallel} - n_{\perp}$ is linear birefringence, d is the grating thickness, and S_3' is a normalized Stokes parameter which describes the ellipticity of polarization states. Unlike thin phase gratings, only the 0^{th} and $\pm 1^{st}$ orders can exist in the diffraction of linear PGs. The 0^{th} order depends on the normalized retardation ($\Delta n_l d/\lambda$), but it is totally independent of the polarization state of input. On the other hand, the $\pm 1^{st}$ orders are sensitive to the input polarization as well as the normalized retardation.

For FDTD simulations, the grating parameters are chosen as: $\Lambda = 20\lambda$, $n_{\perp} = 1.5$, and $\Delta n_l = 0.2$. In Fig. 5.2 (a), the calculated diffraction efficiencies as a function of u from FDTD simulations are compared with analytical solutions from Eq. 5.2. The polarization state of the 0^{th} order is the same as the input polarization, but the $\pm 1^{st}$ orders have left-hand and right-hand circular polarization. The polarization properties of the $\pm 1^{st}$ orders are equivalent to the polarization state of orthogonal circular recording beams in the polarizing hologram corresponding to the anisotropy pattern of linear PGs as shown in Fig. 5.1(a).

Fig. 5.2 (b) illustrates the polarization response of diffraction orders from the linear PG. To investigate only the effect of input polarization, a sinusoidal input was enforced and the grating parameters were fixed for a half-wave retardation ($\Delta n_l d/\lambda = 1/2$), where the 0^{th} order disappears. The efficiencies of the $\pm 1^{st}$ orders alternatively vary with the angle of ellipticity (χ) of input polarization. The ellipticity angle χ can be translated to the normalized Stokes parameter $S_3' = \sin(2\chi)$. We note that the diffraction efficiencies do not respond to the variation in the orientation angle of the polarization ellipse.

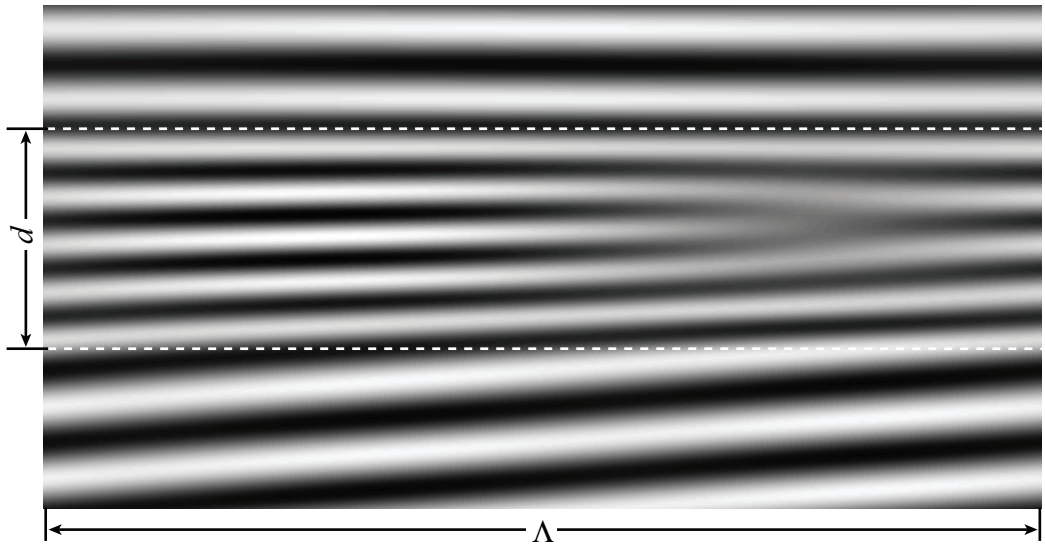


(a) Diffraction efficiencies for various retardation conditions

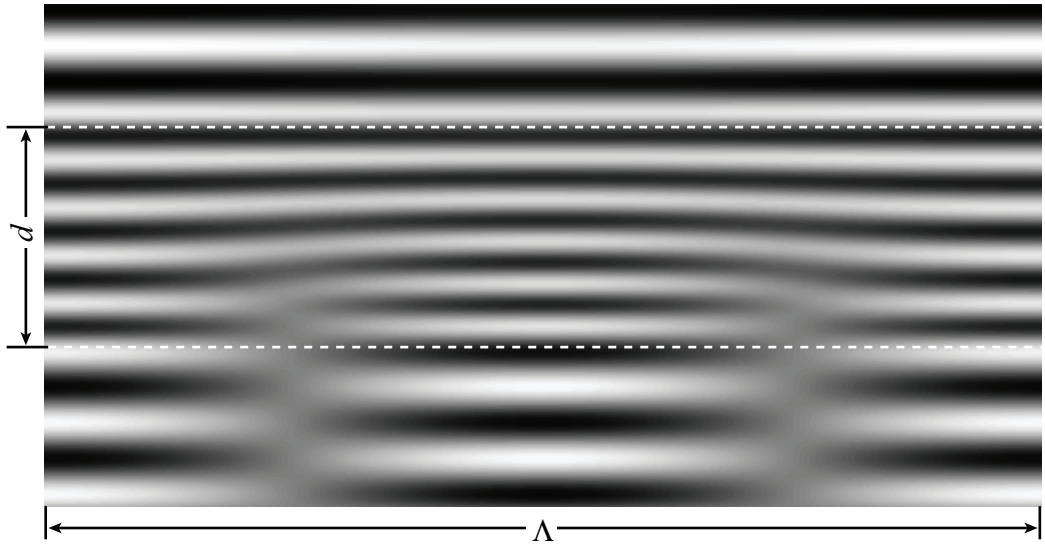


(b) Diffraction efficiencies for various input polarizations

Figure 5.2: Diffraction efficiencies of the linear PG as a function of (a) the normalized retardation $\Delta n_l d/\lambda$ and (b) the ellipticity angle χ of the input polarization. The grating parameters are $\Lambda = 20\lambda_0$, $n_0 = 1.6$, and $\Delta n_l = 0.2$, where λ_0 is the center wavelength.



(a) Near-field image of the electric field for circular input polarization



(b) Near-field image of the electric field for linear input polarization

Figure 5.3: Near-field images of the electric field for (a) circularly polarized input and (b) linearly polarized input. The grating parameters are $\Lambda = 20\lambda$, $n_0 = 1.6$, $\Delta n_l = 0.2$, and $\Delta n_l d/\lambda = \frac{1}{2}$.

We also evaluate the effect of an incident angle on the diffraction properties of the linear PG. Even if it is unclear which angle of incidence starts to break assumptions for the analytical solutions, we can estimate the effective retardation u^* at a certain angle of incidence:

$$u^* = u \times \cos^2 \theta_g \tag{5.3}$$

where $u = \Delta n_l d/\lambda$ and θ_g is the propagation angle in the grating that satisfies $n_0 \sin\theta_g = \sin\theta_{inc}$. Then diffraction efficiencies can be recalculated from Eq. 5.2 using u^* instead of u.

Fig. 5.4(a) illustrates diffraction efficiencies for the first $\lambda/2$ retardation condition. The FDTD results are compared with both analytical and experimental data, which is gratefully provided by Dr. Michael J Escuti. In addition, the normalized Stokes parameter S_3' for the polarization state of the first order is calculated from the FDTD results as a function of incident angles θ_{inc} from 0° to 45°. We note that an oblique illumination affects the polarization state of diffraction orders as well as their efficiencies.

As the incident angle increases, $\Sigma\eta_{\pm 1}$ decreases but the 0^{th} order appears. The polarization of the first order becomes more elliptical. Still, most ($> 99.5\%$) of the energy in diffraction stays in the 0^{th} and 1^{st} orders and the polarization states of the 1^{st} orders are preserved until a relatively high incident angle ($\theta_{inc} \leq 30°$). Good agreement between the FDTD and others is found.

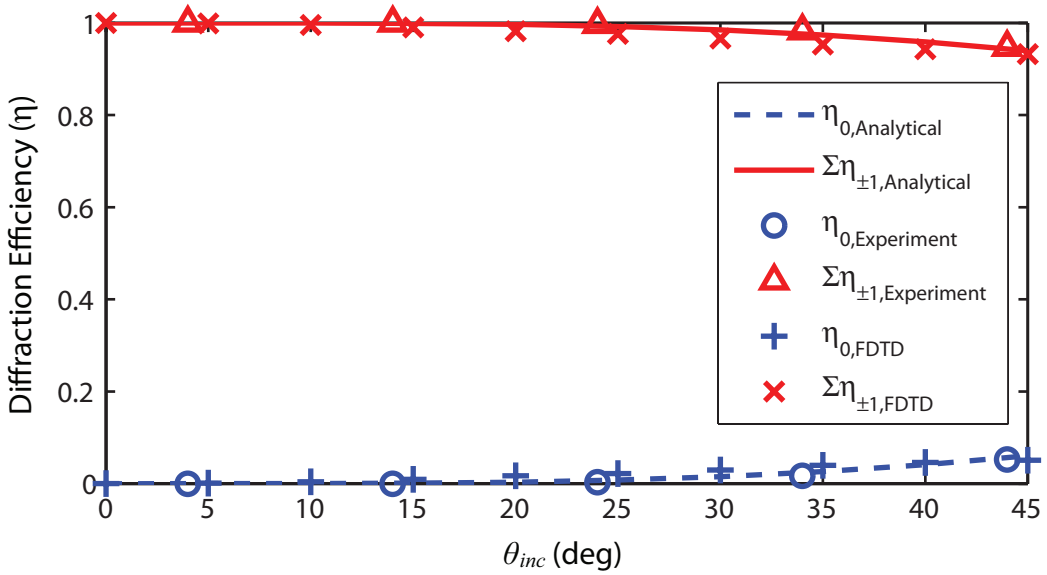
The grating regime is another interesting aspect of linear PGs. Generally, a grating can be classified as the either *thin* or *thick* grating. It is, however, hard to tell if the linear PG falls into one of the grating regimes because of its Bragg properties of diffraction with a thin structure.

Recall that two different parameters can be used to identify the grating regimes [25, 26]:

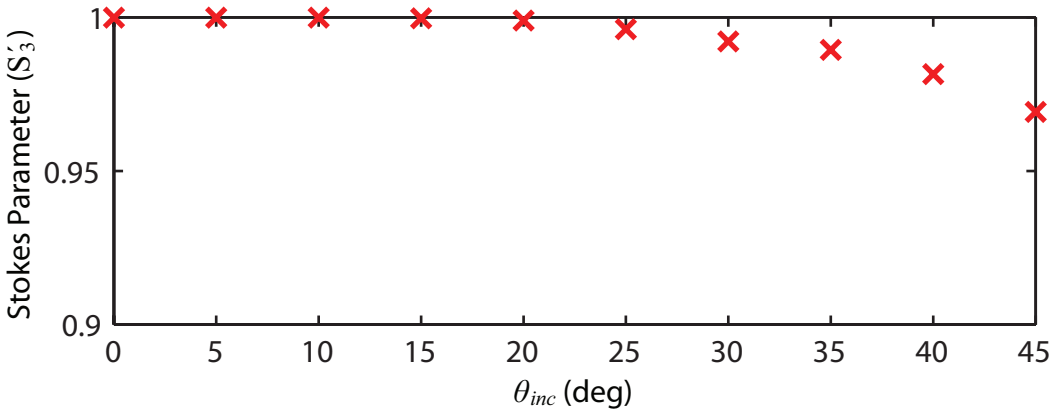
$$\mathrm{Q} = \frac{2\pi\lambda d}{n_0 \Lambda^2} \tag{5.4a}$$

$$\rho = \frac{2\lambda^2}{n_0 \Delta n_l \Lambda^2} \tag{5.4b}$$

where $n_0 \approx \frac{1}{2}(n_\perp + n_\parallel)$. Variable Δn_l is equivalent to the index modulation factor n_1 of the coupled wave theory through $n_1 = \Delta n_l/2$. The main difference between these parameters is that d appears only in Q while ρ has Δn_l.



(a) Diffraction efficiency at various angles of incidence



(b) Nomalized Stokes parameter for the 1^{st} order at various angles of incidence

Figure 5.4: (a) Diffraction efficiencies and (b) the normalized Stokes parameter S_3' of the linear PG at various angle of incidence.

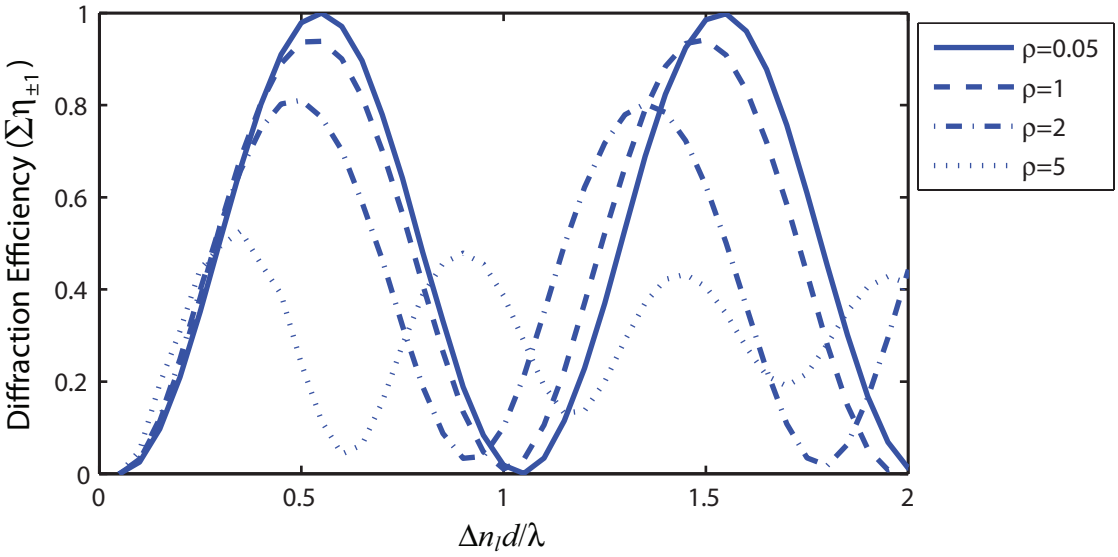


Figure 5.5: The effect of grating parameters ρ and Q on the diffraction properties of the linear PG. Diffraction efficiency (a sum of $\eta_{\pm1}$) is calculated for different values of ρ (0.05, 1, 2, 5) as a function of the normalized retardation $\Delta n_l d/\lambda$; only d is a variable for a given ρ.

We evaluate the impact of Q and ρ parameters on the diffraction of linear PGs. To analyze this, we run a number of monochromatic FDTD simulations with varying d for different values of ρ: 0.05, 0.5, 1, 2, and 5. Analytical solutions in Eq. 5.2 are no longer valid where paraxial approximation fails; i.e. a small grating pitch or a large grating thickness.

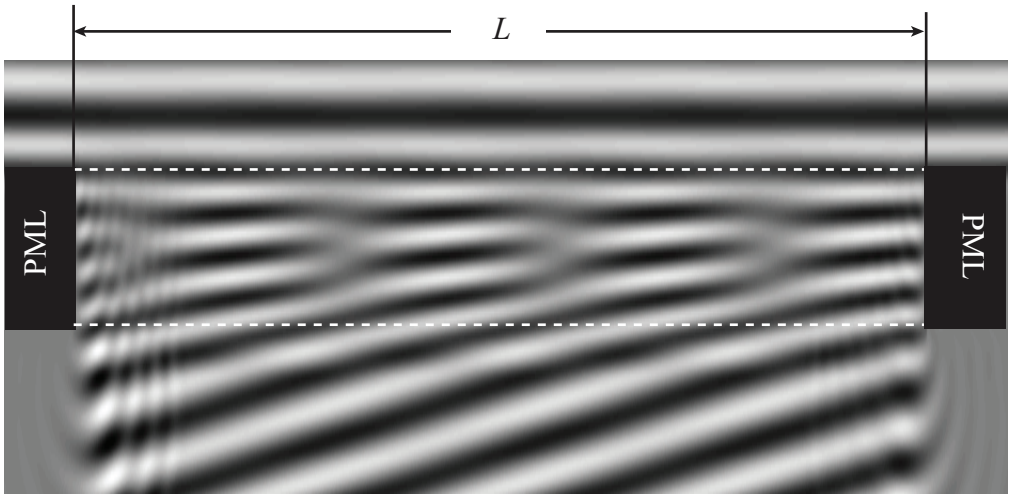
Fig. 5.5 shows the diffraction efficiency (a sum of $\eta_{\pm1}$) with varying d for each ρ value. Note that no higher order appears. We found that ρ parameter dominates to determine the grating regimes of linear PGs in most cases while Q parameter has an impact on diffraction efficiencies for very thick gratings when ρ is relatively large (i.e. $\rho \geq 1$). The traditional threshold values for the grating regimes are still applicable to linear PGs; the thin (Raman-Nath) regime when $\rho \leq 1$; the Bragg grating regime when $\rho \gg 1$. Small variations in the polarization properties of diffracted orders were found when ρ is large; the polarizations of first orders become weakly elliptical.

We also seek to find the minimum size of pixels of linear PGs as a display element. To this end, we study the effect of the finite gratings on the diffraction efficiencies. Fig. 5.6 shows the near-field map of a FDTD simulation and the diffraction efficiency (a sum of $\eta_{\pm1}$). Each pixel is isolated by blocking structures in absorbing media (i.e. PML) and the

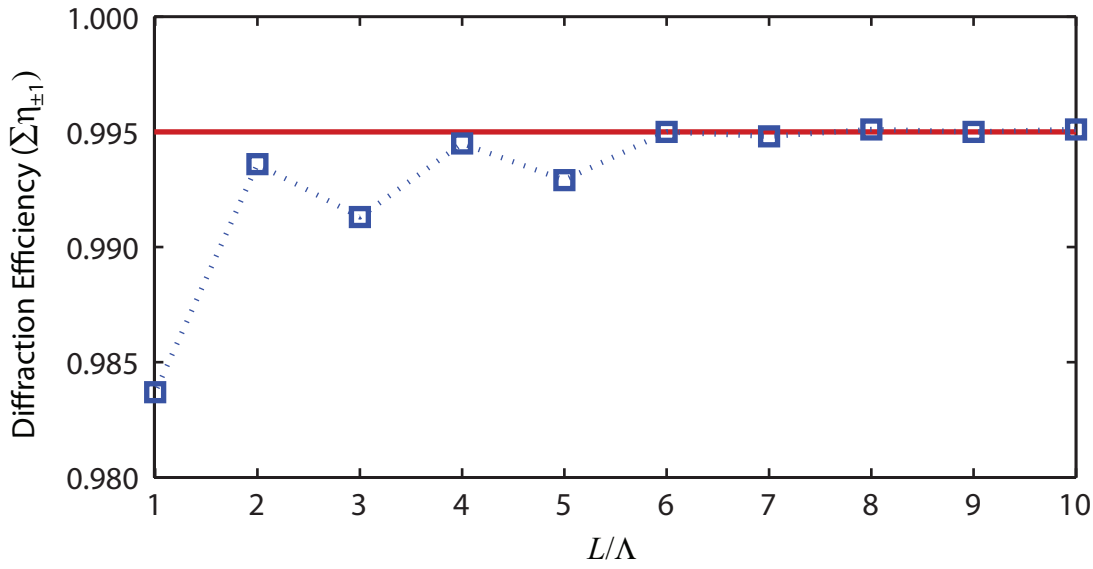
pixel size $L = 4\Lambda$ where $\Lambda = 10\lambda$. We compare the far-field intensities with and without PG structures. The diffraction efficiency asymptotically approaches a nearly ideal value (99.5%) when $L/\Lambda \geq 4$. Note that the maximum diffraction efficiency is $\sim 99.7\%$ for a linear PG having infinite periods when $\Lambda = 10\lambda$. The efficiency weakly bounces corresponding to the ratio L/Λ; it is maximized when L/Λ is an even number whereas it is minimized when L/Λ is an odd number.

Linear PGs can be created by subwavelength features or sub-pixel structures of anisotropic media [7, 8]. In both cases, the discrete anisotropic pattern may affect the diffraction properties of the original linear PG with a continuous profile. Tervo and coworkers reported an analytical study on the effect of lateral pixelation in anisotropy pattern of linear PGs [61].

We briefly repeat the same work to verify the pixelation effect of anisotropy pattern by the FDTD simulations. It is also useful to validate our modified FDTD algorithm by comparing it with the previously reported data. Fig. 5.7(a) and (b) show a sum of the first order diffraction efficiencies for circular and linear input polarizations, respectively. The diffraction efficiency is calculated for the $\lambda/2$ retardation condition as a function of the number of sub-pixels (P) in one grating period (Λ). We note that the sum of efficiencies in the first orders depends on only the retardation condition, not the polarization of the incident beam. The FDTD results are shown to match the analytical results in [61].

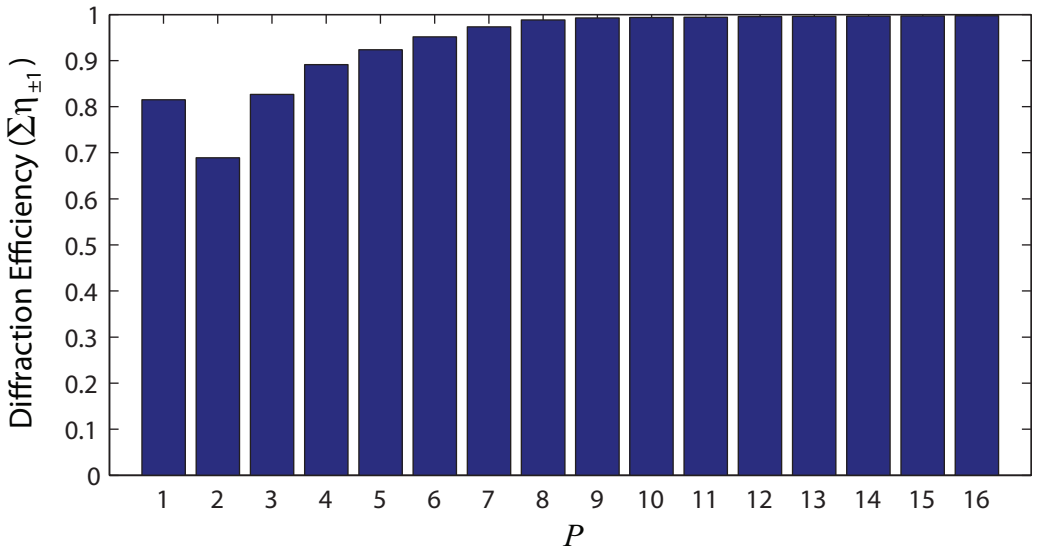


(a) Near-field map of the electric field

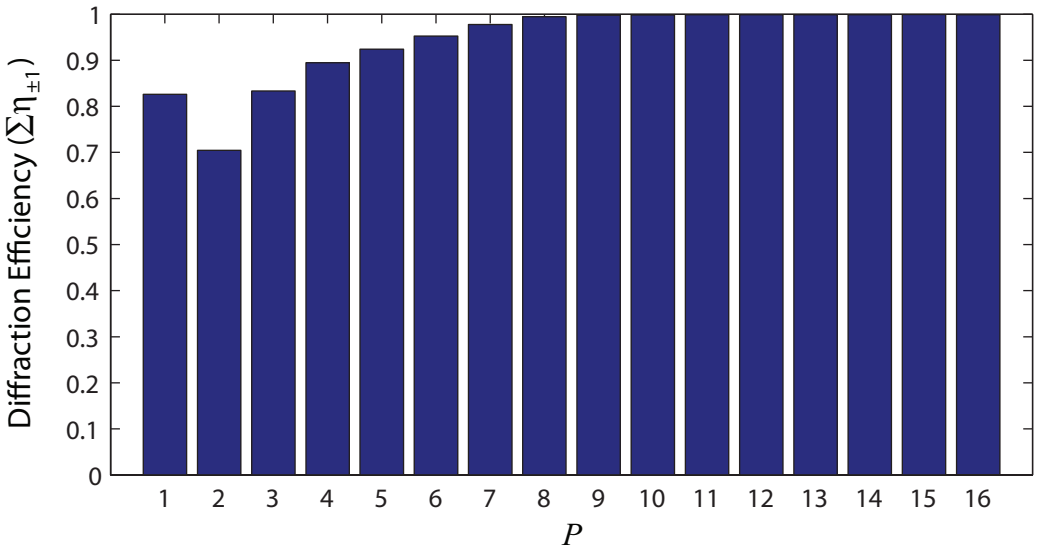


(b) Diffraction efficiency for various Pixel Sizes

Figure 5.6: Linear PG within a single small pixel: (a) near-field map of the electric field and (b) far-field diffraction efficiency (a sum of $\eta_{\pm 1}$) for various pixel size L/Λ. The red line points 99.5% of efficiency. Each pixel is isolated by absorbing media (PML) and L is the size of a pixel. The grating parameters are $\Lambda = 10\lambda_0$, $n_0 = 1.6$, and $\Delta n_l = 0.2$, where λ_0 is the center wavelength.



(a) Diffraction efficiency of the discrete linear PG for circular input polarization



(b) Diffraction efficiency of the discrete linear PG for linear input polarization

Figure 5.7: The effect of lateral pixelation in the anisotropy pattern of linear PGs. Diffraction efficiency (a sum of $\eta_{\pm1}$) is calculated for the $\lambda/2$ retardation condition as a function of the number of sub-pixels P in one grating period.

5.1.2 Elliptical Polarization Gratings

The second type of PGs, namely *elliptical* PGs, have a periodic modulation in both orientation and shape of anisotropy as shown in Fig. 5.1(b). Even with a same holographic field created by the interfering beams, induced spatially varying anisotropy patterns may differ according to birefringence of recording media. One can divide elliptical PGs into two cases depending on the presence of circular birefringence because the diffraction characteristics are completely different based on the presence or absence of circular birefringence: elliptical PGs only with linear birefringence (case 1) and with both linear and circular birefringence (case 2). The former performs very similar diffraction with conventional thin phase gratings whereas the latter yields complementary properties to linear PGs.

Case 1: Elliptical polarization hologram with only linear birefringence

Fig. 5.8 shows the diffraction efficiencies of the elliptical PG in the first case at normal incidence as a function of u. This type of PG produces a large number of diffraction orders as normal phase gratings do. In addition, the diffraction efficiencies do not respond to the input polarization. However, these PGs still have polarization selectivity;

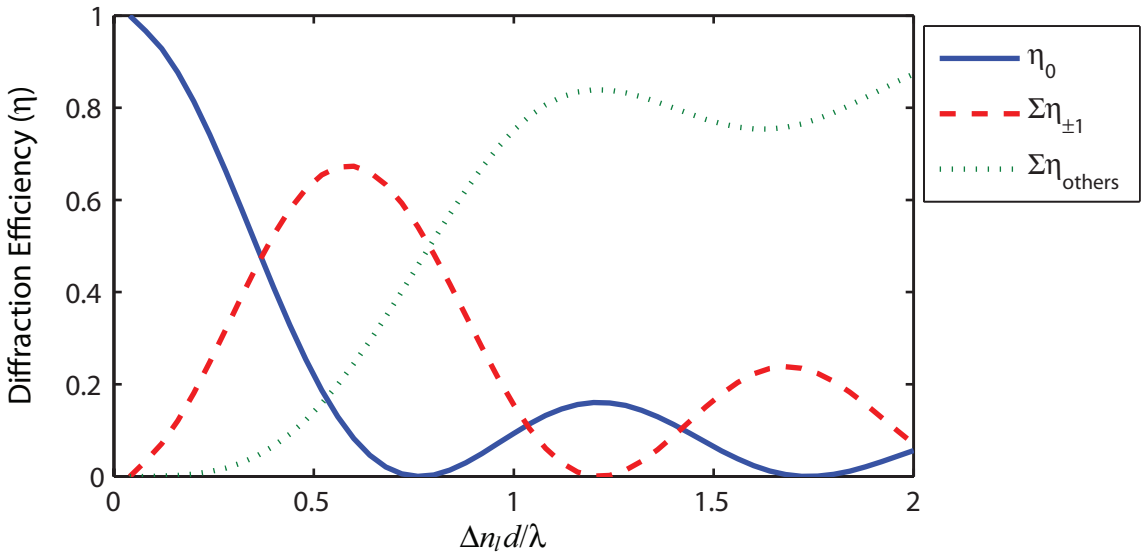


Figure 5.8: Diffraction efficiencies of the elliptical PG as a function of the normalized retardation $\Delta n_l d/\lambda$. The grating parameters are $\Lambda = 20\lambda_0$, $n_0 = 1.6$, and $\Delta n_l = 0.2$, where λ_0 is the center wavelength.

the odd orders have linear polarization rotated by $\pi/2$ for linear input polarization. The maximum diffraction efficiency ($\Sigma\eta_{\pm1}$) from FDTD simulation is 37.4%, which agrees with the previous calculation using the Jones analysis [15].

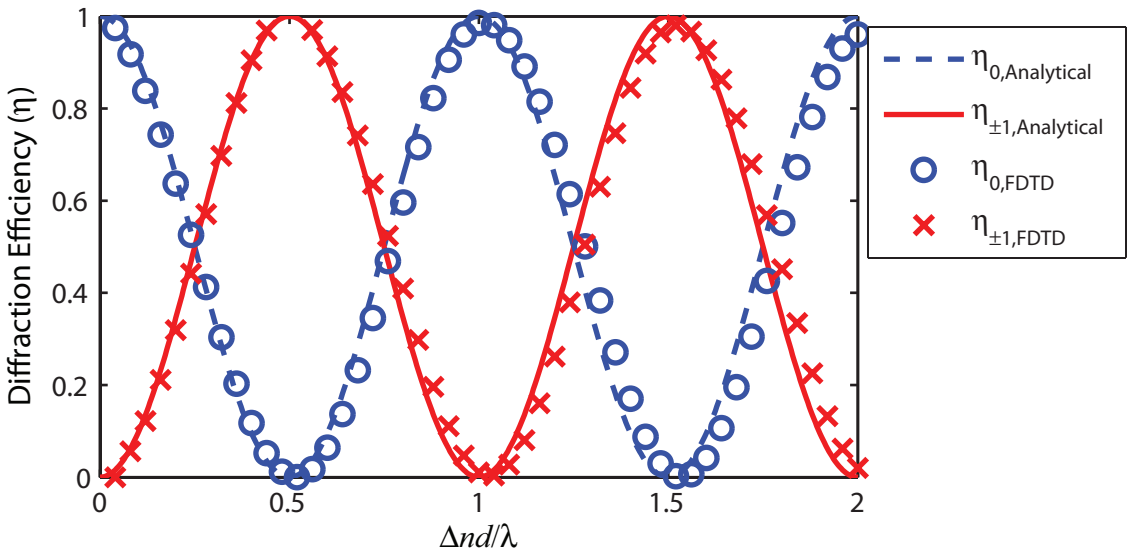
Case 2: Elliptical polarization hologram with linear and circular birefringence

The diffraction efficiencies of the second case of the elliptical PG are illustrated in Fig. 5.9(a). The analytical solutions of diffraction efficiencies are available [4]:

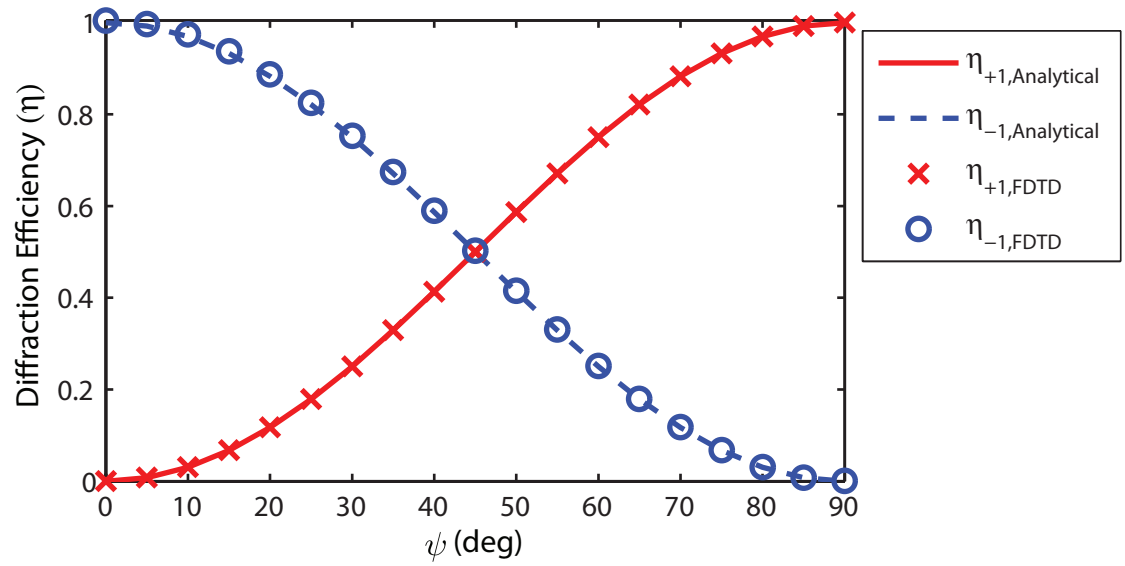
$$\eta_0 = \cos^2(\pi\Delta nd/\lambda) \tag{5.5a}$$

$$\eta_{\pm1} = \frac{1 \mp S_1'}{2}\sin^2(\pi\Delta nd/\lambda) \tag{5.5b}$$

where S_1' is a normalized Stokes parameter which describes horizontal and vertical linear polarizations and both linear and circular birefringence have the same value of $\Delta n = \Delta n_l = \Delta n_c$. Interestingly, its diffraction characteristics resemble those of a linear PG. However, the optical properties of the two PGs are completely different. The first order diffraction of elliptical PGs responds to the orientation of the polarization ellipse while linear PGs respond to a variation in the ellipticity. Fig. 5.9(b) shows the polarization sensitivity of the first diffraction orders of elliptical PGs with circular birefringence. Moreover, the first orders of elliptical PGs have horizontal and vertical linear polarization. Again, this is explained by the fact that the induced polarization state by the anisotropy pattern in elliptical pg as shown in Fig. 5.1(b) can be exactly decomposed into these orthogonal linear polarizations. We note that elliptical PGs with the same linear and circular birefringence have a complementary function to linear PGs.



(a) Diffraction efficiencies for various retardation conditions



(b) Diffraction efficiencies for various input polarizations

Figure 5.9: Diffraction efficiencies of elliptical PGs as a function of (a) the normalized retardation $\Delta nd/\lambda$ and (b) the azimuth angle ψ of the input polarization. The grating parameters are $\Lambda = 20\lambda_0$, $n_0 = 1.6$, and $\Delta n_l = \Delta n_c = 0.2$, where λ_0 is the center wavelength.

The functions of PGs can be described using the Poincré sphere [21], which gives a simple picture for polarizing elements. The polarization of the first orders is converted into the characteristic states for each type of PGs while the polarization of the even orders retain the input polarization as shown in Fig. 5.10.

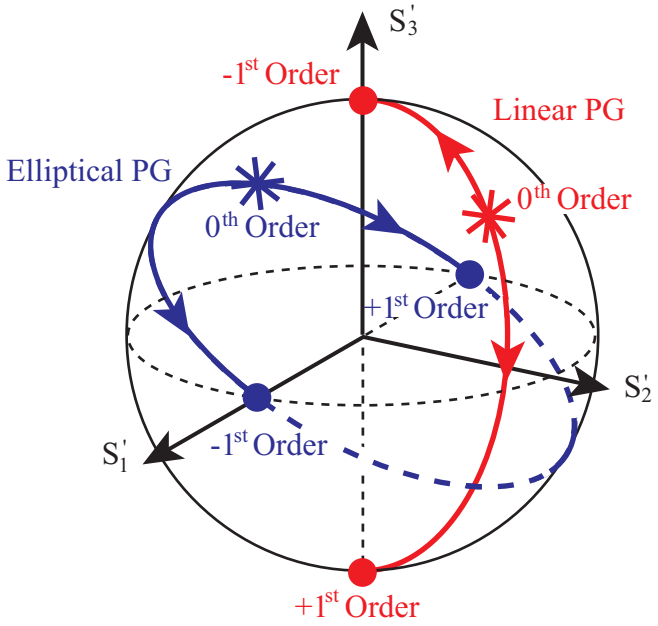


Figure 5.10: Schematic view of the function of PGs on Poincré sphere; red color corresponds to linear PGs and blue color to elliptical PGs with both linear and circular birefringence. Arrows depict the conversion of polarization to the characteristic states: left- and right-hand circular polarizations for linear PGs; horizontal and vertical linear polarizations for elliptical PGs.

5.2 Design of Broadband Polarization Gratings

Extensive numerical analysis in the previous section shows the unique diffraction properties of PGs, which can be very useful for optical systems using polarization of light. A variety of applications of linear PGs were proposed because of their relatively easy fabrication using present materials and their useful polarization diffraction properties. Some examples of these applications include highly efficient linear and circular polarizers, polarizing beam splitters, polarization sensing, polarization independent light modulators, polarizing remote sensing, optical filters, and optical data storage [5–7, 9, 10, 62–64]. Still, fabrication of high quality PGs has limited their real applications. Recently, promising technologies for creating highly efficient and defect-free PGs using polarizing holography and photo-alignment techniques with liquid crystals was reported [57, 58, 65].

The most important advantage of PGs is 100% efficiency in limited diffraction orders. However, an improvement of the spectrum of PG diffraction is desirable for some applications such as spectro-photometry and displays. For these applications, a flat spectrum in the operation range may be required while the PG spectrum appears parabolic.

In this section, we report novel structures of broadband PGs with the same properties of diffracted beams as normal PGs. First, we briefly discuss experiment procedures of polarizing holograms of PGs using reactive mesogens and photo-alignment techniques. Then, we analyze diffraction properties of broadband PG structures. The optimal grating parameters for each design of broadband PGs are tested by the FDTD simulations. Preliminary experiments are also presented.

5.2.1 Polarizing Holography as a means of PG Creation

The first report of PGs was the study of polarization holograms by two orthogonal polarization recording beams [2]. Nikolova et al. reported a more extensive study of diffraction properties of PG holograms. The polarizing interference pattern by two circularly polarized lights is exactly the same as the spatially variant birefringence of linear PGs as shown in Fig. 5.1. The holography setup for PGs is pictured in Fig. 5.11.

In principle, polarizing holograms using orthogonal beams can have an ideal continuous variation in birefringence. However, the quality of PGs is highly dependent on the choice of materials as recording media. Direct recording of volume holograms with photo-

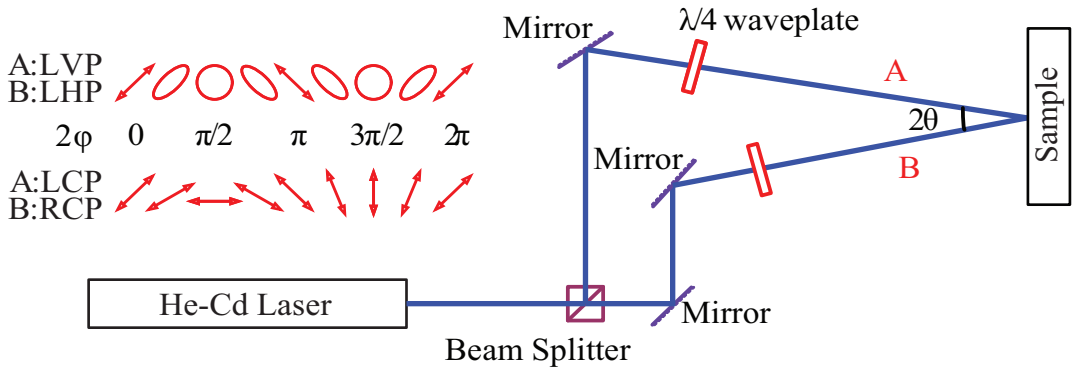
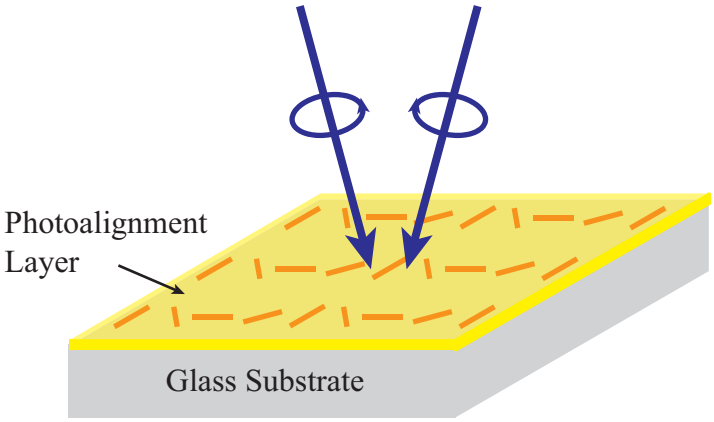


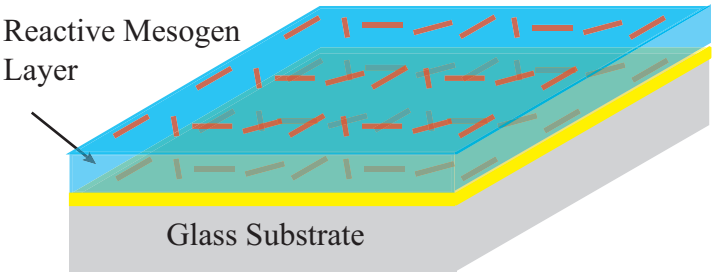
Figure 5.11: Optical system for recording polarizing holograms using two orthogonal polarizations, left- (LCP) and right-hand (RCP) circular or vertical (LVP) and horizontal (LHP) linear polarization. φ is the phase difference between recording beams and arrows depict induced anisotropy by polarization interference of two recording beams.

sensitive materials such as azobenzene polyesters is limited by their low quality of gratings. An effective alternative way of PG creation is the photoalignment technique with liquid crystals.

Photoalignment is a technology for aligning liquid crystal textures without mechanical treatment like micro-rubbing on the surface. The holography procedures for photoalignment material are same as the case of volume holograms. Once recording PG holograms in photoalignment layer, liquid crystal molecules will be aligned following their preferred directions on the surface of the layer. Fig. 5.12 illustrates recording and creating PGs using reactive mesogens (polymerizable liquid crystals). The key of the fabrication of high quality PGs is a proper combination of photoalignment materials and liquid crystal materials. Escuti and his coworkers reported their experimental study of electrically switchable PGs with nematic LC materials for projection display applications using photoalignment technique [58].



(a) Recording of polarization grating in photo-alignment materials



(b) Spinning and polymerization of reactive mesogen films

Figure 5.12: Fabrication procedures of holographic polarization gratings based on a combination of liquid crystal materials and the photo-alignment technique.

5.2.2 Combination of Double-Layered PGs with Mirror Images

A combination of two gratings can improve the bandwidth of PG diffraction when they are mirror images of each other as shown in Fig. 5.13. The uniaxial birefringence in the grating plane for PG1 and PG2 can be described as follows:

$$\text{PG1: } \mathbf{n}(x) = [\sin(\pi x/\Lambda)\ \cos(\pi x/\Lambda)\ 0] \tag{5.6a}$$

$$\text{PG2: } \mathbf{n}(x) = [-\sin(\pi x/\Lambda)\ \cos(\pi x/\Lambda)\ 0] \tag{5.6b}$$

The diffraction efficiencies of this double PG can be derived directly from the analytical solutions in Eq. 5.2:

$$\eta_0 = \cos^4(\pi u/2) \tag{5.7a}$$

$$\eta_{\pm 1} = 2\sin^2(\pi u/2)\cos^2(\pi u/2) \tag{5.7b}$$

$$\eta_{\pm 2} = \frac{1}{4}\sin^4(\pi u/2) \tag{5.7c}$$

where $u = \Delta n_l d/\lambda$. The order of the cosine function in η_0 now becomes 4, exactly a double of that for single PGs. In addition, we note that the second orders appear in diffraction.

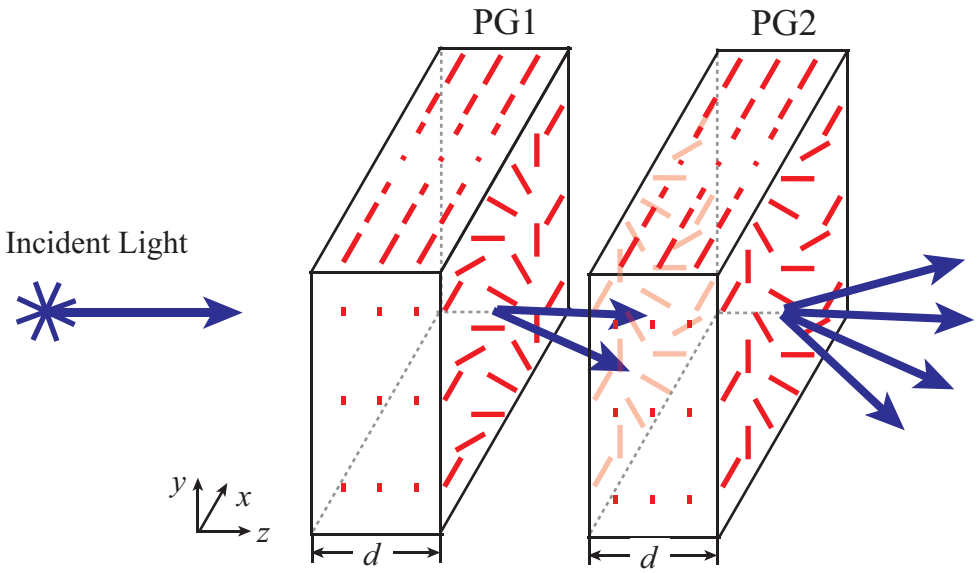


Figure 5.13: Schematic view of the double-layered PG structure for broadband operation. Bars depict uniaxial birefringence in plane.

Fig. 5.14 shows the diffraction efficiencies of a double-layered PG. A strong improvement in the bandwidth for the maximum diffraction efficiency ($\geq$ 99.5%) can be achieved. We compare the bandwidth of the new structure with the original PG in terms of $\Delta\lambda(\% - \lambda_0)$, where λ_0 is the center wavelength for the the first $\lambda/2$ retardation condition. $\Delta\lambda_1 \sim 17.62(\% - \lambda_0)$ for a single PG (PG1 only). For the double-layered PG, it is found to be $\Delta\lambda_2 \sim 35.37\,(\% - \lambda_0)$, approximately double the single PG spectrum.

The double-layered structure can be easily implemented using two identical PGs simply by flipping one of PGs and making them face each other. PGs were fabricated using photo-alignment material ROP-103/2CP (Rolic) and reactive mesogen RMS03-001 (Merck) for verification of the broadband operation of double-layered PGs. Glass substrates were used, and the PG hologram was formed using HeCd laser ($325nm$) with a dose of $\sim 0.3J/cm^2$. The grating period of both PGs was measured $\sim 10\mu m$. We measured the 0^{th} order transmission in the wavelength range of $300nm$ to $800nm$ in the cases of both a single PG and the double-layered structure. Fig. 5.15 shows measured spectrums in both cases. A significant improvement in the diffraction spectrum appears clear. Note that absorption by glass substrates reduces transmittance in UV range near $300nm$. Also reflections at the interfaces with air may take place because of index mismatching.

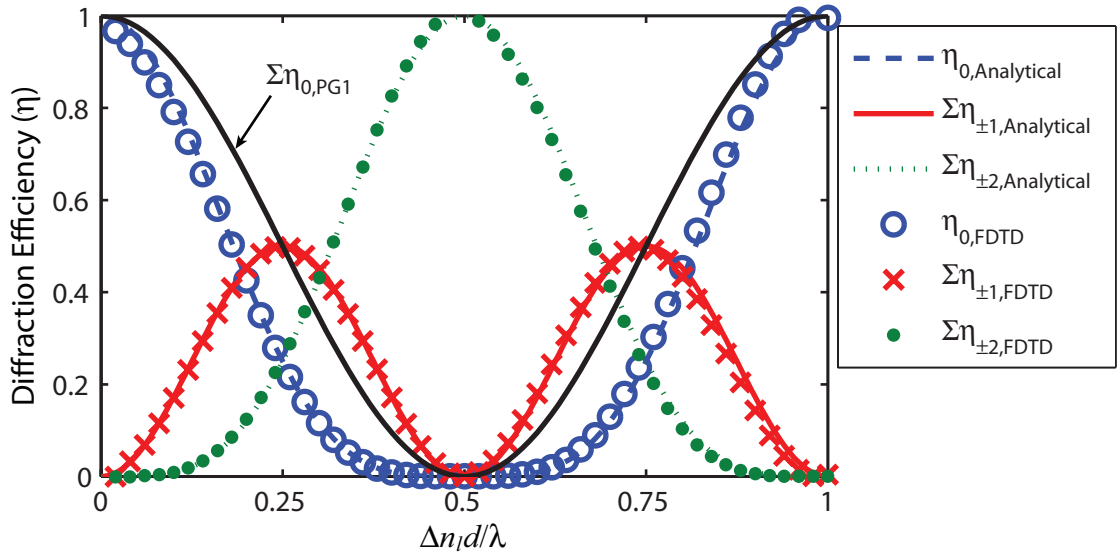


Figure 5.14: Diffraction efficiencies of double-layered PGs as a function of the normalized retardation $\Delta n_l d/\lambda$. Diffraction efficiency of linear PGs is marked for comparison. The grating parameters are $\Lambda = 20\lambda_0$, $n_0 = 1.6$, and $\Delta n_l = 0.2$, where λ_0 is the center wavelength.

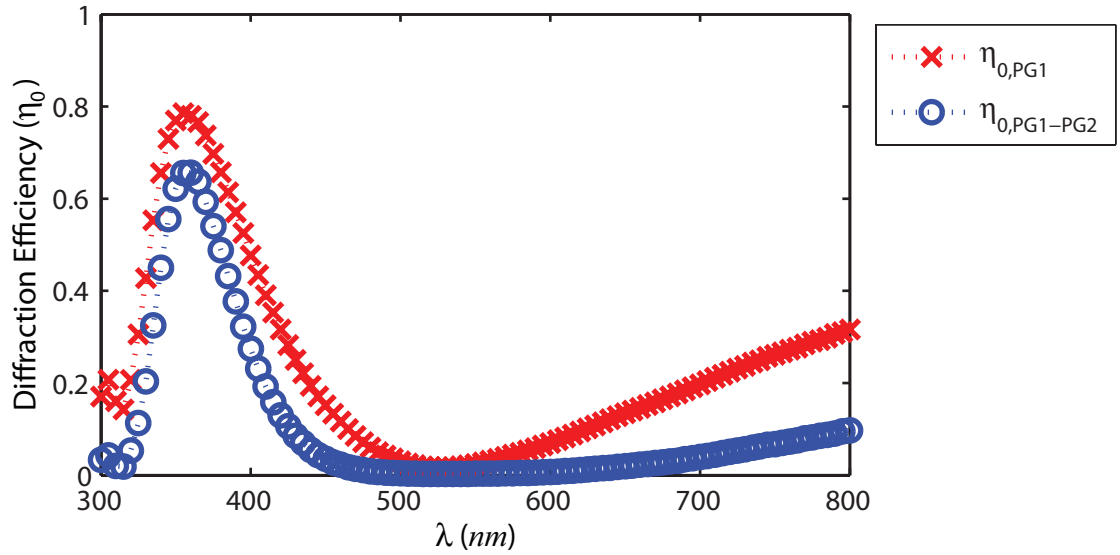


Figure 5.15: Transmittance measured by spectro-photometer of the 0^{th} order for a single PG (PG1) and the double-layered PG (PG1-PG2).

5.2.3 Achromatic Polarization Gratings

We show that a simple combination of two gratings can be used as a broadband PG in the previous section. One of the advantages of the double-layered PG is its simple structure with two identical gratings. However, the improvement of bandwidth is only doubled and two more diffraction orders ($\eta_{\pm 2}$) appear. Still, it should be possible to construct a nearly achromatic polarization grating with the same diffraction properties of linear PGs.

Achromatic wave-plates can be designed using three plates of the same material [66]. The basic structure of an achromatic wave-plate is a combination of three birefringent plates, two identical wave-plates as the first and last and the principal plane of the middle plate making an angle with that of other plates.

We apply the same structure with three identical PGs with an angular shift (θ_{shift}) in the birefringence of the middle PG (PG2) as shown in Fig. 5.16. The angular shift may be achieved by micro-alignment of three independent PGs. However, a more attractive method is introducing thin layers of chiral liquid crystals between PGs. θ_{shift} can be controlled by the pitch of chiral LC materials and its thickness. If the helical pitch of liquid crystal is small enough (i.e. $\sim 100nm$), it is possible to get arbitrary angular shift with very thin chiral LC layers so that the effect of chiral layers can be ignored. The most important advantage of the second method over micro-alignment is its compact structure; it requires three layers of PGs integrated on one substrate instead of three completely independent PGs.

To find the optimal condition for θ_{shift}, we analyze the diffraction efficiency (a sum of $\eta_{\pm 1}$) for different values of θ_{shift}. Diffraction efficiencies, calculated from FDTD simulations, are summarized in Fig. 5.17. The maximum bandwidth $\Delta\lambda_{max} = 60.22(\%-\lambda_0)$ was found when $\theta_{shift} \sim 57^\circ$. The bandwidth of diffraction is further improved over that of the double-layered PG. Moreover, this achromatic PG has the same diffraction properties as normal linear PGs; it has only three diffraction orders, the 0^{th} and $\pm 1^{st}$ orders.

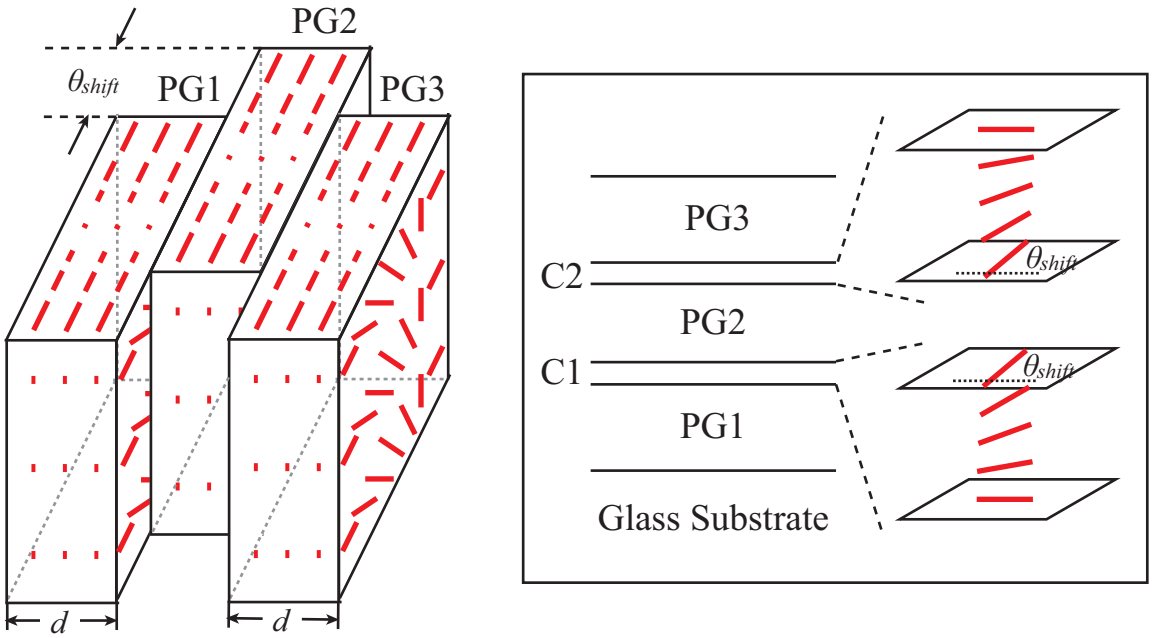


Figure 5.16: Schematic view of the achromatic PG structure using three polarization gratings. θ_{shift} is the phase difference of the middle PG (PG2) with respect to the other PGs. Chiral liquid crystal layers (C1 and C2) with the opposite sense of twist (right- and left-hand) can be used to integrate three grating layers instead using three independent gratings. The structure using chiral LC layers is described inside of the box. Bars depict uniaxial birefringence in the plane.

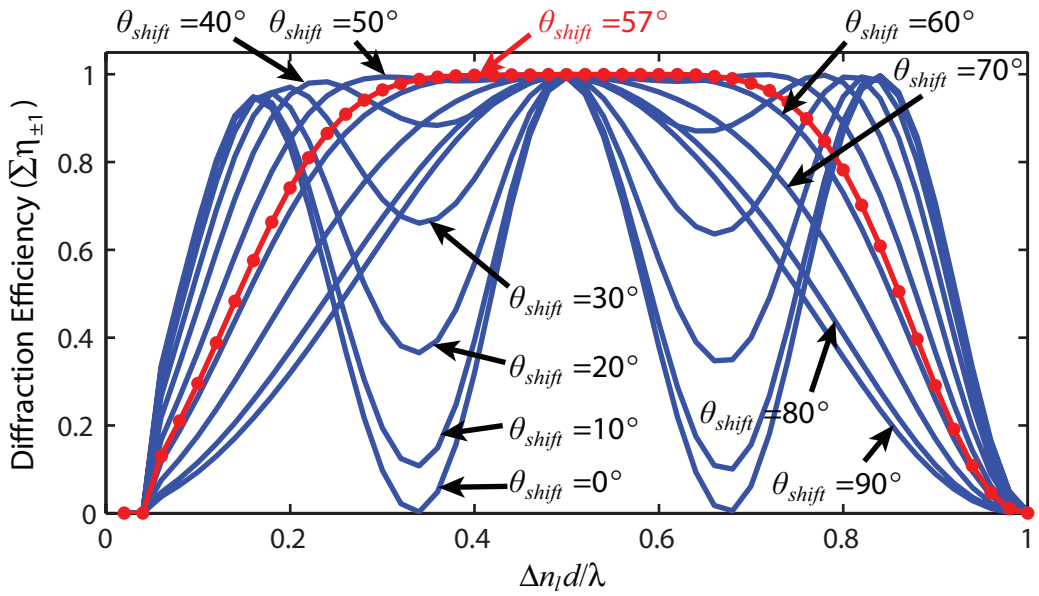


Figure 5.17: Diffraction efficiency (a sum of $\eta_{\pm 1}$) of the achromatic PG using three grating layers as a function of the normalized retardation $\Delta n_l d/\lambda$ for different angular shifts θ_{shift} of the middle layer. The maximum bandwidth $\Delta\lambda_{max} = 60.22(\% - \lambda_0)$ for the first order diffraction can be achieved when $\theta_{twist} = 57°$. The grating parameters are $\Lambda = 20\lambda_0$, $n_0 = 1.6$, and $\Delta n_l = 0.2$, where λ_0 is the center wavelength.

5.2.4 Twisted Polarization Gratings

Optical systems using the achromatic PG can be operated in a very wide range of spectrum. However, one difficulty in fabrication is control of the shift angle between the middle layer and others. Even a small variation of the thickness of chiral LC layers can affect the diffraction properties significantly because we want to use chiral LC materials with short cholesteric pitches.

An alternative solution is using chiral liquid crystal materials with relatively large cholesteric pitches, namely the *twisted PG*. A similar phase difference between PG layers can be formed in two twisted PG layers with opposite sense of twist as shown in Fig. 5.18. Fabrication steps can be dramatically simplified. Large pitch chiral LC materials can be easily synthesized as a mixture of nematic reactive mesogens with chiral dopants. The helical pitch can be designed by varying the amount of chiral dopants in reactive mesogens.

Similarly, we tested the performance of the double-layered twisted PG with different angles of θ_{twist}. Fig. 5.19 illustrates FDTD results for the diffraction efficiency. The maximum bandwidth $\Delta\lambda_{max}$ was found to be $46.65(\% - \lambda_0)$ when $\theta_{twist} \sim 70°$. This band-

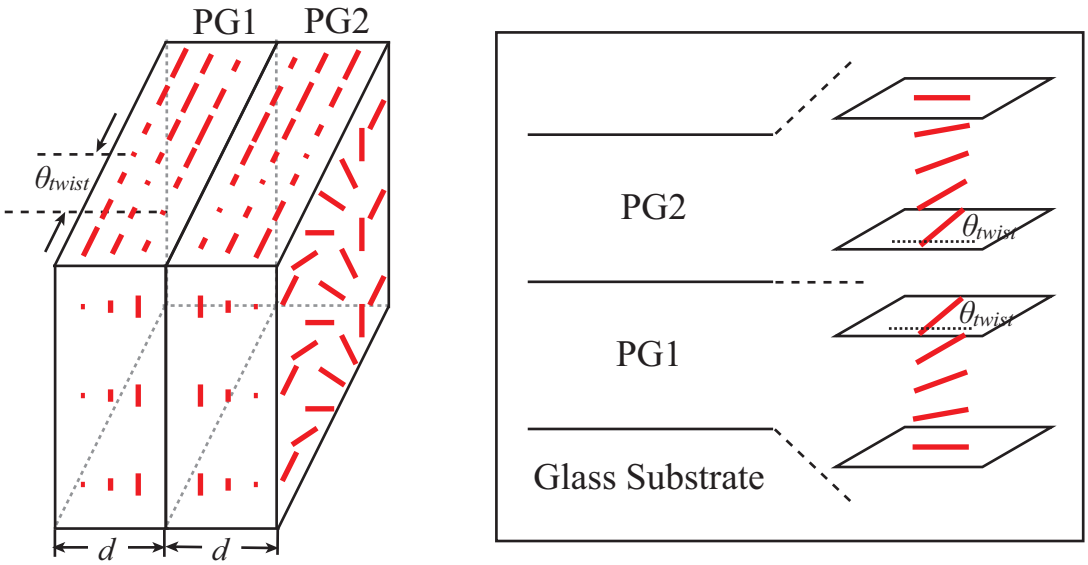


Figure 5.18: Schematic view of the double-layered twisted PG structure for broadband operation. θ_{twist} is the total twist angle of each layer of twisted PGs, which have opposite sense of twist. Bars depict uniaxial birefringence in the plane.

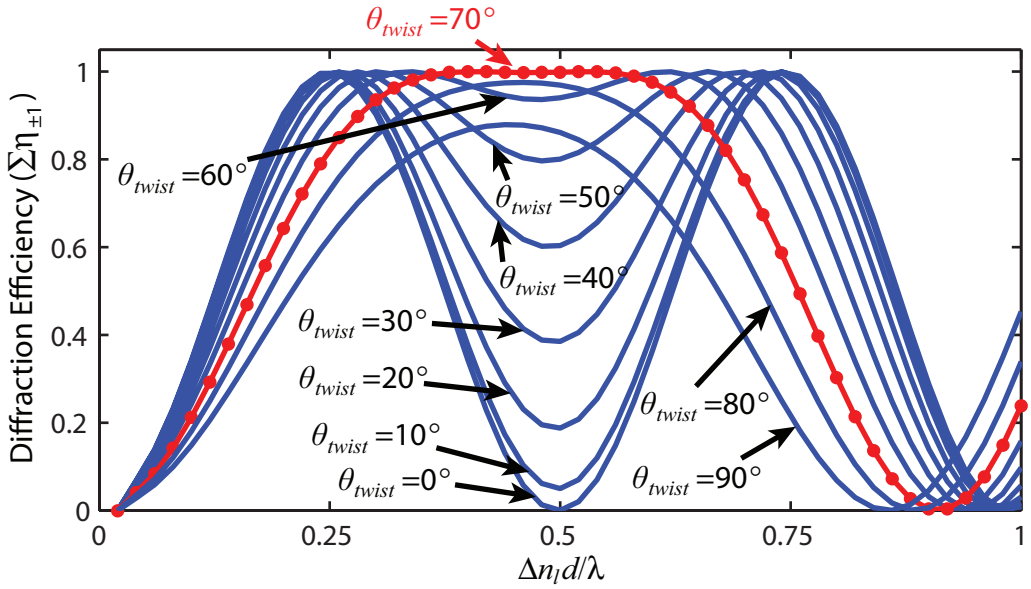


Figure 5.19: Diffraction efficiency (a sum of $\eta_{\pm 1}$) of the double-twisted PG as a function of the normalized retardation $\Delta n_l d/\lambda$ for different twist angles θ_{twist} from 0 to 90°. The maximum bandwidth $\Delta\lambda_{max} = 46.65(\% - \lambda_0)$ for the first order diffraction can be achieved when $\theta_{twist} = 70°$. The grating parameters are $\Lambda = 20\lambda_0$, $n_0 = 1.6$, and $\Delta n_l = 0.2$, where λ_0 is the center wavelength.

width is smaller than that of the achromatic PG. Still, the double-layered twisted PG is attractive because of its simple structure.

The key parameter of the double-layered twisted PG is θ_{twist}. The diffraction properties will be very sensitive to even a small variation of the twist angle. For this reason, a precise control of the total twist angle as well as the thickness of the layer is essential. The twist angle θ_{twist} can be written as

$$\theta_{twist} = 2\pi d/(C \times P) \tag{5.8}$$

where d is the thickness of the chiral layer, P is the helical pitch length and C is the chiral concentration. For a given chiral dopant, θ_{twist} can be controlled by varying the chiral concentration C.

Still, maintaining control of the twist angle is practically difficult due to the following two reasons. First, there is no direct measurement method of HTP. Second, the helical pitch P can vary with host material properties. Moreover, the final liquid crystal textures may affect θ_{twist} or chiral dopants may change the effective retardation of LC layer.

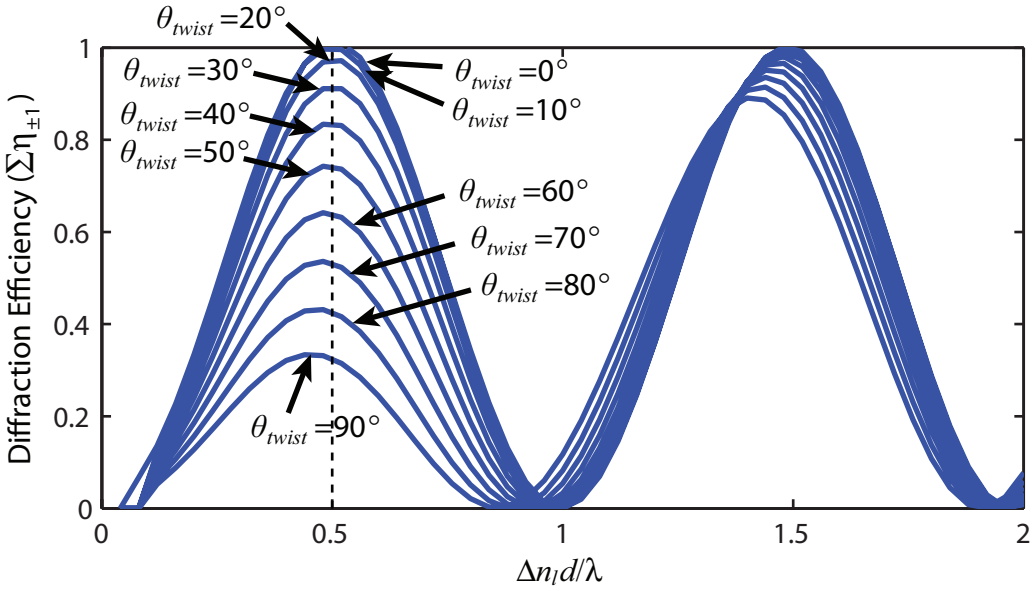
An effective alternative method is to estimate θ_{twist} of the twisted PG from its diffraction properties. To this end, we evaluate the effect of θ_{twist} on the twisted PG diffraction. Fig. 5.20 shows the diffraction efficiency (a sum of $\eta_{\pm 1}$) calculated from FDTD simulations for various total twist angle θ_{twist}. We note that the diffraction efficiency at the first $\lambda/2$ retardation condition is limited by θ_{twist}. Still, only two first orders of diffraction exist for all twist angles. In addition, the diffraction spectrum is shifted to longer wavelength as θ_{twist} increases. The degradation in diffraction efficiency can be explained by the fact that a relatively fast twist in the wavelength can change the polarization state of light propagating in the medium as shown in Fig. 4.10. The effect of twist angle on the diffraction efficiency is reduced for shorter wavelengths where stronger waveguiding can occur.

We prepared the twisted PG samples using the left-handed chiral dopant ZLI-811 mixed in the nematic reactive mesogen RMS03-001 with $\Delta n_l \sim 0.145$ (both are Merck mixtures). The dopant concentration C of ZLI-811 is $0.27wt\%$. The liquid crystal mixture is diluted with the solvent PGMEA by $40wt\%$ to obtain thin layer by spin coating. The PG hologram was recorded in the photoalignment layer (ROP-103/2CP, Rolic) using HeCd laser ($325nm$) with a dose of $\sim 0.5J/cm^2$. After spinning the reactive mesogen mixture at $2krpm$, each layer was polymerized to fix its texture. The twisted PG sample with six layers was implemented.

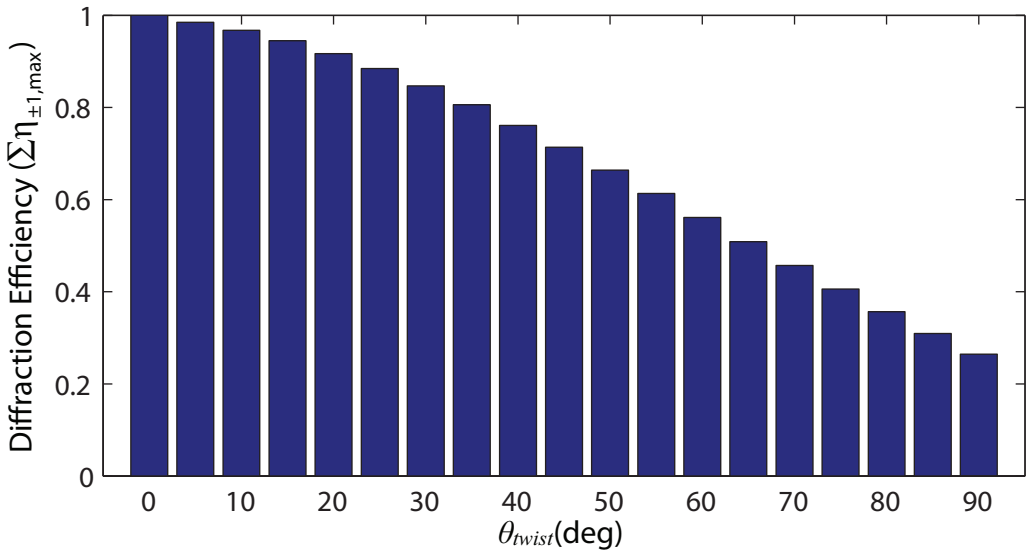
Fig. 5.21 shows the measured spectrum of the 0^{th} order transmittance at each stage of layers. θ_{twist} was estimated by comparing the minimum diffraction efficiency with previous FDTD simulation results in Fig. 5.20. We found that the twist angle θ_{twist} increases linearly with the number of layers (N). Note that the small θ_{twist} of the first layer is incorrect because of the high absorption of glass substrate near $300nm$.

The helical pitch length P of ZLI-811 in RMS03-001 can be calculated from Eq. 5.8. The thickness of the twisted PG sample is estimated for the first $\lambda/2$ retardation condition. For example, the 0^{th} order transmittance with three layers has its minima at $\lambda_0 \sim 460nm$ and the thickness is given by $d = \frac{1}{2}\lambda_0/\Delta n_l \simeq 1.59\mu m$. Since $\theta_{twist} = 40.5°$, $P = 2\pi/(C \times \theta_{twist}) \simeq 381nm$. This pitch length is comparable with a recent study of the properties of ZLI-811 in another nematic liquid crystal mixture [67].

These results show that the angle of twist of the PG can be easily controlled by the $wt\%$ of chiral dopant and the thickness. However, another chiral dopant (right-handed) must be tested to implement the broadband structure. We leave further experimental study for our future work.

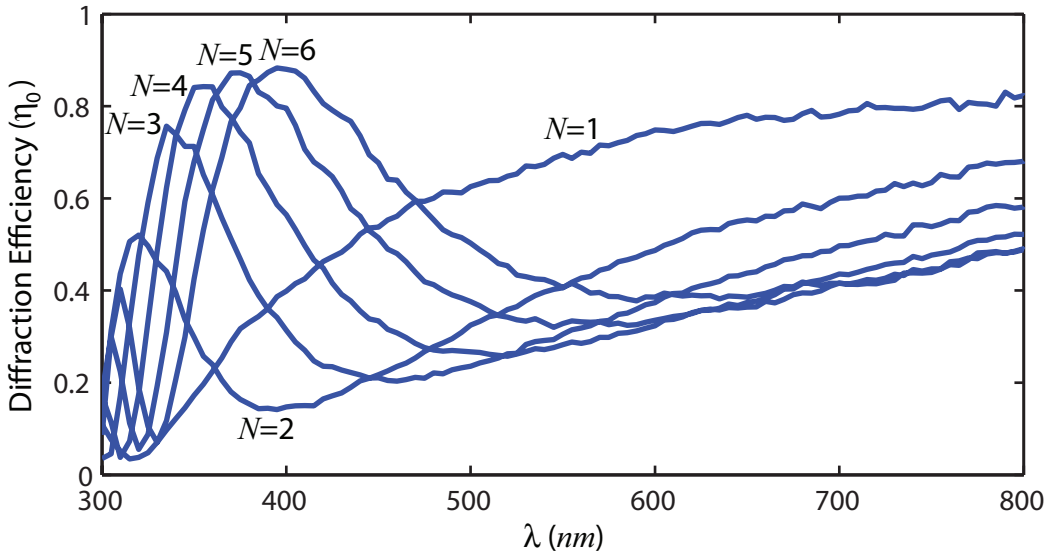


(a) Diffraction efficiency ($\Sigma\eta_{\pm1}$) of the twisted PG for different twist angles

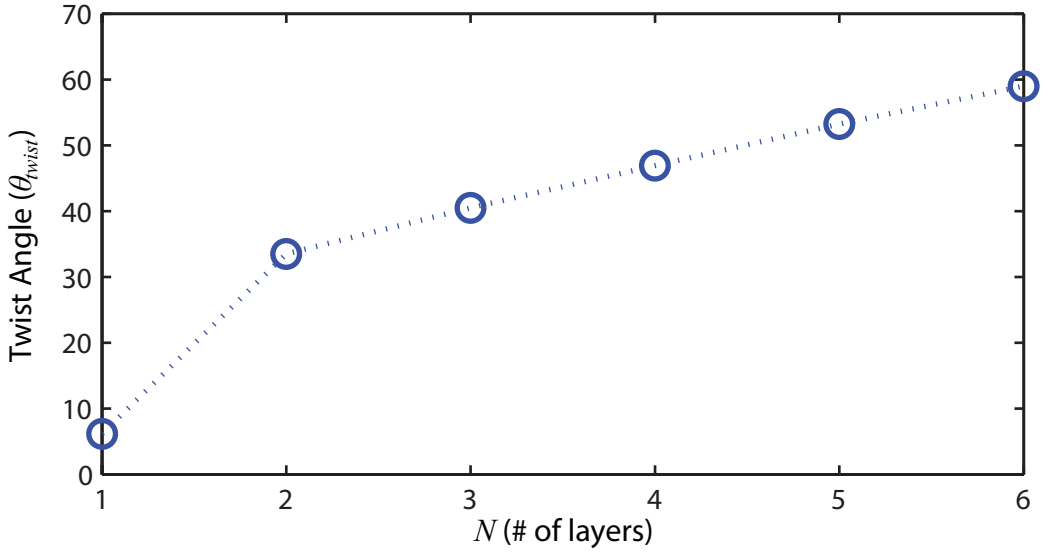


(b) First maximum diffraction efficiency ($\Sigma\eta_{\pm1,max}$) of the twisted PG for different twist angles

Figure 5.20: Diffraction properties of the twisted PG: (a) diffraction efficiency (a sum of $\eta_{\pm1}$) of the twisted PG as a function of the normalized retardation $\Delta n_l d/\lambda$ and (b) the first maximum diffraction efficiency for different twist angles θ_{twist} from 0 to 90°. The grating parameters are $\Lambda = 20\lambda_0$, $n_0 = 1.6$, and $\Delta n_l = 0.2$, where λ_0 is the center wavelength.



(a) The 0^{th} order transmission for multiple layers of the twisted PG



(b) Estimated twist angle for each layer of the twisted PG

Figure 5.21: Diffraction characteristics of the twist PG: (a) spectrums of the 0^{th} order transmission and (b) estimated twist angles of the twisted PG with a number of layers N.

Chapter 6

Conclusion

The derivation of the finite-difference time-domain algorithm starts from the coupling of the electric and magnetic field in the Maxwell curl equations. Material properties of media can be captured in constitution relations described by permittivity ϵ and permeability μ corresponding to the material properties of media. More general expressions for ϵ take the form of tensors with directional dependency as well as magnitude. When a media has different optical properties along a direction (i.e. different values for refractive indices), we call it anisotropic. When describing the propagation of light in anisotropic media, we must take account of the vectorial nature of light, which is already captured in Maxwell's equations.

We developed the modified FDTD method for periodic anisotropic media with nondiagonal permittivity tensor. The periodic boundary conditions at oblique incidence were implemented using the split-field update technique. The new FDTD formulation can be applied to the analysis of periodic structures with arbitrary anisotropy including optical activity at a general angle of incidence. Derivation of this method was outlined in Chapter 3. Wideband source excitation and extraction of frequency information were briefly discussed. Also, the vectorial near- to far-field transformation was introduced.

The new FDTD algorithm was validated by analyzing four different structures: binary phase gratings, dielectric stacks, twisted nematic liquid crystal cells, and a slab structure of optically active media. The results obtained from the FDTD simulations were compared with other analytical or numerical methods. Tests of different physical quanti-

ties like transmittance, diffraction efficiencies, and polarization states of light showed the excellent performance of the FDTD method. To get more accurate results, special care was taken in the simulation time for extracting information. For example, it is very important to determine whether the system is converged to steady state when using monochromatic source excitation. For a wideband source like the Gaussian pulse, the time duration of collecting frequency information is carefully determined to avoid numerical errors.

We applied the FDTD method to the analysis of polarization gratings that have unique diffraction properties owing to their spatially variant anisotropy. Several PG configurations were extensively analyzed. FDTD results were compared with analytical solutions or experimental data, when available, for the diffraction efficiencies. In addition, the effect of grating regimes and finite grating widths was estimated, which cannot be done by analytical methods.

Finally, we proposed three different structures of the broadband PG: the double-layered PG, the achromatic PG using three grating layers, and the double-layered twisted PG. The optical properties of each candidate such as the diffraction efficiency and the bandwidth of the maximum diffraction was evaluated based on the results from FDTD simulations. The achromatic PG using three gratings showed the best performance in terms of the bandwidth. However, the double-layered twisted PG may be more attractive because of its simple structure and comparably large bandwidth. Preliminary experiments have been done to prove the principle of broadband PG structures. More complete experimental study of these broadband PGs remains the topic of further study.

In summary, arbitrary anisotropic properties and periodic boundary conditions were successfully integrated in our new FDTD formulation. FDTD results showed excellent agreement with other analytical or experimental results. This method will be a very efficient and accurate way to analyze diffractive elements with complex structures, which is very difficult or sometimes impossible for analytical solutions. Also, the broadband PG simulations show promise of the FDTD method as an effective tool for novel design of optical elements with advanced properties. We will apply the new FDTD method to analyze novel structures such as photonic bandgap structures, LC displays, and diffractive optical elements.

The FDTD algorithm can be further modified to incorporate more complete material properties including nondiagonal permeability and conductivity tensors. Extension of the FDTD method to three dimensional problems as well as frequency dependent material

properties will be the topic of our future study. More experimental study also needs to be done by implementing the structures designed based on the FDTD simulations.

A package of the FDTD code written in the standard C/C^{++} language will be available to the public as an open source.

Appendix A

Finite-Difference Expressions for P-Q Field Equations

Phase variation across the Yee grid cells at oblique incidence can be removed by introducing the $\boldsymbol{P} = E\exp(jk_x x)$ and $\boldsymbol{Q} = c\mu_0 H\exp(jk_x x)$ fields, where c is the speed of light in a vacuum and $k_x = (\omega/c)\sin\theta_{inc}$. To solve for the modified Maxwell's equations with the $\boldsymbol{P}$ and $\boldsymbol{Q}$ fields, we apply the split-field update technique by defining $\boldsymbol{P} = \boldsymbol{P}_a + \boldsymbol{P}_b$ and $\boldsymbol{Q} = \boldsymbol{Q}_a + \boldsymbol{Q}_b$. The coupling equations of the $\boldsymbol{P}$ and $\boldsymbol{Q}$ fields are given by

$$\frac{j\omega}{c}P_{xa} = -\kappa_{xx}\frac{\partial Q_y}{\partial z} + \kappa_{xy}(\frac{\partial Q_x}{\partial z} - \frac{\partial Q_z}{\partial x}) + \kappa_{xz}\frac{\partial Q_y}{\partial x} \tag{A.1a}$$

$$\frac{j\omega}{c}P_{ya} = -\kappa_{yx}\frac{\partial Q_y}{\partial z} + \kappa_{yy}(\frac{\partial Q_x}{\partial z} - \frac{\partial Q_z}{\partial x}) + \kappa_{yz}\frac{\partial Q_y}{\partial x} \tag{A.1b}$$

$$\frac{j\omega}{c}P_{za} = -\kappa_{zx}\frac{\partial Q_y}{\partial z} + \kappa_{zy}(\frac{\partial Q_x}{\partial z} - \frac{\partial Q_z}{\partial x}) + \kappa_{zz}\frac{\partial Q_y}{\partial x} \tag{A.1c}$$

and

$$P_{xb} = \sin\theta_{inc}(\kappa_{xy}Q_z - \kappa_{xz}Q_y) \tag{A.2a}$$

$$P_{yb} = \sin\theta_{inc}(\kappa_{yy}Q_z - \kappa_{yz}Q_y) \tag{A.2b}$$

$$P_{zb} = \sin\theta_{inc}(\kappa_{zy}Q_z - \kappa_{zz}Q_y) \tag{A.2c}$$

Split equations for "$\boldsymbol{Q}$" field components can be written in a similar way.

$$\frac{j\omega}{c}Q_{xa} = \frac{\partial P_y}{\partial z} \tag{A.3a}$$

$$\frac{j\omega}{c}Q_{ya} = -\frac{\partial P_x}{\partial z} + \frac{\partial P_z}{\partial x} \tag{A.3b}$$

$$\frac{j\omega}{c}Q_{za} = -\frac{\partial P_y}{\partial x} \tag{A.3c}$$

and

$$Q_{xb} = 0 \tag{A.4a}$$

$$Q_{yb} = -\sin\theta_{inc} P_z \tag{A.4b}$$

$$Q_{zb} = \sin\theta_{inc} P_y \tag{A.4c}$$

where subscripts (x, y, z) denotes field components corresponding to the principal axes.

Discrete forms of Eq. A.1 can be expressed as follows:

$$\begin{aligned} P^{n+1}_{xa(i+1/2,k)} &= P^{n}_{xa(i+1/2,k)} \\ &- S\kappa_{xx}\left(Q^{n+1/2}_{y(i+1/2,k+1/2)} - Q^{n+1/2}_{y(i+1/2,k-1/2)}\right) \\ &+ \frac{1}{2}S\kappa_{xy}\left(Q^{n+1/2}_{x(i,k+1/2)} + Q^{n+1/2}_{x(i+1,k+1/2)} - Q^{n+1/2}_{x(i,k-1/2)} - Q^{n+1/2}_{x(i+1,k-1/2)}\right) \\ &- \frac{1}{2}S\kappa_{xy}\left(Q^{n+1/2}_{z(i+3/2,k)} - Q^{n+1/2}_{z(i-1/2,k)}\right) \\ &+ \frac{1}{4}S\kappa_{xz}\left(Q^{n+1/2}_{y(i+3/2,k-1/2)} + Q^{n+1/2}_{y(i+3/2,k+1/2)} - Q^{n+1/2}_{y(i-1/2,k-1/2)} - Q^{n+1/2}_{y(i-1/2,k+1/2)}\right) \end{aligned} \tag{A.5a}$$

$$\begin{aligned} P^{n+1}_{ya(i,k)} &= P^{n}_{ya(i,k)} \\ &+ \frac{1}{2}S\kappa_{yx}\left(Q^{n+1/2}_{y(i-1/2,k+1/2)} + Q^{n+1/2}_{y(i+1/2,k+1/2)} - Q^{n+1/2}_{y(i-1/2,k-1/2)} + Q^{n+1/2}_{y(i+1/2,k-1/2)}\right) \\ &+ S\kappa_{yy}\left(Q^{n+1/2}_{x,(i,j+1/2)} - Q^{n+1/2}_{x,(i,j-1/2)}\right) \\ &- S\kappa_{yy}\left(Q^{n+1/2}_{z,(i+1/2,j)} - Q^{n+1/2}_{z,(i-1/2,j)}\right) \\ &+ \frac{1}{2}S\kappa_{yz}\left(Q^{n+1/2}_{y,(i+1/2,j-1/2)} + Q^{n+1/2}_{y,(i+1/2,j+1/2)} - Q^{n+1/2}_{y,(i-1/2,j-1/2)} - Q^{n+1/2}_{y,(i-1/2,j+1/2)}\right) \end{aligned} \tag{A.5b}$$

$$\begin{aligned} P^{n+1}_{za(i,k+1/2)} &= P^{n}_{za(i,k+1/2)} \\ &- \frac{1}{4}S\kappa_{zx}\left(Q^{n+1/2}_{y(i-1/2,k+3/2)} + Q^{n+1/2}_{y(i+1/2,k+3/2)} - Q^{n+1/2}_{y(i-1/2,k-1/2)} - Q^{n+1/2}_{y(i+1/2,k-1/2)}\right) \\ &+ \frac{1}{2}S\kappa_{zy}\left(Q^{n+1/2}_{x(i,k+3/2)} - Q^{n+1/2}_{x(i,k-1/2)}\right) \\ &- \frac{1}{2}S\kappa_{zy}\left(Q^{n+1/2}_{z(i+1/2,k)} + Q^{n+1/2}_{z(i+1/2,k+1)} - Q^{n+1/2}_{z(i-1/2,k)} - Q^{n-1/2}_{z(i-1/2,k+1)}\right) \\ &+ S\kappa_{zz}\left(Q^{n+1/2}_{y(i+1/2,k+1/2)} - Q^{n+1/2}_{y(i-1/2,k+1/2)}\right) \end{aligned} \tag{A.5c}$$

Similarly, the finite-difference expression for Eq. A.3 are given by

$$Q^{n+1}_{xa(i,k+1/2)} = Q^{n}_{xa(i,k+1/2)} + S\left(P^{n+1/2}_{y(i,k+1)} - P^{n+1/2}_{y(i,k)}\right) \tag{A.6a}$$

$$\begin{aligned} Q^{n+1}_{ya(i+1/2,k+1/2)} &= Q^{n}_{ya(i+1/2,k+1/2)} \\ &\quad - S\left(P^{n+1/2}_{x,(i+1/2,k+1)} - P^{n+1/2}_{x,(i+1/2,k)}\right) + S\left(P^{n+1/2}_{z(i+1,k+1/2)} - P^{n+1/2}_{z,(i,k+1/2)}\right) \end{aligned} \tag{A.6b}$$

$$Q^{n+1}_{za(i+1/2,k)} = Q^{n}_{za(i+1/2,k)} - S\left(P_{y,(i+1,k)} - P_{y,(i,k)}\right) \tag{A.6c}$$

To complete updating the $\boldsymbol{P}$ and $\boldsymbol{Q}$ fields, the "b" components must be removed in a proper way because of their temporal dependency to the total fields. After several mathematical steps, we find that the total fields can be written in terms of the "a" components as follows:

$$Q_z = \frac{1}{D}\left(Q_{za} + \sin\theta_{inc} P_{ya} + \frac{B}{A} P_{za} + C Q_{ya}\right) \tag{A.7a}$$

$$P_z = \frac{1}{A}\left[P_{za} + \sin\theta_{inc}\left(\kappa_{zy} Q_z - \kappa_{zz} Q_{ya}\right)\right] \tag{A.7b}$$

$$Q_x = Q_{xa} \tag{A.7c}$$

$$Q_y = Q_{ya} - \sin\theta_{inc} P_z \tag{A.7d}$$

$$P_x = P_{xa} + \sin\theta_{inc}\left(\kappa_{xy} Q_x - \kappa_{xz} Q_z\right) \tag{A.7e}$$

$$P_y = P_{ya} + \sin\theta_{inc}\left(\kappa_{yy} Q_x - \kappa_{yz} Q_z\right) \tag{A.7f}$$

$$\tag{A.7g}$$

where $A = 1 - \kappa_{zz}\sin^2\theta_{inc}$, $B = \kappa_{yz}\sin^3\theta_{inc}$, $C = (1/A)\kappa_{yz}\sin^2\theta_{inc}$, and $D = 1 - (B/A)\kappa_{zy}\sin\theta_{inc} - \kappa_{yy}\sin^2\theta_{inc}$. The finite-difference forms of Eq. A.7 can be written

as

$$
\begin{aligned}
Q^{n+1}_{z(i+1/2,k)} &= \frac{1}{D} Q^{n+1}_{za(i+1/2,k)} && \text{(A.8a)}\\
&+ \frac{1}{2D}\sin\theta_{inc}\left(P^{n+1}_{ya(i,k)} + P^{n+1}_{ya(i+1,k)}\right)\\
&+ \frac{B}{4AD}\left(P^{n+1}_{za(i,k-1/2)} + P^{n+1}_{za(i,k+1/2)} + P^{n+1}_{za(i+1,k-1/2)} + P^{n+1}_{za(i+1,k+1/2)}\right)\\
&+ \frac{C}{2D}\left(Q^{n+1}_{ya(i+1/2,k-1/2)} + Q^{n+1}_{ya(i+1/2,k+1/2)}\right)\\
P^{n+1}_{z(i,k+1/2)} &= \frac{1}{A} P^{n+1}_{za(i,k+1/2)} && \text{(A.8b)}\\
&+ \frac{1}{4A}\sin\theta_{inc}\kappa_{zy}\left(Q^{n+1}_{z,(i-1/2,k)} + Q^{n+1}_{z,(i+1/2,k)} + Q^{n+1}_{z,(i-1/2,k+1)} + Q^{n+1}_{z,(i+1/2,k+1)}\right)\\
&- \frac{1}{2A}\sin\theta_{inc}\kappa_{zz}\left(Q^{n+1}_{ya,(i-1/2,k+1/2)} + Q^{n+1}_{ya,(i+1/2,k+1/2)}\right)\\
Q^{n+1}_{x,(i,k+1/2)} &= Q^{n+1}_{xa,(i,k+1/2)} && \text{(A.8c)}\\
Q^{n+1}_{y(i+1/2,k+1/2)} &= Q^{n+1}_{ya(i+1/2,k+1/2)} && \text{(A.8d)}\\
&- \frac{1}{2}\sin\theta_{inc}\left(P^{n+1}_{z,(i,k+1/2)} + P^{n+1}_{z,(i+1,k+1/2)}\right)\\
P^{n+1}_{x(i+1/2,k)} &= P^{n+1}_{xa(i+1/2,k)} && \text{(A.8e)}\\
&+ \frac{1}{4}\sin\theta_{inc}\kappa_{xy}\left(Q^{n+1}_{x,(i,k-1/2)} + Q^{n+1}_{z,(i+1,k-1/2)} + Q^{n+1}_{x,(i,k+1/2)} + Q^{n+1}_{z,(i+1,k+1/2)}\right)\\
&- \sin\theta_{inc}\kappa_{xz} Q^{n+1}_{z,(i+1/2,k)}\\
P^{n+1}_{y(i,k)} &= P^{n+1}_{ya(i,k)} && \text{(A.8f)}\\
&+ \frac{1}{2}\sin\theta_{inc}\kappa_{yy}\left(Q^{n+1}_{x,(i,k-1/2)} + Q^{n+1}_{x,(i,k+1/2)}\right)\\
&- \frac{1}{2}\sin\theta_{inc}\kappa_{yz}\left(Q^{n+1}_{z,(i-1/2,k)} + Q^{n+1}_{z,(i+1/2,k)}\right)
\end{aligned}
$$

Note that field values at every integer and half-integer time-step need to be stored in different variables.

Bibliography

[1] J. C. Maxwell, "A dynamical theory of the electromagnetic field," *Philos. Trans. R. Soc. Lond., A*, vol. 155, pp. 459–512, 1865.

[2] S. D. Kakichashvili, "Method of recording phase polarization holohrams," *Sov. J. Quant. Electron.*, vol. 4, pp. 795–798, 1974.

[3] L. Nikolova and T. Todorov, "Diffraction efficiency and selectivity of polarization holographic recording," *Opt. Acta*, vol. 31, pp. 579–588, 1984.

[4] L. Nikolova, T. Todorov, M. Ivanov, F. Andruzzi, S. Hvilsted, and P. S. Ramanujam, "Polarization holographic gratings in side-chain azobenzene polyesters with linear an circular photoanisotropy," *Appl. Opt.*, vol. 35, pp. 3835–3840, 1996.

[5] F. Gori, "Measuring stokes parameters by means of a polarization grating," *Opt. Lett.*, vol. 24, pp. 584–586, 1999.

[6] V. Sankaran, M. J. Everett, D. J. Maitland, and J. J. T. Walsh, "Comparison of polarized-light propagation in biological tissue and phantoms," *Opt. Express.*, vol. 13, pp. 601–611, 2005.

[7] J. A. Davis, J. Adachi, C. R. Fernandez-Pousa, and I. Moreno, "Polarization beam splitters using polarization diffraction gratings," *Opt. Lett.*, vol. 26, pp. 587–589, 2001.

[8] Z. Bomzon, G. Biener, V. Kleiner, and E. Hasman, "Real-time analysis of partially polarized light with a space-variant subwavelength dielectric grating," *Opt. Lett.*, vol. 27, pp. 188–190, 2002.

[9] G. Cincotti, "Polarization gratings: Design and applications," *IEEE J. Quantum Electron.*, vol. 39, pp. 1645–1652, 2003.

[10] T. Yamamoto, M. Koashi, S. K. Ozdemiir, and N. Imoto, "Experimental extraction of an entangled photon pair from two identically decohered pairs," *Nature*, vol. 421, pp. 343–346, 2003.

[11] H. Kogelink, "Coupled wave theory for thick hologram gratings," *Bell Syst. tech. J.*, vol. 48, pp. 2909–2947, 1969.

[12] R. S. Chu and J. A. Kong, "Modal theory of spatially periodic media," *IEEE Trans. Microwave Theory Tech.*, vol. MTT-25, pp. 18–24, 1977.

[13] R. C. Jones, "A new calculus for the treatment of optical systems. i. description and discussion of the calculus," *J. Opt. Soc. Am.*, vol. 31, pp. 488–, 1941.

[14] J. Tervo and J. Turunen, "Paraxial-domain diffractive elements with 100% efficieincy based on polarization gratings," *Opt. Lett.*, vol. 25, pp. 785–786, 2000.

[15] M. Ivanov and T. Eiju, "Analysis of the properties of polarization holographic diffraction gratings," *Proc. SPIE*, vol. 4659, pp. 361–368, 2002.

[16] G. Cipparrone, A. Mazzulla, and L. Blinov, "Permanent polarization gratings in photosensitive langmuir-blodgett films for polarimetric applications," *J. Opt. Soc. Am. B*, vol. 19, pp. 1157–1161, 2002.

[17] K. S. Yee, "Numerical solution of initial boundary value problems involving maxwell's equations in isotropic media," *IEEE Trans. Antenn. Propag.*, vol. 14, pp. 302–307, 1966.

[18] A. Taflove and S. C. Hagness, *Computational Electrodynamics: Finite-Difference Time-Domain Method*. Norwood, MA: Artech House, 2nd ed., 2000.

[19] J. Schneider and S. Hudson, "The finite-difference time-domian method applied to anisotropic material," *IEEE Trans. Antenn. Propag.*, vol. 41, pp. 994–999, 1993.

[20] J. A. Roden, S. D. Gedney, M. P. Kesler, J. G. Maloney, and P. H. Harms, "Time-domain analysis of periodic structures at oblique incidence: Orthorgonal and

nonorthogonal fdtd implementation," *IEEE Trans. Microwave Theory Tech.*, vol. 46, pp. 420–427, 1998.

[21] E. Collett, *Polarized Light: fundamentals and applications*. New York: Marcel Dekker, 1993.

[22] M. Born and E. Wolf, *Principles of Optics*. New York: Cambridge University Press, 7th ed., 1999.

[23] G. R. Fowles, *Introduction to Mordern Optics*. New York: Holt, Rinehart and Winston, 1968.

[24] P. Yeh, *Optics*. New York: Addison-Wesley Publshing Co., 1993.

[25] W. R. Klien and B. D. Cook, "Unified approach to ultrasonic light diffraction," *IEEE Trans. Ultrason. Ferr.*, vol. SU14, p. 123, 1967.

[26] M. G. Moharam and L. Yong, "Criterion for bragg and raman-nath diffraction regimes," *Appl. Opt.*, vol. 17, pp. 1757–1759, 1978.

[27] I. Richter, Z. Ryzi, and P. Fiala, "Analysis of binary diffraction gratings: comparison of different approaches," *J. Mod. Opt.*, vol. 16, pp. 1915–1917, 1991.

[28] M. G. Moharam and T. K. Gaylord, "Rigorous coupled-wave analysis of planar-grating diffraction," *J. Opt. Soc. Am.*, vol. 71, pp. 811–818, 1981.

[29] T. K. Gaylord and M. G. Moharam, "Analysis and applications of optical diffraction by gratings," *Proc. IEEE*, vol. 73, pp. 894–937, 1985.

[30] M. G. Moharam and T. K. Gaylord, "Rigorous coupled-wave analysis of metallic surface-relief gratings," *J. Opt. Soc. Am. A*, vol. 3, pp. 1780–1796, 1986.

[31] P. Lalanne and D. Lemercier-Lalanne, "On the effective medium theory of subwavelength periodic structures," *J. Mod. Opt.*, vol. 43, pp. 2063–2085, 1996.

[32] E. B. Grann, M. G. Moharam, and D. A. Pommet, "Artificial uniaxial and biaxial dielectrics with use of two-dimensional subwavelength binary gratings," *J. Opt. Soc. Am. A*, vol. 11, pp. 2695–2703, 1994.

[33] H. Kikuta, H. Yoshida, and K. Iwata, "Ability and limitation of effective medium theory for subwavelength gratings," *Opt. Rev.*, vol. 2, pp. 92–99, 1995.

[34] I. Richter, P.-C. Sun, F. Xu, and Y. Fainman, "Design considerations of form birefringent microstructures," *Appl. Opt.*, vol. 34, pp. 2421–2429, 1995.

[35] I. Richter, P.-C. Sun, F. Xu, and Y. Fainman, "Artificial uniaxial and biaxial dielectrics with the use of photoinduced gratings," *J. Appl. Phys.*, vol. 81, pp. 23–29, 1996.

[36] M. L. Doucen and P. Pellat-Finet, "Polarization properties and diffraction efficiencies of binary anisotropic gratings: general study and experiments on ferroelectric liquid crystals," *Opt. Commun.*, vol. 151, pp. 321–330, 1998.

[37] J. Park, C. Yu, J. Kim, S. Chung, and S. Lee, "Concept of a liquid-crystal polarization beamsplitter based on binary phase gratings," *apl*, vol. 83, pp. 1918–1920, 2003.

[38] E. Hecht, *Optics*. San Francisco: Addison-Wesley Pub. Co., 4th ed., 2002.

[39] G. Mur, "Absorbing boundary conditions for the finite-difference approximation of the time-domain electromagnetic field equations," *IEEE Trans. electromagn. C.*, vol. 23, pp. 377–382, 1981.

[40] J. P. Berenger, "A perfectly matched layer for the absorption of electromagnetic waves," *J. Computat. Phys.*, vol. 23, pp. 185–200, 1994.

[41] J. P. Berenger, "Three-dimensional perfectly matched layer for the absorption of electromagnetic waves," *J. Computat. Phys.*, vol. 23, pp. 363–379, 1996.

[42] W. C. Chew and W. H. Weedon, "A 3d perfectly matched medium from modified maxwell's equations with streched coordinates," *Microwave and Optical technology Lett.*, vol. 7, pp. 599–604, 1994.

[43] Z. S. Sacks, D. M. Kingsland, R. Lee, and J.-F. Lee, "A perfectly matched anisotropic absorber for use as an absorbing boundary condition," *IEEE Trans. Antenn. Propag.*, vol. 43, pp. 1460–1463, 1995.

[44] R. Mittra and U. Pekel, "A new look at the perfectly matched layer (pml) concept for the reflectionless absorption of electromagnetic waves," *IEEE Micro. Guided W.*, vol. 5, pp. 84–86, 1995.

[45] S. D. Gedney, "An anisotropic perfectly matched layer-absorbing medium for the truncation of fdtd lattices," *IEEE Trans. Antenn. Propag.*, vol. 44, pp. 1630–1639, 1996.

[46] J. A. Roden and S. D. Gedney, "Convolution pml (cpml): An efficient fdtd implementation of the cfs-pml for arbitrary media," *Microw. Opt. Techn. Let.*, vol. 27, pp. 334–339, 2000.

[47] D. M. Sullivan, "A simplified pml for use with the fdtd method," *IEEE Microwave and Guided Wave Letters*, vol. 6, pp. 97–99, 1996.

[48] M. G. Moharam, E. B. Grann, D. A. Pommet, and T. K. Gaylord, "Formulation for stable and efficient implementation of the rigorous coupled-wave analysis of binary gratings," *Proc. IEEE*, vol. 73, pp. 894–937, 1985.

[49] N. Chateau and J.-P. Hugonin, "Algorithm for the rigorous coupled-wave analysis of grating diffraction," *J. Opt. Soc. Am. A*, vol. 11, pp. 1321–1331, 1994.

[50] I. Celanovic, F. O'Sullivan, M. Ilak, J. Kassakian, and D. Perreault, "Design and optimization of one-dimensional photonic crystals for thermophotovoltaic applications," *Opt. Lett.*, vol. 29, pp. 863–865, 2004.

[51] F. O'Sullivan, I. Celanovic, N. Jovanovic, J. Kassakian, S. Akiyama, and K. Wada, "Optical characteristics of one-dimensional si/sio2 photonic crystals for thermophotovoltaic applications," *J. Appl. Phys.*, vol. 97, no. 033529, 2005.

[52] S. Chandrasekhar, *Liquid Crystals*. Cambridge: Cambridge U. Press, 1992.

[53] C. H. Gooch and H. A. Tarry, "The optical properties of twisted nematic liquid crystal structures with twist angles ≤ 90 degrees," *J. Phys. D: Appl. Phys.*, vol. 8, pp. 1575–1584, 1975.

[54] W. H. Southwell, "Gradient-index antireflection coatings," *Opt. Lett.*, vol. 8, pp. 584–586, 1983.

[55] M. Attia and J. Jonathan, "Anisotropic gratings recorded from two circularly polarized coherent waves," *Opt. Commun.*, vol. 47, pp. 85–90, 1983.

[56] B. Wen, R. G. Petschek, and C. Rosenblatt, "Nematic liquid-crystal polarization gratings by modification of surface alignment," *Appl. Opt.*, vol. 41, pp. 1246–1250, 2002.

[57] J. N. Eakin, Y. Xie, R. A. Pelcovits, M. D. Radcliffe, and G. P. Crawford, "Patterned alignment layers using holographic exposure technique," *SID Digest*, vol. 04, pp. 578–581, 2004.

[58] M. J. Escuti and W. M. Jones, "Polarization independent switching with high contrast from a liquid crystal polarization grating," *SID Digest*, vol. 37, pp. 39.34–, 2006.

[59] Z. Bomzon, G. Biener, V. Kleiner, and E. Hasman, "Spatial fourier-transform polarimetry using space-variant subwavelength metal-strip polarizers," *Opt. Lett.*, vol. 26, pp. 1711–1713, 2001.

[60] Z. Bomzon, G. Biener, V. Kleiner, and E. Hasman, "Radially and azimutally polarized beam generated by space-variant dielectric subwavelength gratings," *Opt. Commun.*, vol. 209, pp. 45–54, 2002.

[61] J. Tervo, V. Kettunen, M. Honkanen, and J. Turunen, "Design of space-variant diffractive polarization elements," *J. Opt. Soc. Am. A*, vol. 20, pp. 282–289, 2003.

[62] S. L. Jacques, J. C. Ramella-Roman, and K. Lee, "Imaging skin pathology with polarized light," *J. Biomed. Opt.*, vol. 7, pp. 329–340, 2002.

[63] E. Hasman, Z. Bomzon, A. Niv, G. Biener, and V. Kleiner, "Polarization beam-splitters and optical switches based on space-variant computer-generated subwavelength quasi-periodic structures," *Opt. Commun.*, vol. 209, pp. 45–54, 2002.

[64] G. Cincotti, "Design and fabrication techniques for polarization gratings for polarization mode dispersion measurements," *J. Opt. A: Pure Appl. Opt*, vol. 6, pp. S100–S104, 2004.

[65] J. N. Eakin, Y. Xie, R. A. Pelcovits, M. D. Radcliffe, and G. P. Crawford, "Zero voltage freedericksz transition in periodically alligned liquid crystals," *Appl. Phys. Lett.*, vol. 85, pp. 1671–1673, 2004.

[66] P. Hariharan and P. E. Ciddor, "Broad-band superachromatic retarders and circular polarizers for the uv, visible and near infrared," *J. mod. Optics*, vol. 51, pp. 2315–2322, 2004.

[67] Y. Huang, Y. Zhou, C. Doyle, and S. Wu, "Tuning the photonic band gap in cholesteric liquid crystals by temperature-dependent dopant solubility," *Opt. Express.*, vol. 14, pp. 1236–1242, 2006.